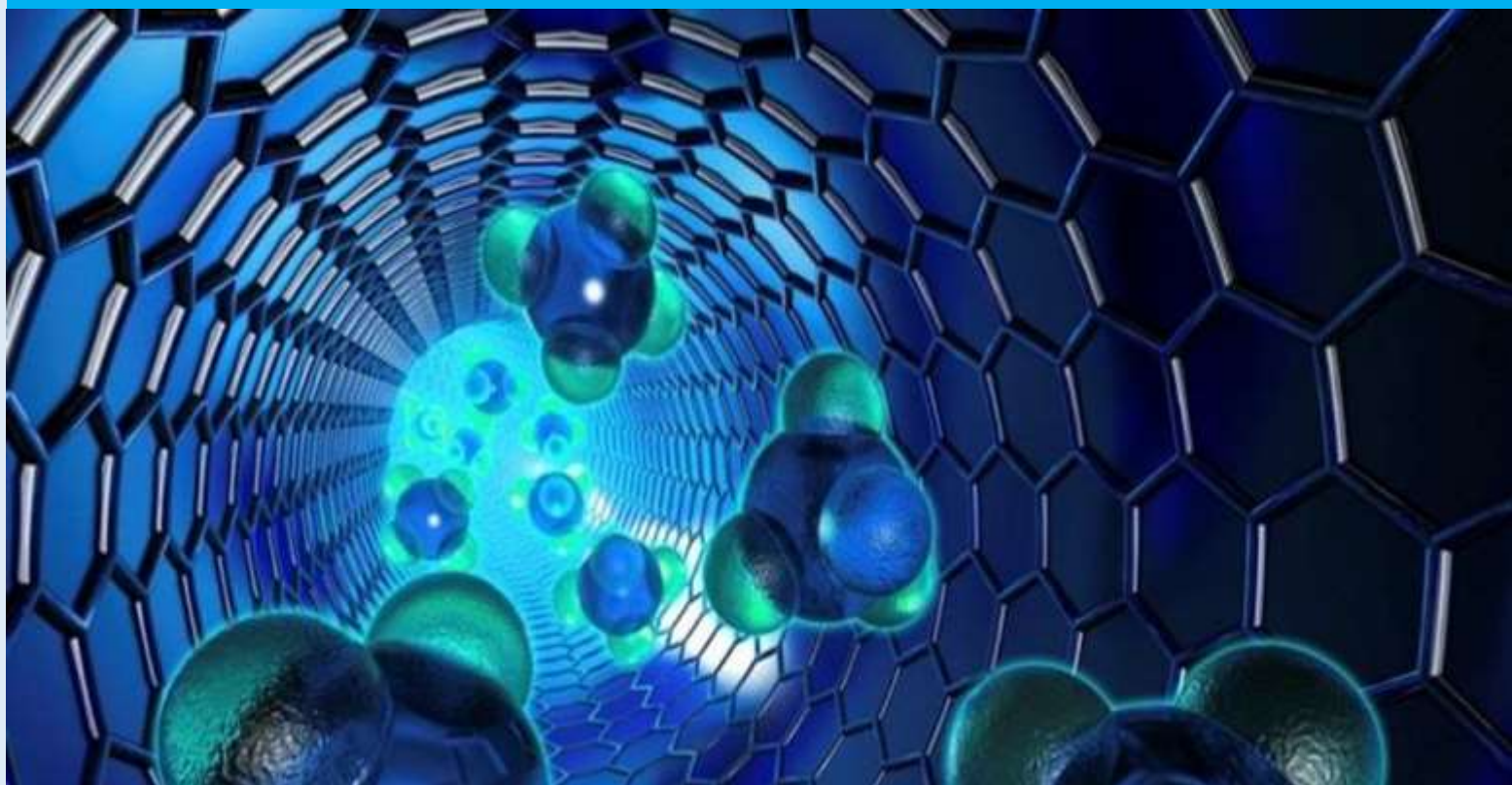


e-ISSN: 2602-277X

International Journal of Chemistry and Technology



**Volume: 5, Issue: 1
E - Journal**

**30 JUNE 2021
<http://dergipark.org.tr/ijct>**

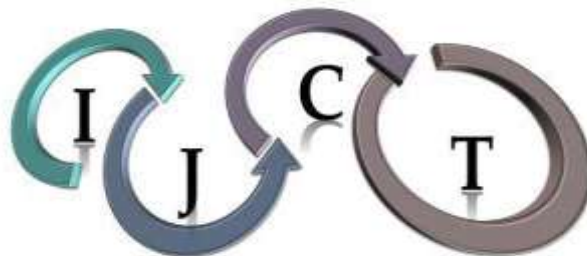


International Journal of Chemistry and Technology

JOURNAL INFO

Journal Name	International Journal of Chemistry and Technology
Journal Initial	IJCT
Journal Abbreviation	Int. J. Chem. Technol.
ISSN (Online)	2602-277X
Year of Launching	2017, August
Editor-in-Chief and Managing Editor	Prof. Dr. İbrahim Demirtaş
Manager of Publication	Assist. Prof. Mehmet Akyüz
Scope and Focus	Chemistry, Material Science, Technology
Review Type	Peer Review Double-Blinded
Ethical Rules	Plagiarism check, copyright agreement form, conflict of interest, ethics committee report
Access Type	Open Access
Publication Fee	Free
Article Language	English
Frequency of Publication	Biannually
Publication Issue	June, December
Publisher	Prof. Dr. İbrahim Demirtaş
Web Page	http://dergipark.org.tr/ijct
Contact E-mail address	ijctsubmission@gmail.com, ijctsubmission@yahoo.com
Contact Address and Executive address	Department of Chemistry, Faculty of Arts and Sciences, Iğdir University, 76000, Iğdir, Turkey
Contact Telephone	90 532 233 17 38 (Secretary)
Publication Date	30/06/2021
Technical Editor	Assist. Prof. Dr. Evrim BARAN AYDIN
Spelling Editor	Dr. Oğuzhan Koçer, MSc. Rabia Acemioğlu
Language (Grammar) Editor	Assist. Prof. Dr. Muhammet KARAMAN, Assist. Prof. Dr. Muhittin KULAK, Dr. Lawali YABO DAMBAGI
Secretary	Dr. Oğuzhan KOÇER, MSc. Rabia ACEMIOĞLU

All detailed information including instructions for authors, aim and scopes, ethical rules, manuscript evaluation, indexing info, and manuscript template etc. can be found on the main web page of IJCT (<http://dergipark.gov.tr/ijct>).



International Journal of Chemistry and Technology

Volume: 5, Issue: 1, Year 2021

Founder of IJCT

Prof. Dr. Bilal ACEMIOĞLU

EDITORIAL BOARD

Editor-in-Chief

Prof. Dr. İbrahim DEMİRTAŞ

(Organic Chemistry and Phytochemistry, Iğdır University, Iğdır, Turkey)

Associate Editors

Prof. Dr. M. Hakkı ALMA
(Material Science and Technology
K.Maraş Sütçü İmam/Iğdır University, Turkey)

Prof. Dr. Ekrem KÖKSAL
(Biochemistry,
Erzincan Binali Yıldırım University, Erzincan,
Turkey)

Prof. Dr. Fevzi KILIÇEL
(Analytical Chemistry,
Karamanoğlu Mehmet Bey Uni., Karaman, Turkey)

Prof. Dr. Mehmet SÖNMEZ
(Inorganic Chemistry, Gaziantep
University, Gaziantep, Turkey)

Prof. Dr. Yuh-Shan HO
(Chemical and Environmental Engineering,
Asia University, Taichung City, Taiwan)

Prof. Dr. Yahya GÜZEL
(Theoretical Chemistry and Polymer Chemistry
Erciyes University, Kayseri, Turkey)

Prof. Dr. Mustafa ARIK
(Physical Chemistry,
Atatürk University, Erzurum, Turkey)



International Journal of Chemistry and Technology

Advisory Editorial Board

Prof. Dr. Harun PARLAR
(Technical University of Munich, München Germany)

Prof. Dr. Shaobin WANG
(Curtin University, Perth, Australia)

Prof. Dr. Ana Beatriz Rodriguez MORATINOS
(University of Exramadura, Badajoz, Spain)

Prof. Dr. Jon-Bae KIM
(College of Health Sciences, South Korea)

Prof. Dr. Rashid AHMAD
(University of Malakand, Chakdara, Pakistan)

Prof. Dr. Guang-Jie ZHAO
(Beijing Forestry University, Beijing, China)

Prof. Dr. Jaine H. Hortolan LUIZ
(Federal University of Alfenas, Unifal-MG, Brazil)

Prof. Dr. Papita DAS
(Jadavpur University, Jadavpur, India)

Prof. Dr. Vagif ABBASOV
(Nef-Kimya Prosesleri Institutu, Baku, Azerbaijan)

Prof. Dr. Atiqur RAHMAN
(Islamic University, Kushita, Bangladesh)

Prof. Dr. Mika SILLANPAA
(LUT Lappeenranta Uni.y of Technology, Lappeenranta, Finland)

Prof. Dr. Salah AKKAL
(University of Mentouri Consatntine Consatntine, Algeria)

Prof. Dr. Gilbert Kapche DECCAUX
(University of Yaounde I, Yaounde, Cameroon)

Prof. Dr. Gelu BOURCEANU
(Alexandru Ioan Cuza University, Romania)

Prof. Dr. Ahmet ÇAKIR
(Kilis 7 Aralik University, Kilis, Turkey)

Prof. Dr. M. SALIH AĞIRTAŞ
(Yüzüncü Yıl University, Van, Turkey)

Prof. Dr. Nufullah SARAÇOĞLU
(Atatürk University, Erzurum, Turkey)

Prof. Dr. Rahmi KASIMOĞULLARI
(Dumlupınar University, Kütahya, Turkey)

Prof. Dr. Ahmet Baysar
(Inonu University, Malatya, Turkey)

Prof. Dr. Hamdi TEMEL
(Dicle University, Diyarbakır, Turkey)

Prof. Dr. Ö. İrfan KÜFREVOĞLU
(Atatürk University, Erzurum, Turkey)

Prof. Dr. Ömer ŞAHİN
(Siirt University, Siirt, Turkey)

Prof. Dr. Anatoli DIMOGLU
(Düzce University, Düzce, Turkey)

Prof. Dr. Mehmet UĞURLU
(Sıtkı Kocman University, Muğla, Turkey)

Prof. Dr. Şükrü BEYDEMİR
(Anadolu University, Eskişehir, Turkey)

Prof. Dr. Ramazan SOLMAZ
(Bingol University, Bingöl, Turkey)

Prof. Dr. Mahfuz ELMASTAŞ
(Health Sciences University, İstanbul, Turkey)

Prof. Dr. Mehmet DOĞAN
(Balıkesir University, Balıkesir, Turkey)

Prof. Dr. Giray TOPAL
(Dicle University, Diyarbakır, Turkey)

Prof. Dr. Birgül YAZICI
(Cukurova University, Adana, Turkey)



International Journal of Chemistry and Technology

Advisory Editorial Board

Prof. Dr. Barbaros NALBANTOĞLU
(Yıldız Technical University, İstanbul, Turkey)

Prof. Dr. Murat ALANYALIOĞLU
(Atatürk University, Erzurum, Turkey)

Prof. Dr. T. Abdulkadir ÇOBAN
(Erzincan Binali Yıldırım University, Erzincan Turkey)

Prof. Dr. İsmet KAYA
(18 Mart University, Çanakklae, Turkey)

Prof. Dr. Serhan URUŞ
(Sütçü İmam University, K.Maraş, Turkey)

Prof. Dr. Ömer İŞILDAK
(Gaziosmanpaşa University, Tokat, Turkey)

Prof. Dr. Halim AVCI
(Kilis 7 Aralık University, Kilis, Turkey)

Prof. Dr. Ahmet TUTAR
(Sakarya University, Sakarya, Turkey)

Prof. Dr. Duygu EKINCI
(Atatürk University, Erzurum, Turkey)

Prof. Dr. Metin BÜLBÜL
(Dumlupınar University, Kütahya, Turkey)

Prof. Dr. Ali KARA
(Uludağ University, Bursa, Turkey)

Prof. Dr. Murat SARAÇOĞLU
(Erciyes University, Kayseri, Turkey)

Prof. Dr. Murat SADIKOĞLU
(Gaziosman Paşa University, Tokat, Turkey)

Prof. Dr. Mustafa KARATAŞ
(Aksaray University, Aksaray, Turkey)

Assoc. Prof. Dr. Şenay ŞİMŞEK
(North Dakota State University, Fargo, USA)

Assoc. Prof. Dr. Mahjoub JABLI
(University of Monastir, Monastir, Tunisia)

Assoc. Prof. Dr. Muhammet KÖSE
(Sütçü İmam University, K.Maraş, Turkey)

Assoc. Prof. Chin-Hung LAI
(Chung Shan Medical University, Taiwan)

Assoc. Prof. Niyaz M. MAHMOODI
(Institute for Color Science and Technology Tehran, Iran)

Assoc. Prof. Dr. Mustafa ÖZDEMİR
(Süleyman Demirel University, Isparta, Turkey)

Assoc. Prof. Dr. Metin AÇIKYILDIZ
(Kilis 7 Aralık University, Kilis, Turkey)

Assist. Prof. Masood Ayoub KALOO
(Govt. Degree College Shopian, J & K, India)

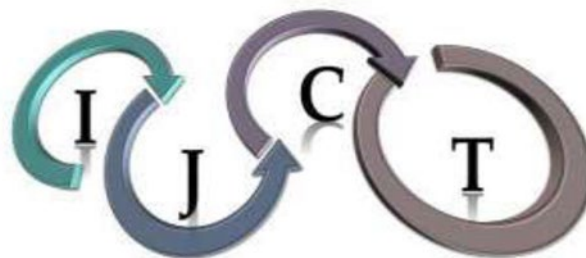
Assist. Prof. Dr. Mutasem Z. BANI-FWAZ
(King Khalid University, Asir-Abha, Saudi Arabia)

Assist. Prof. Dr. Bakhtiyor RASULEV
(North Dakota State University, Fargo, USA)

Dr. Zineb TRİBAK
(Sidi Mohamed Ben Abdellah University, Fez Morocco)

Dr. Sameer Ahmed AWAD
(University of Anbar, Ramadi, Iraq)

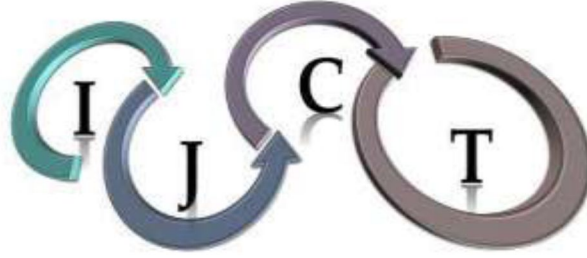
Dr. Ramadan E. ASHERY
(Damanhour University, Egypt)



International Journal of Chemistry and Technology

TABLE OF CONTENTS

Research Articles	Pages
1. Effect of nano-multimetallic catalyst on hydrogen production by hydrolysis of ammonia borohydride Nano boyutlu multi metalik katalizörünün Amonyak boran hidroliziyle hidrojen üretimine etkisi Erhan ONAT, Mehmet Sait İZGİ	1-5
2. Antifungal effect of some essential oil Bazı uçucu yağ kombinasyonlarının antifungal etkisi Musa TÜRKMEN, Durmuş Alpaslan KAYA	6-10
3. Investigation Confirmation by molecular docking of the pharmacophore defined as 4D-QSAR using the MCET method for the 2-hydroxydiarylamide derivatives 2-hidroksidiarilamid türevleri için 4D-QSAR'da MCET yöntemi kullanılarak belirlenen farmakoforum moleküler docking ile doğrulanması Burçin TÜRKMENÖĞLU, Yahya GÜZEL	11-25
4. The activity of ceria supported complex in hydrogen generation Seryum oksit destekli kompleksin hidrojen üretimindeki aktivitesi Dilek KILINÇ, Ömer ŞAHİN	26-32
5. Silica-coated magnetic Fe ₃ O ₄ nanoparticles as efficient nano-adsorbents for the improvement of the vapor-phase adsorption of benzene Benzenin buhar-fazı adsorpsiyonunun iyileştirilmesi için etkili nano-adsorbentler olarak silika-kaplı manyetik Fe ₃ O ₄ nanoparçacıkları Mehmet Şakir ECE, Sinan KUTLUAY, Ömer ŞAHİN	33-41
6. Structural and theoretical study based on DFT calculations of 3-Methyl-4- [3-ethoxy-(2-p-metilbenzenesulfonyloxy)-benzylidenamino]-4,5-dihydro-1H-1,2,4-triazol-5-one Manyetik 3-Metil-4-[3-etoksi-(2-p-metilbenzensülfoniloksi)-benzilidenamino]-4,5-dihidro-1H-1,2,4-triazol-5-on'un DFT hesaplamalarına dayalı yapısal ve teorik çalışması Gül KOTAN, Faruk KARDAŞ	42-51
7. The anticancer activity of chalcone compounds against human prostate carcinoma cell and human colon colorectal adenocarcinoma Kalkon bileşiklerinin insan prostat karsinom hücresi ve kolon kolorektal adenokarsinomuna karşı antikanser aktivitesi Bedriye Seda KURŞUN AKTAR, Ayşe ŞAHİN YAĞLIOĞLU, Emine Elçin ORUÇ-EMRE	52-58



8. Determination of electronic characteristics of tetrahydro pyrimidine derivatives and investigation of usability as anti-corrosion 59-66
Tetrahidro pirimidin türevlerinin elektronik özelliklerinin belirlenmesi ve korozyon önleyici olarak kullanılabilirliğinin araştırılması
Murat OKAY, Erdem ERGAN, Begüm Çağla AKBAŞ, Esvet AKBAŞ
9. Comparison of the chemical composition and bioactive properties of extracts prepared from the mature Turkish and Brazilian banana peels 67-76
Olgun Türk ve Brezilya muz kabuklarından hazırlanan ekstraktların kimyasal bileşimi ve biyoaktivite özelliklerinin karşılaştırılması
Tevfik ÖZEN, İbrahim DEMİRTAŞ
10. Inhibition profiles and molecular docking studies of antiproliferative agents against aldose reductase enzyme 77-82
Antiproliferatif ajanların aldoz redüktaz enzimine karşı inhibisyon profilleri ve moleküler docking çalışmaları
Namık KILINÇ



Effect of nano-multimetallic catalyst on hydrogen production by hydrolysis of ammonia borohydride

Erhan Onat¹, Mehmet Sait İZGİ^{1,*}

¹Siirt University Faculty of Engineering and Architecture, Department of Chemical Engineering, Siirt, Turkey

Received: 26 August 2020; Final revised: 09 October 2020; Accepted: 10 October 2020

*Corresponding author e-mail: saitizgi@gmail.com

Citation: Onat, E.; İzgi, M.S. *Int. J. Chem. Technol.* 2021, 5 (1), 1-5.

ABSTRACT

This study focuses on the hydrolysis of hydrogen production parameters through the synthesized catalyst Co-Cr-B from ammonia borane using the low cost of cobalt (Co) and chromium (Cr). The synthesized Co-Cr-B catalyst was interacted with the ammonia borane solution. Later, optimum conditions for the hydrolysis of ammonia borane were determined at different catalyst amounts, NaOH concentrations, catalytic activities, and temperatures. Reaction kinetics was examined using the data obtained, and the activation energy of the reaction was determined as 22.30 kJ.mol⁻¹. The degree of reaction was in agreement with the 1st degree.

Keywords: Ammonia borane, Co-Cr-B, hydrogen, nanocatalyst, hydrolysis.

Nano boyutlu multi metalik katalizörünün Amonyok boran hidroliziyle hidrojen üretimine etkisi

ÖZ

Bu çalışma, düşük maliyetli kobalt (Co) ve krom (Cr) kullanılarak amonyak borandan sentezlenmiş katalizör Co-Cr-B aracılığıyla hidrojen üretim parametrelerinin hidrolizine odaklanmaktadır. Sentezlenen Co-Cr-B katalizörü, amonyok boran çözeltisi ile etkileştirildi. Daha sonra amonyok boranın hidrolizi için optimum koşullar, farklı katalizör miktarlarında, NaOH konsantrasyonlarında, katalitik aktivitelerde ve sıcaklıklarda belirlendi. Reaksiyon kinetiği elde edilen veriler kullanılarak incelendi ve reaksiyonun aktivasyon enerjisi 22.30 kJ mol⁻¹ olarak belirlendi. Reaksiyonun derecesi 1. derece ile uyumluydu.

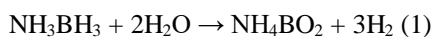
Anahtar Kelimeler: Amonyum boran, Co-Cr-B, hidrojen, nanokatalizör, hidroliz.

1. INTRODUCTION

Rather than the decrease of fossil fuels over time, they spread to the environment because of using these fuels; toxic wastes such as unburned hydrocarbon, soot, odor, carbon monoxide (CO) and carbon dioxide (CO₂) with greenhouse effect disrupt the ecological balance and harm human health. Alternative clean energy sources that will overcome the environmental and environmental energy problems in the future are among the most researched topics by researchers. Hydrogen (H₂) comes to the fore as one of the most important of these energy sources researched today.¹ Systems that enable the use of hydrogen as an energy source are defined as Proton Exchange Membrane (PEM) fuel cells. In these cells, electricity is produced by taking hydrogen into the system. The basic requirement of

using hydrogen as an energy source is that hydrogen is obtained from many sources. These resources can be listed as follows; electrolysis,³ hydrolysis,⁴ etc. from water by thermochemical methods from fossil sources.⁵ Methods, photoelectrochemical methods from solar energy,⁶ photobiological methods from green algae and plant tissue⁷ and chemical methods from boron-derived compounds.⁸ While considering the conditions of using hydrogen as an energy source, there is a fundamental problem of gas storage and transportation of hydrogen due to the high cost of hydrogen fuel technology. With the chemical storage of hydrogen in boron compounds, transportation and storage problems are largely eliminated.^{8, 9-11} Ammonia borane is one of the boron-sourced compounds used in hydrogen storage. Besides

being capable of storing high hydrogen (16.6% by mass), ammonia borane allows hydrolysis to be separated from water by hydrolysis as well as the hydrogen it contains in its structure and enables high yield of hydrogen. The hydrogen decomposition reaction is given in Eq. (1).



The reaction rate given in Eq. (1) can be adjusted with the catalyst. This provides great advantages in the use of hydrogen as an energy carrier, eliminating the problem of transport and storage.

1.1. Catalyst in hydrogen production

Catalysts are generally defined as substances that increase the reaction rate. It is possible to summarize hydrogen production from boron-borne compounds as in Equality 1 in general. Hydrolysis reactions are generally catalyst controlled. Considering that the hydrogen requirement is obtained from the reaction and the reaction is catalyst controlled, it is understood that the catalyst is important for hydrogen production. Metals used as catalysts are usually precious metals such as Rh, Ru, Pd and P.¹²⁻¹⁶ Although they have high hydrocatalytic activities, the cost of these metals is quite high. Recently, catalyst production is obtained from non-precious metals (such as Co, Cu, Ni, Mn) and metal alloys, whose efficiency can be increased with multimetallic systems.¹⁷⁻¹⁹ In this work, we report the synthesis, characterization and application of H₂ release of multimetallic-based CoCrB catalyst. Co and Cr were selected because they are highly reactive metals in the hydrolysis of boron based metal hydrides and B was coupled with NaBH₄ reduction method during synthesis which showed superior catalytic performance with a high rate of maximum hydrogen production rate 6071 ml g⁻¹min⁻¹

2. MATERIALS AND METHODS

Within the scope of the study, the catalyst was synthesized according to the literature.^{14,15} The chemical was weighed at the ratios determined for the synthesis process¹⁰ and mixed in the magnetic stirrer for 30 minutes at 500 rpm and then reduced with sodium borohydride at the specified rates. The catalyst obtained after reduction was filtered by vacuum filtration and left to dry in an oven at 60°C for 6 h under nitrogen gas. Hydrolysis reactions of ammonia borane were carried out using the catalyst observed to be completely dry. The experimental set up for H₂ generation by the hydrogenation of ammonia borane is illustrated in Figure 1. Hydrolysis test system consists of circulating water bath, magnetic stirrer, jacketed tube, graduated burette and connecting hoses used for temperature control. The jacketed tube in the figure provides the test

environment. Graded burette was used to measure the released H₂ gas.

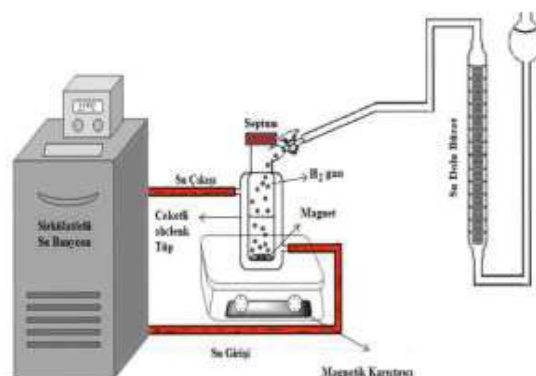


Figure 1. Hydrolysis reaction apparatus.

3. RESULTS AND DISCUSSION

3.1. NaOH Effect in solution medium

In this study, the first parameter measured for the ammonia borane catalytic reaction is the sodium hydroxide effect, which contains common ions and provides a positive effect on decomposition. The analyzed sodium hydroxide parameters are in the range of 1% and 7.5% by mass. The graph of the values showing hydrogen production of these environments were given in Figure 2. As seen in Figure 2, The most effective solution medium for hydrogen production is the environment with 5% (wt) NaOH solution.

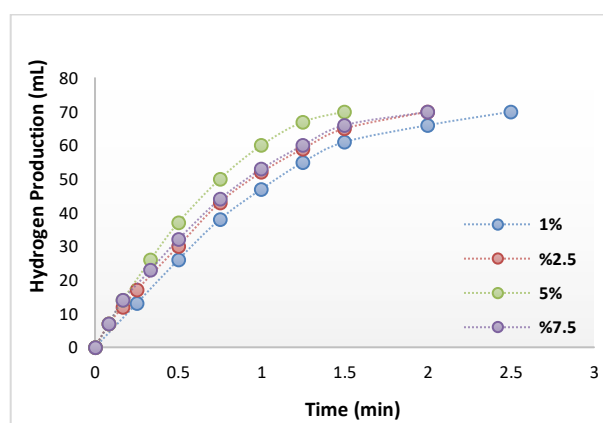


Figure 2. Effect of different NaOH concentrations on 30 °C, 25 mg Co₉₆-Cr₄-B catalyst, 1 mmole NH₃BH₃ solution

Depending on the change of NaOH concentration, that is, solution pH, it was determined that the hydrogen production rate, which was 2500 ml min⁻¹ g⁻¹ at 1% NaOH concentration, increased to 3478 ml min⁻¹ g⁻¹ at 5% NaOH concentration. In our study, we continued with 5% NaOH solution medium by mass as the solution medium in the next process.

3.2 Catalyst Amount

After determining the best NaOH (5% (wt) concentration value for the reaction medium, hydrogen production hydrolysis reactions based on catalyst amounts were carried out. The graph of the amount of hydrogen released due to catalyst amount was given in Figure 3. As seen in the graph, hydrogen production increased due to the increase of catalyst amount. This can be attributed to the increase in the amount of catalyst acting on ammonia borane.²⁰

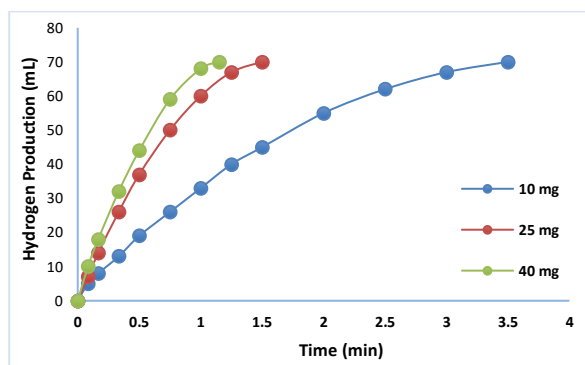


Figure 3. Hydrogen production in different catalyst amounts to 30 °C, Co₉₆-Cr₄-B catalyst, 1 mmole NH₃BH₃, 5% NaOH solution.

Considering the hydrogen production amount per catalyst, it was determined that the most effective hydrogen production rate was achieved with 10 mg of Co-Cr-B catalyst. As in the literature, subsequent experiments continued using 10 milligrams for the amount of catalyst, which is generally considered the lowest value.

3.3. Ammonia borane concentration

After determining the catalyst amount (10 mg) and NaOH 5%(wt) values of the solution, the substrate concentration having one of the most important effects on the hydrolysis reaction comes. At this stage of the study, hydrolysis reactions were performed with different NH₃BH₃ concentrations to determine the interaction between catalyst and substrate.

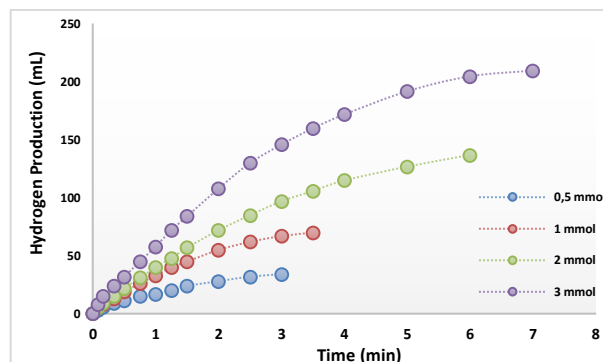


Figure 4. 30°C, 10 mg Co₉₆-Cr₄-B catalyst, hydrogen production at different concentrations of NH₃BH₃ to 5% NaOH solution.

These values are in the range of 0.5, 1, 2 and 3 mmole NH₃BH₃. Hydrogen production related to hydrolysis reactions carried out at different concentrations were given in Figure 4.

Considering the hydrogen production rate at different NH₃BH₃ concentrations, it was determined that the hydrogen production rate increased depending on the increase in concentration. The hydrogen production rate at a concentration of 3 mmole NH₃BH₃ was determined as 6071 ml g⁻¹ min⁻¹

3.4. Effect of temperature

One of the most important parameters studied for catalytic reactions is the temperature effect on the reaction. In this study, the graph of the examinations of the Co-Cr-B catalyst at different temperatures for the temperature effect of NH₃BH₃ hydrolysis was given in Figure 5. As seen in Figure 5, hydrogen production increases due to temperature increase. This is attributed to the effective collision theory that it is clear that particles with increasing temperature will interact more.

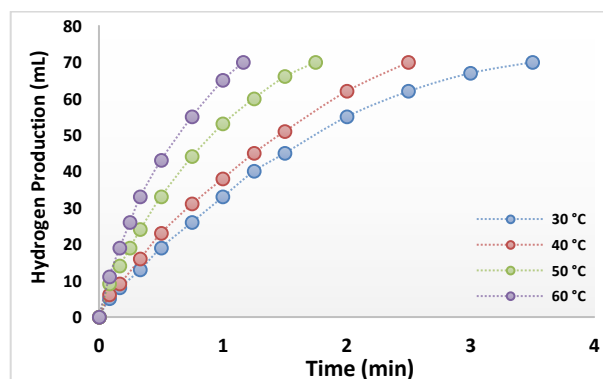


Figure 5. Hydrogen production in different concentrations of 258 NH₃BH₃ to 1 mmole NH₃BH₃, 10 mg Co₉₆-Cr₄-B catalyst, 5% (wt) NaOH solution.

3.5. Activation energy

The activation energy is one of the main parameters obtained from temperature experiments and is

determined according to the Arrhenius equation. The hydrogen production rate of ammonia borane hydrolysis catalyzed by the catalyst can be described by the Arrhenius equation (Eq. (2)).

$$\ln k = \ln A - E_a / RT \quad (2)$$

Here, R is the universal gas constant (8.314 kJ K⁻¹ mole⁻¹). K is the rate constant (min⁻¹). A is a constant known as the Arrhenius factor. T is absolute temperature (K). The values seen in Figure 5 are the data obtained from Figure 5. Based on the data obtained in Figure 5, when the 1/T graph is drawn against lnk as in Figure 6, the activation energy of the reaction (E_a) is 22.30 kJ mole⁻¹ when the slope value obtained is replaced in the Arrhenius equation given in Eq. (2). Using the same values, the reaction was determined to be 1st degree.

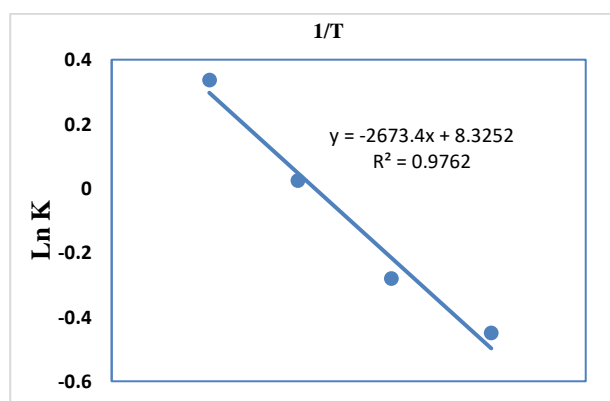


Figure 6. 1st order Arrhenius equation for the catalytic effect of Co₉₆-Cr₄-B catalyst to the NH₃BH₃ reaction

3. CONCLUSIONS

In this study, in which the catalytic effect of Co-Cr-B catalyst on ammonia borane hydrolysis was measured, the catalytic effective NaOH concentration for the solution medium was determined as the solution medium containing 5% NaOH by mass. In addition, it was positively evaluated that an effective hydrogen production rate was achieved by using only 10 mg of catalyst. The catalytic effective value, determined as the ammonia borane concentration, was determined as 3 mmole. As a result of the parameter evaluation of this study, the most effective hydrogen production conditions were achieved at 30°C in 5% NaOH solution by using 10 mg of catalyst at 3 mmole NH₃BH₃ hydrolysis value. At these values, the hydrogen production rate was determined as 6071 ml g⁻¹ min.

Conflict of interests

Authors declare that there is no a conflict of interest with any person, institute, company, etc.

REFERENCES

1. İzgi, M. S.; Şahin, Ö.; Onat, E.; Saka, C., *Int. J. Hydrog. Energy*, 2020, 45 (43), 22638-22648
2. Kazici, H. C.; Salman, F.; Izgi, M. S.; Şahin, Ö., *J. Electron Mater* 2020, 1-11.
3. Zeng, K.; Zhang, D. *Prog. Energy Combust. Sci.* **2010**, 36 (3), 307-326.
4. Kazici, H. C.; Yilmaz, S.; Sahan, T.; Yildiz, F.; Er, O. F.; Kivrak, H. *Front. Energy Res.* **2020**, 14(3) 578-589.
5. Balat, M., A global perspective. *Energ. Source. Part B: B* **2007**, 2 (1), 31-47.
6. Horoz, S.; Dai, Q.; Maloney, F.; Yakami, B.; Pikal, J.; Zhang, X.; Wang, J.; Wang, W.; Tang, J. *Phys. Rev. Appl.* **2015**, 3 (2), 11-24.
7. Gamborg, O. I.; Murashige, T.; Thorpe, T. A.; Vasil, I. K. *In vitro* **1976**, 12 (7), 473-478.
8. İzgi, M. S.; Şahin, Ö.; Ödemiş Ö; Saka, C. *Mater. Manuf. Processes* 2018, 33 (2), 196-201.
9. Şahin, Ö.; İzgi, M. S.; Onat, E.; Saka, C. *Int. J. Hydrog. Energy*, **2016**, 41 (4), 2539-2546.
10. Fernandes, R.; Patel, N.; Miotello, A. *Appl. Catal. B: Env.* **2009**, 92 (1-2), 68-74.
11. Ding, X. L.; Yuan, X.; Jia, C.; Ma, Z. F. *Int. J. Hydrog. Energy* **2010**, 35 (20), 11077-11084.
12. Huynh, K.; Napolitano, K.; Wang, R.; Jessop, P. G.; Davis, B. R. *Int. J. Hydrog. Energy* **2013**, 38 (14), 5775-5782.
13. Su, C. C.; Lu, M. C.; Wang, S. L.; Huang, Y.H. *RSC Adv.* **2012**, 2 (5), 2073-2079.
14. İzgi, M. S.; Şahin, Ö.; Saka, C. *Int. J. Hydrog. Energy* **2016**, 41 (3), 1600-1608.
15. İzgi, M. S. *Energ. Source. Part A* **2016**, 38 (17), 2590-2597.
16. İzgi, M. S.; Şahin, Ö.; Saka, C. *Mater. Manuf. Processes* **2019**, 34 (14), 1620-1626.
17. Jeong, S.; Kim, R.; Cho, E.; Kim, H. J.; Nam, S.-W.; Oh, I. H.; Hong, S. A.; Kim, S. H. *J. Power Sour.* **2005**, 144 (1), 129-134.
18. Salinas-Torres, D.; Navlani-García, M.; Kuwahara, Y.; Mori, K.; Yamashita, H. *Catal. Today* **2019**, (324),90-96.

19. Jia, H.; Chen, X.; Song, X.; Zheng, X.; Guan, X.; Liu, P. *Int. J. Energ. Res.* **2019**, 43 (1), 535-543.

20. Li, Y.; Li, S. *Int. J. Hydrog. Energy* **2020**, 45 (17), 10433-10441.



Antifungal effect of some essential oil combinations

Musa TÜRKMEN^{1*}, Durmuş Alpaslan KAYA¹

¹Hatay Mustafa Kemal University, Department of Field Crop, Hatay 31000, Turkey

Received: 17 April 2021; Revised: 14 May 2021; Accepted: 14 May 2021

*Corresponding author e-mail: turkmenmusa@hotmail.com

Citation: Türkmen, M.; Kaya, D. A. *Int. J. Chem. Technol.* 2021, 5 (1), 6-10.

ABSTRACT

In the present study, *in vitro* antifungal effect of the essential oils was examined against soil-borne (*Sclerotinia sclerotiorum*) pathogens. Essential oils obtained from *Foeniculum vulgare* and *Laurus nobilis* plants, naturally growing in the Hatay province, Turkey. The volatile phase of essential oils at different concentrations inhibited the mycelial growth in the dependent of dose. While the fungitoxic effect of essential oils was determined as 7.50 µL in laurel essential oil, it was determined as 5.0 µL in fennel essential oils. Laurel essential oils exhibited fungicidal effect at 15 µL whereas. Fennel essential oils exhibited fungicidal effect at 7.50 µL. The two essential oils were combined by 3 different techniques (manually combined oils; together distillation of oils; using solvent and combined oils) and were applied against *S. sclerotiorum* disease agents. As a conclusion, the results exhibited that laurel and fennel obtained separately by manually mixing with suitable combination of essential oils (M-F%75L%25) showed fungicidal effect at 5.0 µL; laurel and fennel essential oil obtained by distilling the mixture (T-F%75L%25) exhibited fungicidal effect at 3.75 µL concentrations and laurel and fennel essential oils with appropriate combination and mixture with hexane (S-F%75L%25) exhibited fungicidal effect at 3.75 µL. Antimicrobial activities revealed that the essential oils in appropriate combinations are more effective than their using alone against fungal disease agents.

Keywords: Antifungal effect, Essential oil, Fennel, Laurel.

Bazı uçucu yağ kombinasyonlarının antifungal etkisi

ÖZ

Bu çalışmada, Türkiye'nin Hatay ilinin farklı bölgelerinde doğal olarak yetişen *Foeniculum vulgare* ve *Laurus nobilis* gibi farklı bitkilerden elde edilen uçucu yağların, toprak kaynaklı fungal (*Sclerotinia sclerotiorum*) hastalık etkenlerine karşı *in vitro* antifungal etkinliği araştırılmıştır. Farklı konsantrasyonlardaki uçucu yağların buhar fazı, doza bağlı bir şekilde miselyal gelişimini inhibe etmiştir. *L. nobilis* uçucu yağlarının uçucu fazları 7.50 µL'de fungitoksik etki ve 15 µL'de fungisidal etki gösterirken; *F. vulgare* uçucu yağları 5.0 µL konsantrasyonda fungitoksik etki ve 7.50 µL'de fungisidal etki göstermiştir. İki uçucu yağ, 3 farklı yöntem kullanılarak karıştırılmış (elle iki uçucu yağ karıştırılmış; yağlar birlikte damıtılarak karıştırılmış ve çözücü kullanılarak karıştırılmış) ve *Sclerotinia sclerotiorum* patojenlerine karşı test edilmiştir. Sonuçlar, ayrı ayrı elde edilen *L. nobilis* ve *F. vulgare'* nin elle karıştırılmasıyla elde edilen uygun uçucu yağ kombinasyonunun (M-F% 75L% 25) 5.0 uL'de fungisidal etki gösterdiğini; *L. nobilis* ve *F. vulgare'* nin birlikte damıtılmasıyla elde edilen kombinasyonunun (T-F%75L%25) 3.75 µL konsantrasyonda fungisidal etki gösterdiğini ve *L. nobilis* ve *F. vulgare* uçucu yağlarının uygun kombinasyonunun hekzanla karıştırılmasıyla (S-F% 75L% 25) 3.75 uL'de fungisidal etki gösterdiğini ortaya koymuştur. Antimikrobiyal aktiviteler, uygun kombinasyonlardaki uçucu yağların mantar hastalık etkenlerine karşı tek başlarına kullanılmasından daha etkili olduğunu ortaya çıkarmıştır.

Anahtar Kelimeler: Antifungal Etki, Uçucu Yağ, Rezene, Defne.

1. INTRODUCTION

Food firms admit that shelf life, nutrition and microbial quality of food yield are important for them. Synthetic pesticides have been usually used to preserve food and

extend the shelf-life of food products. But these synthetic pesticides can rise health problems for consumers in a long term period.¹ Therefore food processors and consumers have expressed a wish to decrease the use of synthetic chemicals in food protection.²⁻⁵ Chemical

fertilizers should be applied at appropriate doses according to the programs prepared according to the results of the analysis of the control experts and high efficiency should be achieved by reducing the negative effects on the environment.⁶ In the selection of plant species and varieties, the ecological conditions of the region where the production will be made and the possibility of getting the diseases at the lowest level under these conditions should be taken into consideration.⁷ Extreme pesticide usage, which threatens ecological and human health in recent years, and increasing prices have created the need for alternative ways a fight with diseases.⁸ It has directed the researchers to the usage of essential oils and plant extracts due to their less negative effects on human health and environmental safety.^{9,10} The plants have been used by humans since the early ages for food, spices and medical purposes. The development in the pharmaceutical industry in parallel with chemistry in the 18th century, caused substitution of plants with synthetic and semi-synthetic materials.¹¹ Essential oils have long time served as flavoring agents in food and beverages. Recently, essential oils are taking increasing attention because of their antimicrobial effects.¹² Extract and essential oils that are obtained from plants in different ways, have been proved to have antifungal activities.¹³ Moreover, recently, several studies have been reported on the antifungal activity of essential oils against fungal pathogens¹⁴⁻¹⁷ and it was shown that the antifungal effects of essential oil depend on the composition of essential oils.¹⁸ Although there are numerous reports on the antifungal activities of essential oils, *in vitro* conditions¹⁹ there is no research devoted to the use of different methods of combination of essential oils. In this study; essential oils obtained from *Foeniculum vulgare* Mill and *Laurus nobilis* L which commonly grown in Hatay province^{20,21} and essential oils combinations obtained in different ways have been studied in *in vitro* conditions as means of an alternative way to chemical fight against *Sclerotinia sclerotiorum* fungal pathogen factor which is an important problem in plants.

2. MATERIALS AND METHODS

2.1. Plant material

In our study, the essential oils were obtained from the leaves of Laurel (*Laurus nobilis* L.) and the seeds of fennel (*Foeniculum vulgare* Mill.). Both plants have antimicrobial effects and they are naturally grown in Hatay province.

2.2. Essential Oil Extraction

Hydrodistillation was used for the plant material dried at room temperature. It was weighed and placed in a round bottom flask with a volume of distilled water (the solvent); Essential oils from dry *Laurus nobilis* L. plant

leaves and *Foeniculum vulgare* seeds were obtained by hydro distillation for 3 h with Clevenger's apparatus. The oils were separated, dried over anhydrous sodium sulphate and stored in an amber bottle at 4 °C until used.

2.3. Obtaining the Essential Oils mixtures

Three different methods have been adopted to obtain essential oil mixtures. Firstly, the *F. vulgare* and *L. nobilis* essential oils obtained separately in Clevenger have been mixed in specific ratios [*Foeniculum vulgare-Laurus nobilis* (75%-25%), (50%-50%), (25%-75%)], the essential oil mixtures obtained have been applied to *S. sclerotiorum* pathogen, planted onto Petri dishes, in different concentrations. Afterward, mixtures of *F. vulgare* and *L. nobilis* essential oils in suitable ratio have been obtained by putting them into carboys together at Clevenger evenly [*Foeniculum vulgare-Laurus nobilis*] and different concentrations of this mixture have been applied to pathogen.

Finally, the *F. vulgare* and *L. nobilis* essential oils obtained separately at Clevenger have been diluted separately with hexane at 2:1 ratio and by taking from *F. vulgare*-hexane and *L. nobilis*-hexane different volumes, mixtures in specific ratios [*F. vulgare-L. nobilis*] were obtained and further applied to *S. Sclerotiorum* pathogen.

2.4. Test of the Micro-organisms

The *S. sclerotiorum* used in this study was isolated from infected tomato stalks, which showed symptoms of Sclerotinia root rot. The surface disinfected sclerotia was coated by antibiotic modified potato dextrose agar. Plates were incubated at 20 °C for 5-7 days to allow growth of mycelium in the medium. Small agar blocks containing hyphal ends were cut at colony borders and transferred to potato dextrose agar (PDA). Replicate plates were incubated at 20 °C. The fungal isolate was re-inoculated into the tomato seedling and found to be highly pathogenic.⁹

2.5. Determination of the Antifungal Activities of Essential Oils

To determine the antifungal activities of essential oils from fennel and laurel plants and suitable mixtures of these oils, the culture of the 7-days old *S. sclerotiorum* isolate was placed in the center of the 9 cm diameter sterile Petri dish containing PDA medium (autoclaved for 15 minutes at 121 °C). *S. sclerotiorum* isolate was taken with a 5 mm fungus drill. Different doses of essential oils were added to sterile filter papers (10 mm diameter, Whatman No. 1) placed into Petri dishes. The Petri dish was covered with parafilm to prevent the loss of essential oils and incubated at 24-25 °C. Pure water was added to the Petri dishes. Evaluations were made by measuring colony radial growth diameters (in mm) when growth of fungi in the control Petri dish was completed. The

blocking ratio (%) at different concentrations of each essential oil was calculated according to Abbott formula.¹

$$\text{Blocking (\%)} = \frac{FGK - FGU}{FGK} \times 100$$

FGK = Fungal growth in control oils (mm)

FGU = Diameter of fungal growth in treated Petri dishes (mm)

2.6. Determination of the Fungicidal and Fungistatic Effect of Essential Oils

The *in vitro* antifungal volatile phase effects of essential oils against *S. sclerotiorum* were determined against mycelial growth. The single spore culture of each fungal isolates were grown on Potato Dextrose Agar (PDA) medium at 25°C for 3–5 days. In consequence, all the essential oils used in the experiments revealed not to have micelle development although the covers were replaced at the concentrations in which 100% interception was

plant essential oils on fungal micelle development, different concentrations of essential oils obtained from *Laurus nobilis* and *Foeniculum vulgare* plants and different concentrations of proper mixtures of these oils obtained via different methods have been applied on *S. sclerotiorum* pathogen to identify the volatile effects.

3.2. Activities of *Laurus nobilis* and *Foeniculum vulgare* Plant Essential Oils on Fungal Development

The results obtained for the experiments concerning the volatile effect of *Foeniculum vulgare* and *Laurus nobilis* essential oils are given in Table 1. As it is seen in Table 1, with the increase of the concentrations of essential oils, micelle developments of the funguses decrease. Comparing the two essential oils studied the results obtained showed that the essential oil of fennel was more inhibitory to *S. sclerotiorum* than laurel essential oil. As it can be seen in Table 1, *S. sclerotiorum* micelles covered the entire Petri dish (90 mm) in both applications

observed, hence it has been determined that essential oils effect on fungus at mentioned concentrations are fungicidal (completely disrupter, fatal).

2.7. Statistical analysis

All *in vitro* experiments were established according to a randomized plot design. The experiment was established with 3 replicates, each Petri dish being one repeat. This trial was repeated twice. The variance analysis was performed with one-way ANOVA using SPSS statistical program (SPSS Inc., version 11.5.0) without converting the obtained measurement values to % and the differences between the concentrations were determined by Duncan Multiple Comparison Test ($p \leq 0.05$).

3. RESULTS AND DISCUSSION

3.1. Activities of *Laurus nobilis* and *Foeniculum vulgare* Plant Essential Oils on Fungal Development

Within the study intended to research volatile effects of at control doses. In Table 1, the numbers represent the diameter covered by mycelial development. Micelle development was determined as 35.00 mm at 2.50 μL dose for fennel essential oil and it was determined that it inhibits 61.20% of micelle development. The micelle development of fungus at a dose of 3.75 μL of fennel essential oil was found to be 6.70 mm, and at this concentration, it was found that essential oil inhibits the micelle development of 92.56%. It was determined that the mycelial growth of the fungus was not seen at 5.00 μL dose of fennel essential oil meaning that this essential oil showed fungistatic effect and it can be concluded that fennel essential oil prevents the mycelial growth at this dose. Instead at the higher dose (7.5 μL) it has been determined that it shows fungicidal effect. When the effectiveness of laurel essential oil on micelle development was examined, it was determined that it showed fungistatic effect for a dose of 7.50 μL . and fungicidal effect for a dose of 15.00 μL .

Table 1. The activity of different essential oils at different doses on *S. sclerotiorum* micelle development

Essential oils		
Dose (μL)	<i>Foeniculum vulgare</i>	<i>Laurus nobilis</i>
0	90.00d	90.00
2.50	35.00cA	90.00B
3.75	6.70bA	90.00B
5.00	0.00aA*	90.00B
7.50	0.00a**	0.00*
10.00	0.00a	0.00*
12.50	0.00a	0.00*
15.00	0.00a	0.00**

*the dose showing fungistatic effect; ** the dose showing fungicidal effect; the rates in the column are the average of the rates in 3 different Petris dishes and they have been repeated at 3 different times. Small letters next to the rates in the same column (Difference between doses in the effectiveness of different doses of essential oils on micelle development) or capital letters next to the rates in the

same line (The difference between oils in the effectiveness of the same doses of fennel and laurel essential oils on mycelial development) shows that the differences among applications are not statistically significant (Duncan's Multiple Range Test, $p \leq 0,05$).

3.3. Determination of the Effectiveness of Essential Oils Mixtures on Micelle Development of Fungal Agents Under *in vitro* Conditions

As it can be seen from Table 2, with increasing concentrations of essential oils, the effectiveness of essential oils on the pathogen micelle development has increased. It has been observed that the mixture showing the most fungitoxic effect is the mixture containing more *Foeniculum vulgare* plant essential oil concentration. It was observed that the essential oil mixture obtained as a result of distillation of plants together (T) in the same bottom flask had more effect on mycelial growth at lower concentrations than the mixture with hexane solvent (S) and the essential oils obtained separately (M) from the plants. M-F%50L%50 and M-F%75L%25 essential oil mixtures showed fungistatic effect for a dose of 3.75 μL and fungicidal effect for a dose of 5 μL . M-F%25L%75

essential oil mixture showed fungistatic effect for a dose of 5 μL and 7.50 μL , while it showed fungicidal effect for a dose of 10 μL . T-F%50L%50 was found to have fungistatic effect for a dose of 3.75' μL while it was observed to have fungicidal effect for a dose of 5 μL . T-F%75L%25 essential oil mixture showed fungicidal effect for a dose of 3.75 μL . T-F%25L%75 essential oil mixture showed fungistatic effect the doses of 3.75 and 5 μL , while it showed fungicidal effect for a dose of 7.50 μL . S-F%50L%50 essential oil mixture showed fungistatic effect for the doses 3.75 and 5 μL , while it showed fungicidal effect for a dose of 7.50 μL . It was seen that S-F%75L%25 essential oil mixture had fungicidal effect for a dose of 3.75 μL while S-F%25L%75 essential oil mixture had fungicidal effect for a dose of 5 μL . The results that have been conducted to determine the volatile effects of essential oils are given in Table 2.

Table 2. Determination of the effectiveness of essential oils mixtures (F: *Foeniculum vulgare*, L: *Laurus nobilis*) on micelle development of fungal agents under *in vitro* conditions

Mixtures	Doses (μL)					
	0	2.50	3.75	5.00	7.50	10.0
M-F%50L%50	90.00c	11.67bA	0.00aA*	0.00a**	0.00a	0.00a
M-F%75L%25	90.00c	7.67bA	0.00aA*	0.00a**	0.00a	0.00a
M-F%25L%75	90.00d	59.00cD	31.33bC	0.00a*	0.00a*	0.00a**
T-F%50L%50	90.00c	9.33bA	0.00aA*	0.00a**	0.00a	0.00a
T-F%75L%25	90.00c	17.33bB	0.00aA**	0.00a	0.00a	0.00a
T-F%25L%75	90.00c	9.00bA	0.00aA**	0.00a*	0.00a**	0.00a
S-F%50L%50	90.00c	36.67bC	0.00aA**	0.00a*	0.00a**	0.00a
S-F%75L%25	90.00c	19.67bB	0.00aA**	0.00a	0.00a	0.00a
S-F%25L%75	90.00d	40.00cC	13.33bB	0.00a**	0.00a	0.00a

*the dose showing fungi static effect; **the dose showing fungicidal effect. The experiment has been repeated at 3 different times and the values in the column represents the inhibition rates and they are the average of the values obtained for 3 different Petri dishes. Capital letters next to the average inhibition rates in the same column (Difference between doses in the effectiveness of different doses of essential oils on micelle development) or small letters next to the rates in the same line (The difference between oils in the effectiveness of the same doses of fennel and laurel essential oils on mycelial development) show that the differences among applications are not statistically significant (Duncan's Multiple Range Test, $p \leq 0,05$).

4. CONCLUSIONS

This study suggests that essential oils have the potential for use in the control of soil-borne fungal disease agents such as *S. sclerotiorum*. It has been determined that essential oil mixtures show synergistic effect against pathogen and the effects of essential oil mixtures, especially the mixture obtained by distilling *Foeniculum vulgare* and *Laurus nobilis* plants together, on the development of pathogen are quite promising. The essential oils and their mixtures used in this study could be considered as potential alternatives for synthetic fungicides.

ACKNOWLEDGEMENTS

This work has been produced from the master thesis.

Conflict of interests

I declare that there is no a conflict of interest with any person, institute, company, etc.

REFERENCES

- Ghabraie, M.; Vu, K.D.; Tata, L.; Salmieri, S.; Lacroix, M. *LWT-Food Sci. Technol.*, **2016**, 66, 332-339.

2. Conner, D.E; Beuchat, L.R. *J. Food Sci*, **1984**, 49, 29–434.
3. Deans, S.G.; Ritchie, G. *Int.J. Food Microbiol*, **1987**, 165-180.
4. Beuchat, L.R.; Dillon, V.M.; Board, R.G., *CAB International Wallingford, UK*, **1994**, 167–180.
5. Delaquis, P.J.; Stanich, K.; Girard, B.; Mazza, G. *Int.J. Food Microbiol*, **2002**, 74, 101–109.
6. Çalık, A. *Gece Academy. Innovative Approaches in Agriculture, Forestry and Aquaculture Sciences*. **2018**, 101-105.
7. Çalık, A. *Turkish JAF Sci.Tech.*, **2020**, 8(3): 728-732.
8. Paster, N.; Bullerman, L.B., *Int.J. Food Microbiol*, **1988**, 7, 257–265.
9. Soylu, E.M.; Tok, M.F.; Soylu, S.; Kaya, A.D.; Evrendilek, G.A. *Pak. J. Biol. Sci*, **2005**, 8, 25-29.
10. Soylu, S.; Yigitbas, H.; Soylu, E.M.; Kurt, S. *Journal of Applied Microbiology*, **2007**, 103, 1021–1030.
11. Altinok-Yipel, F.; Yipel, M. *Türk Veteriner Hekimler Birliği Dergisi*, 2014, 1(2): 79-82.
12. Burt, S. *Int.J. Food Microbiol*, 2004, 94, 223–253.
13. Toroğlu, S.; Cenet, M. *KSÜ Fen ve Mühendislik Dergisi*, 2006, 9(2), 12-20.
14. Edris, A.E.; Farrag, E.S. *Nahrung/Food*, **2003**, 47, 117–121.
15. Kalembe, D.; Kunicka, A. *Curr. Med. Chem*, **2003**, 10, 813-829.
16. Pitarokili, D.; Tzakou, O.; Loukis, A.; Harvala, C. *J Agric Food Chem*, **2003**, 51, 3294–3301.
17. Kara, M.; Soylu, S.; Türkmen, M.; Kaya, D.A. *Journal of Tekirdag Agricultural Faculty*, **2020**, 17(2), 264-275.
18. Niculescu, O.; Gaidau, C.; Simion, D.; Daniela Berechet, M. *Revista De Chimie (Bucharest)*, **2020**, 71(1), 445-449.
19. Deleanu, M.; Popa, E.E.; Popa M.E. *Revista De Chimie (Bucharest)*, **2018**, 69(8), 1927-1933.
20. Koçer, O.; Ayanoğlu, F. *International Journal of Eastern Anatolia Science Engineering and Design*, **2021**, 3 (1), 72-88.
21. Ayanoğlu, F.; Kaya, D.; Koçer, O. *Int. J. Chem. Technol*, **2018**, 2 (2), 161-167.



Confirmation by molecular docking of the pharmacophore defined as 4D-QSAR using the MCET method for the 2-hydroxydiarylamide derivatives

Burçin TÜRKMEÑOĞLU¹, Yahya GÜZEL^{2*}

¹Department of Pharmaceutical Basic Sciences, Faculty of Pharmacy, Erzincan Binali Yıldırım University, Erzincan 24100, Turkey

²Department of Chemistry, Faculty of Science, Erciyes University, 38039, Kayseri, Turkey,

Received: 19 September 2020; Final revised: 11 November 2020; Accepted: 16 November 2020

*Corresponding author e-mail: yguzel@erciyes.edu.tr

Citation: Türkmenoğlu, B.; Güzel, Y. *Int. J. Chem. Technol.* 2021, 5 (1), 11-25.

ABSTRACT

For the 2-hydroxydiarylamide derivative series that inhibits serine proteases by mediating various events related to the basic processes of tumor invasion and metastasis in cancer, the pharmacophore (Pha) responsible for the activity was estimated by the Molecular Conformer Electron Topological (MCET) method. The atoms in the common core structure of the molecules and template are aligned so that the remaining oriented atoms superimposition with the maximum number. Pha; in the 4D-QSAR analysis, it is selected and used to represent the molecule that can interact best by the receptor among all conformers. The model proposed in the training set was verified in the external test set and the electronic identifying values of the Pha atoms in both sets were considered. With Leave One Out-Cross Validation (LOO-CV) the model proposed according to 33 molecules in the training set ($q^2 = 0.998$) was validated by using 8 molecules ($r^2 = 0.993$) in the external test set. As a result of the MCET method, the proposed pharmacophore structure was confirmed using molecular docking.

Keywords: 2-hydroxydiarylamide derivatives, Molecular docking, 4D-QSAR, MCET, Klopman index.

2-hidroksidiarilamid türevleri için 4D-QSAR'da MCET yöntemi kullanılarak belirlenen farmakoforun moleküler docking ile doğrulanması

ÖZ

Pb (Kanserde tümör istilası ve metastazının temel süreçleri ile ilgili çeşitli olaylara aracılık ederek serin proteazları inhibe eden 2-hidroksidiarilamid türevi serisi için, aktiviteden sorumlu farmakofor (Pha), Moleküler Konformer Elektron Topolojik (MCET) yöntemi ile tahmin edilmiştir. Moleküllerin ve şablonun ortak çekirdek yapısındaki atomlar ile diğer yönlendirilmiş atomlar maksimum sayı olacak şekilde üst üste hizalanır. 4D-QSAR analizinde, Pha grubu tüm konformerler arasında reseptör tarafından en iyi etkileşime girebilen molekülü temsil etmek için seçilir ve kullanılır. Eğitim setinde önerilen model harici test setinde doğrulanmış ve her iki setteki Pha atomlarının elektronik tanımlayıcı değerleri dikkate alınmıştır. Bir veri dışarıda bırakılarak çapraz doğrulama (LOO-CV) ile eğitim setindeki 33 moleküle göre önerilen model ($q^2 = 0.998$) harici test setinde 8 molekül ($r^2 = 0.993$) kullanılarak doğrulanmıştır. MCET yönteminin bir sonucu olarak, önerilen farmakofor yapısı moleküler docking kullanılarak doğrulanmıştır.

Anahtar Kelimeler: 2-hidroksidiarilamid türevleri, Moleküler docking, 4D-QSAR, MCET, Klopman indeksi.

1. INTRODUCTION

Cancer is one of the most important health problems of our time. The aim of cancer treatment is to kill tumor cells in a manner that minimizes damage to the surrounding cells. Apoptosis (programmed cell death) is a physiological process that is commonly used in the

treatment of cancer, allowing cells to be killed without producing an inflammatory response.¹ 2-hydroxydiarylamide family has been reported to have a variety of interesting biological properties, including fungicidal, antiviral and bactericidal activities.² However, the inhibitory activity of the 2-hydroxydiarylamide series against any serine protease in

cancer has not been previously reported in the literature. Despite this, it has been reported to be the strongest preventive activity against over-expression of colon cancer cells. Transmembrane protease/serine 4 (TMPRSS4) has been reported in the literature.² TMPRSS4 is a type II transmembrane serine protease (TTSP), is a member of the family and has been found to be highly expressed in many cancers. TMPRSS4 is a new type II transmembrane serine protease that is highly in vivo on the cell surface in pancreatic, thyroid, colon and other cancerous tissues.³ Recently, type II transmembrane serine proteases (TTSP) have been recognized as a novel sub-family of serine proteases that have an extracellular proteolytic region, a transmembrane region, and a short cytoplasmic region.⁴⁻⁷ In previous studies, TMPRSS4 was found to be associated with cell migration, invasion, epithelial mesenchymal transition and stage progression in colon, metastasis and colorectal cancer cells.⁸⁻¹⁰ The 2-hydroxydiarylamide derivative series and TMPRSS4 synthesized by researchers have been shown experimentally for a good inhibitory activity, evaluated to inhibit serine protease activity and suppress cancer cell invasion.²

Advances in computational chemistry in drug design have provided an important basis for the discovery of new drug candidates for biological activity.¹¹ In addition to the structure and function of the target, both ligand and structure-based studies are conducted to understand the mechanism by which it interacts with potential drugs.¹² Both methods play a vital role in modern drug design because it is a much cheaper and faster alternative to discovery.

Recently, both the 4D-Quantitative Structure Activity Relationship (4D-QSAR) method and the molecular docking approach for multiple conformers have been proposed to overcome drug discovery challenges.¹³

The primary goal of this study is to propose the pharmacophore (Pha) model of the newly synthesized 2-hydroxydiarylamide compounds² by Klopman index 4D-QSAR analysis developed by us for the first time and to use the molecular docking method to confirm this model.

2. METHODS

The methods used in this study are given below according to the order of operation.

- SPARTAN'10 model molecular modeling program (Wavefunction, Irvine, CA, USA) for quantum chemical calculations; "Molecular Modeling" is used to represent or imitate molecules' lifelike behavior with all theoretical and computational methods.
- ETM program to convert quantum chemical results to Electron Topological Matrix (ETM); To

characterize molecular systems in 3D, atomic characters originating from molecular modeling methods were stored in matrix form for each conformer.

- The interaction points of the pharmacophore between the Ligand-Receptor (L-R) were determined by the descriptor type with the MCET program in the QSAR method, which is the most used in Ligand-based drug design calculations.
- FlexX docking program was used to calculate and observe binding interaction between L-R.

2.1. Quantum chemical calculations

Molecular conformational optimization was performed using Spartan'10 (Wavefunction, Irvine, CA, USA) using molecular mechanical field approach and quantum chemical calculations with B3LYP/6-31G level method. The conformers of a compound that are like each other are aligned to a common structure and recognized to avoid reuse. In the same compound, the high energy conformers were canceled due to their low population according to the Boltzmann distribution, and those with the lowest energy were included in the study. Of these conformers, only one that is most compatible with the receptor structure is considered responsible for the activity to represent the molecule. 41 compounds consisting of 2-hydroxydiarylamide derivatives as the anti-metastasis agent under investigation is taken from the literature and given in Table 1.²

2.2. Electron topological matrix program (ETMP)

The Electron Topological Matrix (ETM) of each conformer is a mathematical indicator where the conformer is represented by spatial and atomic descriptor numerical values. After the results obtained from the calculations in the quantum chemistry are recorded as Cnfrmr_No.txt file, the electronic values of atoms are Natural, Mulliken and Electrostatic charges, HOMO/LUMO orbital coefficients, Fukui index (f⁺, nucleophilic and f⁻, electrophilic functions) distances are converted into ETM with our in house software ETM program. The rows and columns of this matrix are ordered with the same index atoms. While the topological distance between different atoms is the descriptor electronic values between the same atoms, the upper triangular matrix is given in the diagonal region of the ETM. The non-diagonal values of the matrix, the distance between the atoms and the length of the bond will not change, so the conformer's space structure will remain the same. Accordingly, the descriptors of different genera used in diagonal values are represented by the corresponding values of atoms in the upper lines of the diagonal matrix and the descriptor name at the end of the line. Thus, the two-dimensional ETM is transformed into a three-dimensional matrix with the same distances and different descriptors as in Figure 1.

Table 1. Compound structures of 2-hydroxydiarylamide derivative series

Mol. No	Mol. Structures	Mol. No	Mol. Structures
n01		n22	
n02		n23	
n03		n24*	
n04*		n25	
n05		n26	
n06*		n27	
n07		n28	

Table 1. Continued

n08		n29	
n09		n30	
n10*		n31	
n11		n32	
n12*		n33	
n13		n34	
n14		n35*	

Table1. Continued

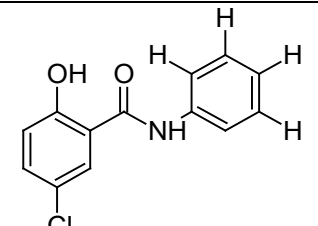
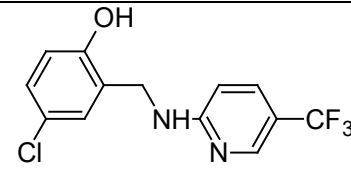
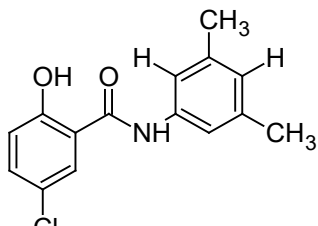
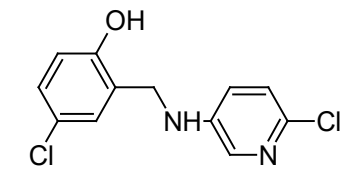
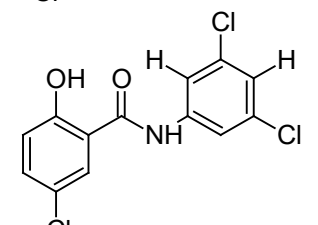
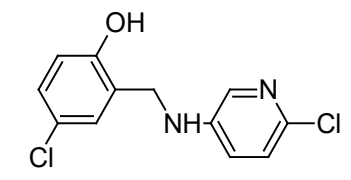
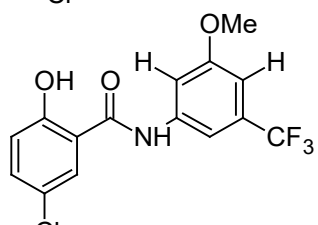
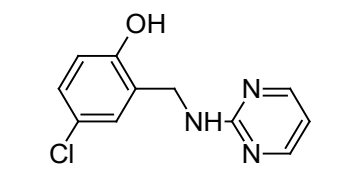
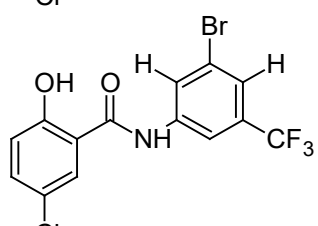
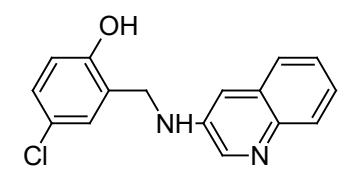
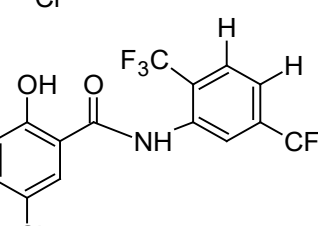
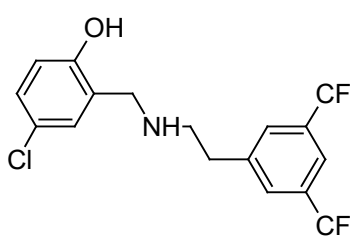
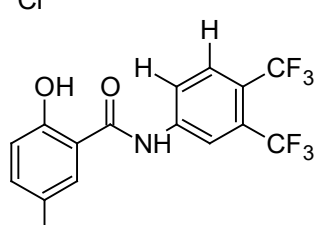
n15		n36*	
n16		n37	
n17		n38	
n18		n39	
n19*		n40	
n20		n41	
n21			

Table 2. Cartesian coordinate of the conformer n01_01.

Atom	X	y	Z
O2	0	0	0
N1	2.2841	0	0
C5	1.0195	4.9372	0
C6	-0.135	4.2161	0.246
O1	-1.299	2.1881	0.4297
C3	2.2411	2.8757	-0.325
C1	-0.133	2.8101	0.2077
C7	1.067	0.636-	0.022
C4	2.2088	4.259	-0.297
C2	1.0822	2.1212	-0.051
C8	2.5627	-1.38	0.0101
C9	3.3013	-4.093	0.0224
C10	1.5791	-2.375	-0.094
C11	3.9094	-1.752	0.1204
C12	4.2709	-3.097	0.1245
C13	1.9631	-3.715	-0.084
C14	0.9014	-4.786	-0.13
F1	-0.229	-4.353	-0.723
F2	0.5691	-5.199	1.113
F3	1.3288	-5.874	-0.806
C15	5.732	-3.464	0.17
F4	5.9284	-4.682	0.7121
F5	6.2711	-3.485	-1.069
F6	6.4455	-2.572	0.8936
H7	3.0965	0.5909	0.1005
H1	-1.138	1.2184	0.2988
Cl1	3.6678	5.1748	-0.65

Although the coefficients of the boundary orbitals in the atomic charges, Fukui index and ETM are optionally changed, the non-cross values do not change because the conformer's skeletal structure is constant. In the two-dimensional ETM shown in [Figure 1](#), diagonal values are given by electrostatic charges and non-diagonal values, bond length or distance between atoms. If different diagonal values are used instead of the electrostatic

charge value, a new two-dimensional ETM is created while the non-diagonal values remain constant. A three-dimensional matrix is formed with each successive ETM. It is possible to show this three-dimensional matrix in two dimensions, as shown in [Figure 1](#), when the non-cross values are unchanged, and the cross values are given in separate lines.

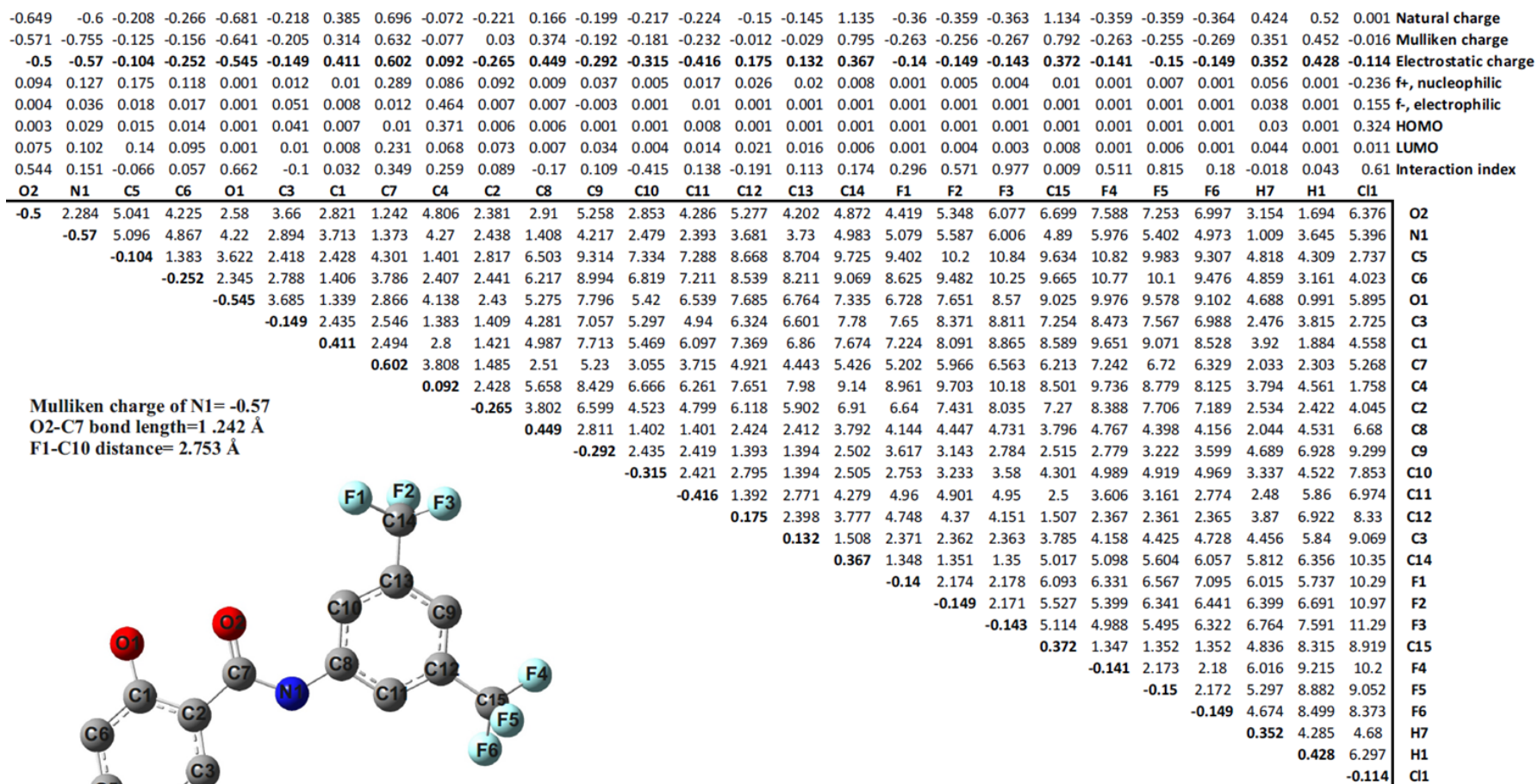


Figure 1. Three-dimensional ETM is represented by the same non-diagonal and different diagonal values.

For each conformer, the three-dimensional upper triangular matrix of the remaining atoms is found, ETM.txt, and for the sake of simplicity, except for functional atoms such as O, N, S in the molecular skeleton, the hydrogen atoms bound to carbon atoms are ignored. Then, for each conformer, the three-dimensional upper triangular matrix is as ETM_txt, and the Cartesian coordinates keep the x-, y-, z-values (Table 2) as Cart_txt in the files. Coordinates of the first three atoms; Other coordinate values are arranged as in Table 2 with reference to (0,0,0), (x, 0,0) and (0, y, z). For each Pha experiment, this process is applied to the coordinates of the remaining atoms, referring to the first three atoms of the nucleus structure being made similar 'zero'. Thus, all atoms of each ligand are brought to the appropriate and common positions relative to the receptor with maximum overlap and real 3D interaction is provided

2.3. MCET Method

MCET program¹⁴⁻²¹ written by GÜZEL is used to operate 3D/4D-QSAR methods. Like CoMFA/CoMSIA, it works on the principle of aligning and matching atoms in ligands. common core structure in all molecules that are part of the pharmacophore can form the beginning of pairing. The electronic and geometric similarities of conformer atoms in the molecules align according to the proposed core structure. According to the core structure, the conformer with the maximum number of atoms matching the template is chosen to represent its molecule. However, it is possible to select representatives of different conformer structures for each of the core structures derived from the template conformer. First, the electronic and geometric similarity of the atoms in the molecular nucleus structure, depending on their tolerance values, is a good start for both the aggregation of the atoms in the molecules and the determination of the pharmacophore structure. Significant difference of our method from the above two methods:

i. Molecules are placed in the grid by overlapping with the template conformer instead of using the reference volume tolerance dt value instead of grid spacing.

ii. It is extremely useful to know the active conformation of the drug receptor complex for drug design to be effective. Therefore, in order to explain the interactions between L-R, it is important to predict this conformer which is responsible for the activity for each molecule. Since there is a dynamic balance between conformers, the reduction in the amount of compatible conformer held by the receptor is compensated by others, and the penetration rates of the molecules remain the same according to the Boltzmann distribution. As discussed herein, the interaction of multiple conformers with the receptor results in 4D-QSAR.

iii. The conformer compatible with the receptor may not always be at the lowest energy level. One of the conformers of any molecule that best matches the

template is used to determine Pha, as it will be in the optimal position for interaction with the receptor.

iv. Recently, different local reactive descriptor (LRD) has been used as chemical properties responsible for ligand-receptor interaction to predict a ligand-based model. The energy resulting from the interaction points between the L-R varies depending on the type and value of the LRD selected in the program interface. Mulliken / Natural / Electrostatic atomic charges, HOMO / LUMO coefficients, Fukui index and Klopman index are used as LRD type atoms in the interface of the MCET program.^{16, 17, 22} With the descriptors used in the MCET method, research can be conducted with different series showing preventive properties, especially cancer. In other words, with these LRDs, the compounds studied on anticancer can be screened, as well as the activities of the compounds that will inhibit other diseases can be calculated in detail. The aggregation of atoms depends on the LRD types. Since the LRD type, an independent variable in the ligands, changes, an aggregation of different clusters will occur due to different alignment and different overlap. In order to determine the structure of the binding site of the 3D receptor more realistically, the LRD type should be chosen well. Therefore, the established model may be close to reality. A good model cannot be created using a wrong identifier. A good LRD selection is required to get a better Pha. In determining the Pha of a molecule, different types of probes are used as descriptors in CoMFA/CoMSIA, while the electronic properties of atoms in MCET are used in ETM with different LRD types. One of the LRDs we use as the descriptor is more effective than the probe used in CoMFA / CoMSIA. Because multiple probes are required to define an interaction point, a single descriptor (e.g. Klopman index) used as LRD in MCET is ionic (positive / negative), hydrogen bond (donor / acceptor) is examined by many features such as non-polar interactions. More realistic results can be achieved with the more comprehensive and general descriptor used in our software MCET method.

The steps of the algorithm operated in MCET are summarized as follows.^{16, 17, 22}

- The simplest and least compatible molecule are selected as a template because it is considered one of the most compatible with the receptor.
- Groups consisting of combinations of 3, 4, 5 or 6 atoms containing at least one functional atom are the starting or core structure (CS) of the active structures.
- At least one active molecule conformer should contain this CS. This is determined by the tolerance given by the defining values of the atoms in the formula and the coordinate values in space. Accordingly, it is ordered from the number of molecules to the minimum number of CS.
- Using a tolerance slightly greater than the spatial geometric tolerance applied to CS, the positions of

the oriented atoms in the conformers of all molecules are overlapped with the atomic positions of the template conformer. The tolerances used for both CS and spatial positions vary in specific increments, so overlaps are checked for suitability of all molecules. The optimum tolerance value is determined by the best overlap.

- The conformer having the largest number of atoms matching the atoms in the template conformer is selected to represent other conformers in its molecule.
- The reference positions are taken from the atoms of at most and least active molecules. The conformers of the selected molecules containing the atoms in these positions are aligned to be superposition.
- At the positions in space, the receptor-side interaction parameter values corresponding to this position are calculated using the descriptor values of the atoms of the clustered molecules. Here, the descriptor types of atoms are natural, Mulliken, electrostatic atomic charges; the coefficients or Fukui indexes in HOMO/LUMO have used, as well as the Klopman index, which was first introduced by us to the literature. As expected in this study, Klopman index gave better results. The reason for this is that a more realistic analysis can be performed because the Klopman index not only involves the atomic charge but also the coefficients in the boundary orbitals. An important detail to consider when using the Klopman index is; if the HOMO coefficients of the ligand are used, the LUMO coefficients of the receptor are used and the receptor that provides the electron in the ligand serves as the hydrogen. HOMO or LUMO of the ligand can be selected as the descriptor, or one of the atomic charges (natural, Mulliken and electrostatic) can be selected. The Klopman index, natural-HOMO, natural-LUMO, Mulliken-HOMO, etc., from each combination of these selections different descriptors can be created.
- Positions which may be interaction points are determined by Genetic Algorithm (GA). The model is matured by adding new positions to the CSs discussed with this algorithm. Whether a new position can be added to the position of the model is determined by a significant increase in the statistical value. The positions in the resulting model show the superposition of the ligands, including the CSs, but reveal the pharmacophore structure of the receptor as a negative image of these positions. The CS in the superposition constitutes a common structure in which each molecule interacts with the receptor, while the remaining directed atoms act as enhancer or reducing activity. Each molecule is determined to increase or decrease the activity relative to its atomic descriptor value at that position.
- By aligning the CSs of the molecules, the greatest number of matching atoms of the conformer that

will interact best with the receptor helps to select the most compatible one. Therefore, the most accurate structure of the CS is found by accurately overlapping the conformers.

- Those involved in the interaction between the clusters of superimposed atoms can give rise to superposition and may be independent variables of the model. The terms align, superimpose and superposition used in QSAR investigations are expressed separately in MCET although they are used interchangeably.
- Adding a new position within the models is determined by someone who has the best statistical result with PLS measurements. PLS calculations are treated as NLLS because the interaction energy resulting from the ligand-receptor pharmacophore structure is used as a model in non-linear equality. For each CS and NLLS calculations of clusters of oriented atoms, the best statistical results are obtained for the most appropriate tolerance values. The tolerance values during the clustering of each CS and molecules carrying atoms and atoms around it, the limit that is possible is rated from minimum to maximum. NLLS calculations are performed using the Levenberg-Marquardt algorithm.
- Molecules are divided into two as training and test set by Gaussian process. This process ensures that the molecules in the test set are best represented by those in the training set. In order to do this, there must be an agreement between the independent variables of the molecules in both sets. A machine learning algorithm including the Gauss process uses the similarity between points to estimate the value of an unseen point in the test set, utilizing the training data. The activity of each molecule is validated according to q^2 values with the model proposed by using LOO-CV in the training set. The activities of the molecules in the excluded test set are predicted by using the same model. ^{16, 17, 22}

As a result, the steps processed within the MCET method; selection of template conformer, alignment of CSs and selection of molecular conformers from superimposed atoms around it, clustering of molecules, separation of training and test sets according to GP, suggestion of the model with GA, superposition of calculation of activities with non-linear equality and determining q^2 and r^2 values by using PLS in LOO-CV. ^{16, 17, 22}

Energy calculations in biological interaction are a long and difficult question in practice. To solve this problem, the energy contribution of L-R interaction and the selected conformational energy contribution of molecular conformers are handled together. Conversion of conformers of the same molecule in a selected conformer can be achieved by energy intake or application. The receptor binding energy of conformers should be higher during conversion between conformers. Thus, a

conformer may represent other conformers within the molecule to interact with the receptor. One of the most important features that distinguish MCET from others is the interaction of a single conformer with the most suitable receptor. Another feature of our method is that it can use LRDs such as atomic charge, Fukui index and HOMO/LUMO coefficients as well as the Klopman index introduced by you. They provide information about the electronic structures of molecules that interact with the receptor.

2.4. Partial least squares (PLS) analysis

The partial least squares statistical method used in the derivation of 4D-QSAR models is an extension of the multiple regression analysis where the original variables are replaced by a small set of linear combinations. In this study, the PLS method with Leave One Out-Cross Validation (LOO-CV) was used to determine the optimal number of components using the cross-validation coefficient q^2 . External validation of the various models was performed using a test set of five molecules. The final analysis was performed using the optimal number of components obtained from to obtain the correlation coefficient (r^2). The value of q^2 determines the internal predictability of the model, while the value of r^2 evaluates the internal consistency of the model. Thus, the best QSAR model was chosen based on the values of q^2 and r^2 .

2.5. Klopman Index

We first introduced the Klopman-Salem equation used to describe the regional/stereo selective reactions as a new local reactive descriptor and used the equation²³⁻²⁶ to demonstrate ligand-receptor interaction. Therefore, we have given the name of "Klopman's Index" in a similar way to another LRD. A new molecular orbital, ψ_{AB} , is formed from the linear combinations ψ_A and ψ_B orbitals by using c_a and c_b weight coefficient between two separate (A and B) molecules. For a simple Lewis acid-base ($A + B \rightarrow AB$) reaction, how the wave function ψ_{AB} is calculated in Klopman and Jensen perturbation molecular orbital (MO) theory is given in Eq.(1).

$$\psi_{AB} = c_a\psi_A + c_b\psi_B \quad (1)$$

According to the Klopman-Salem equation, the energy gain (or loss) can be calculated when the corresponding atoms of the two separate compounds interact with electrostatic and covalent, separately or both. The detailed form of the Eq.(2) is given below.²³⁻²⁶

$$\Delta E = -\sum_{a \in A, b \in B}^n (q_a + q_b)\beta_{ab} S_{ab} + \sum_{k \in A, l \in B}^n \left(\frac{Q_k Q_l}{\epsilon R_{kl}} \right) + \frac{\sum_{r \in A}^{occ} \cdot \sum_{s \in B}^{unocc} - \sum_{s \in B}^{occ} \cdot \sum_{r \in A}^{unocc}}{\sum_{E_r - E_s} \cdot \frac{2(\sum_{a \in A, b \in B}^n c_{ra} c_{sb} \beta_{cb})^2}{E_r - E_s}} \quad (2)$$

A and B are interacting molecules n is number of interaction points between two molecules q_a is the electron population in the atomic orbital a_i , $i = 1, 2, 3 \dots n$ β and S are resonance and overlap integrals Q_k is the total charge on atom k ; ϵ is the local dielectric constant R_{kl} is the distance between the atoms k_i and l_i , c_{ra} is the coefficient of atomic orbital a_i in molecular orbital r , (r refers to the molecular orbitals on one molecule). E_r is the energy of molecular orbital r .

$$\Delta E \approx \sum_1 \left(\frac{Q_{nuc} Q_{elect}}{\epsilon R_i} \right) - 2 \sum_1^n \frac{(c_{nuc, i} c_{elect, i} \beta_i)^2}{E_{LUMO(elec)} - E_{HOMO(nuc)}} \quad (3)$$

For the interaction between the ligand and the receptor as nucleophiles and electrophiles in the binary system, the first term of Eq. (3) means Coulombic repulsion or attraction, while the second term in Eq. (3) refers to the contribution in the frontier orbital term. Q_{nuc} and Q_{elec} represent atomic charges, c_{nuc} and c_{elec} orbital coefficients, R distance between atoms, ϵ local dielectric constant, β resonance integrals, E_{HOMO}/E_{LUMO} cross-frontier energy values.

During the interaction of the ligand and the receptor, the distance between the ligand and the receptor, the dielectric constant, and the values Kappa (κ) and Xi (ξ) of the position points in the receptor field are continuously given in both terms, and Kappa and Xi can be summed up as constants respectively.

The output of the model is a non-linear function arising from atomic descriptors on the ligand and adjustable constants in the receptor domain. In order to find a model that gives a good statistical result, a significant correlation of the adjusted constants calculated according to the observed activity values should be ensured. The statistical results of experimental and predicted efficiency values were calculated by NLLS method. Estimated activity values can be determined after the adjustable constants of all positions in the receptor area are calculated at the same time.

2.6. Molecular docking

Molecular docking techniques are often used to investigate how drugs, drug candidates, enzymes, nucleic acids, and receptor proteins in computer-aided rational drug design fit together.^{27, 28} In these docking studies, the binding energy of the three-dimensional receptor can be determined and the binding site between the ligand-receptor can be visualized. This can be useful for understanding the type of attachment and for designing smaller, more compatible ligands targeting proteins.²⁹

Table 3. Observed and predicted activities of 41 2-hydroxydiarylamide derivatives.

Mol.No	Obs.(pKi)	Pred.(pKi)	Mol.No	Obs. (pKi)	Pred.(pKi)
n01	1.960	1.960	n22	1.520	1.495
n02	1.000	1.098	n23	1.460	1.471
n03	1.890	1.876	n24*	1.460	1.452
n04*	1.540	1.489	n25	1.550	1.545
n05	1.920	1.867	n26	1.800	1.829
n06*	1.920	1.913	n27	1.890	1.884
n07	1.550	1.582	n28	1.120	1.064
n08	1.540	1.529	n29	1.920	1.934
n09	1.920	1.920	n30	2.000	2.020
n10*	1.720	1.730	n31	2.220	2.217
n11	1.000	1.019	n32	1.000	1.005
n12*	1.000	1.014	n33	1.000	1.007
n13	1.000	1.005	n34	1.000	1.015
n14	1.410	1.406	n35*	1.000	0.951
n15	1.300	1.379	n36*	1.100	1.141
n16	1.410	1.421	n37	1.000	1.009
n17	1.720	1.666	n38	1.000	0.990
n18	1.800	1.823	n39	1.000	1.009
n19*	1.920	1.875	n40	1.000	1.000
n20	1.700	1.653	n41	1.070	1.052
n21	1.890	1.891			

*Compounds in the test set

Molecular docking was applied to investigate molecular scavenging using a patented search engine to place a scoring function and ligands in the binding site of a protein. The crystal structure of the Tmprss4 receptor from the RCSB Protein Data Bank (PDB ID: 5CE1). The ligands enter the bonding zone with the FlexX docking. All the water molecules in 5CE1 were deleted and polar hydrogen atoms were added.

In this article we implemented automatic docking. The 5CE1 structure was used in subsequent docking experiments without energy reduction. FlexX docking was used to visualize the binding mode between protein and ligand.

3. RESULTS AND DISCUSSION

The data set is divided into two groups, 33 compounds are selected as training set and 8 compounds as test set. Observed and predicted activities of all compounds in training and test sets are given in Table 3. This dataset was used to construct the 4D-QSAR (MCET) model and to analyze its physicochemical properties. In the molecular docking calculations were made according to the molecule.

3.1. MCET results

Tmprss4 has been reported to be used as an active target in cancer treatment by minimizing cancer spread in the body.² Established the role of Tmprss4 serine proteolytic effect in tumor cell invasion, it has been shown to be a novel approach in the treatment of malignant tumors.² In order to use pKi values in activity calculations, inhibitor Ki (nM) values were arranged as log (1 / Ki) on a negative logarithmic scale. In the study,

data sets of 41 compounds with structural diversity were divided into training test sets with 33 and 8 compounds, respectively. The test set consists of approximately 20% of the whole set, ensuring that it contains representative samples of the training set and the range of activity values of the training set. For both the training and test sets, the activities calculated by the MCET method were compared to the experimental results obtained from the article. Accordingly, activity calculations, Klopman index, Fukui index, Natural, Mulliken and Electrostatic charges were made with different descriptors and the statistical results are shown in Table 4.

Table 4. The values of q^2 and r^2 according to different descriptors. (The descriptor with the best results is marked in bold.)

Descriptors	q^2	r^2
Natural Charge	0.822	0.465
Mulliken Charge	0.870	0.757
Electrostatic Charge	0.832	0.685
N_Fukui (f+)	0.863	0.824
P_Fukui (f-)	0.981	0.995
HOMO	0.920	0.913
LUMO	0.932	0.867
Natural HOMO Klopman	0.996	0.986
Mulliken HOMO Klopman	0.995	0.991
Electrostatic HOMO Klopman	0.998	0.993
Natural LUMO Klopman	0.995	0.991
Mulliken LUMO Klopman	0.997	0.996
Electrostatic LUMO Klopman	0.993	0.994

Pha information of the descriptor which gives the best statistical result is given in Table 5.

Table 5. Klopman index using predicted Pha atoms and parameter constants (The atomic positions of CS are shown in italics).

Mol. No	Atom No	x, y, z Cartesian Coord.			Position letters	Kappa-(κ) Values	Xi-(ξ) Values
		x	Y	z			
<i>n01_01</i>	<i>O2</i>	<i>0</i>	<i>0</i>	<i>0</i>	<i>a</i>	-0.059	-0.2120
<i>n01_01</i>	<i>O1</i>	<i>2.5810</i>	<i>0</i>	<i>0</i>	<i>b</i>	-0.186	-1.0120
<i>n01_01</i>	<i>C12</i>	<i>-4.7550</i>	<i>2.2890</i>	<i>0</i>	<i>c</i>	-0.110	-5.9390
n02_04	C15	3.7070	1.9950	0.8160	d	0.4930	39.9290
<i>n02_04</i>	<i>N1</i>	<i>-1.2090</i>	<i>2.0160</i>	<i>0.7430</i>	<i>e</i>	0.2150	11.1940
n02_04	C11	1.2080	1.9760	0.6950	f	0.5020	-4.2760
n02_04	C1	-3.9010	1.0920	-1.6680	g	0.4570	27.3150
n02_04	F1	1.088	-2.037	-2.149	h	0.066	7.0660
n12_04	F6	4.418	-2.329	1.297	i	1.339	-0.8660
n13_02	C3	1.907	1.862	-2.233	j	0.449	0.9980
n13_02	C13	2.054	-3.352	1.609	k	-1.079	-2.3240
n02_04	C3	-1.602	1.652	-2.210	l	-0.231	-8.3280
n02_04	F3	2.337	-2.716	-0.504	m	0.941	3.558
n11_01	C11	-2.800	3.890	-0.115	n	-0.163	15.459
n12_04	C17	-2.139	-0.136	-1.006	o	-0.618	-5.754
n12_04	C10	4.389	2.103	-0.959	p	0.713	-28.826
n01_01	F4	-6.835	3.236	-0.615	r	0.026	-34.854
n29_03	H1	1.066	-1.466	1.622	s	-0.340	-8.486
n02_04	F2	0.164	-2.765	-0.321	t	0.323	-5.353
n11_01	C15	-4.569	5.625	-0.391	u	0.513	-5.473
n12_04	F5	6.526	-2.014	0.844	v	-0.676	-1.508
n32_03	O2	-1.486	-0.033	1.914	y	0.198	-0.138

Herein, according to the MCET method, the positions of the reference molecules from which Pha is obtained are marked with a, b, c and other letters according to the cartesian coordinate values of the corresponding atoms. These letters are the geometric information of the interaction areas of Pha and the Kappa and Xi parameters of the corresponding receptor are calculated. Although the Kappa constant contains the charge value of the corresponding atom in the receptor, the constant Xi is the coefficient of the atom. At these points given as a, b, c and so on between L-R, either the pulling force or the pushing force occurs due to negative or positive markings of both the ligand and the receptor. As can be seen from

Eq. (3), in the first term, for atomic charges, if both sides are the same marked, the pulling force arises if the thrust is marked differently. On the other hand, if the coefficients in the second term are in the same sign, if the tensile force is in the different sign, the thrust force occurs. These forces have a greater effect due to the greater absolute value of the numbers in Kappa and Xi.

L-R complex parameters; the descriptor is the structure and receptor of CS with distance tolerance values. The structure of CS, which is one of the interaction points shown in Figure 2, is given by points a, b, c and e.

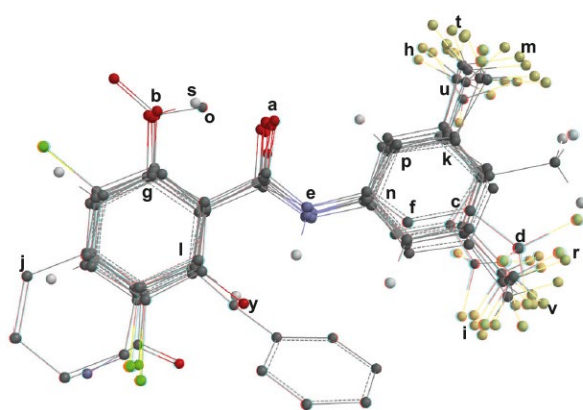


Figure 2. Superimposition of n01, n02, n11, n12, n13, n29 and n32 molecules determination of Pha.

The first three atoms of each candidate CS (called a, b and c) are aligned with the starting points (0,0,0), (x, 0,0) and (x, y, 0). The positions of the remaining atoms in the conformation are rearranged according to the Cartesian coordinate values of x, y and z. Thus, the atoms of all ligands having coordinate values in space may interact with the directed points of the receptor position.

Using two different tolerance values, only the CS atoms are aligned with respect to the position tolerance value in the remaining set of directed atoms. The similarity and identity of CS atoms is the source of interaction with the receptor. Direct and indirect combinations are made between clustered positions. First, r^2 (regression coefficient for all ligands) values are calculated for the first three atoms and for the best of CS. It is then debatable which of the clustered positions should be chosen as the fourth argument. For this purpose, each position is used as a candidate and is designated as the fourth position leading to the greatest increase in r^2 . Similarly, the fifth, sixth and subsequent interaction points with the best r^2 values were included in the model. In this study, the points of interaction consisting of 22 positions with the letters a, b, c are given in Figure 2.

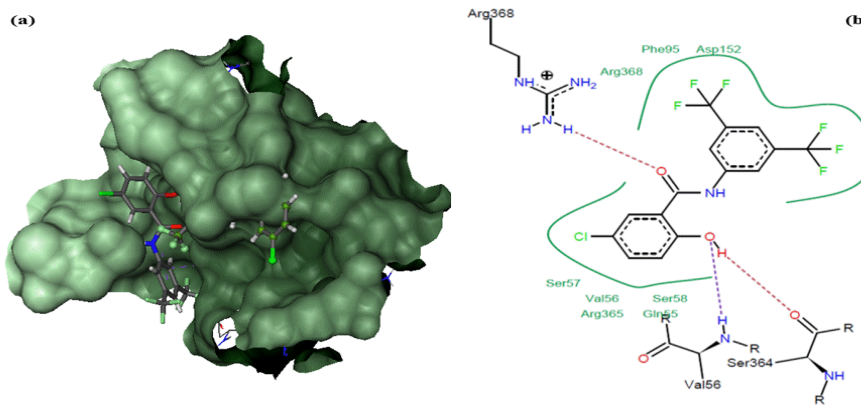


Figure 4. (a) Interaction between receptor-ligand. (b) Interaction diagram of the selected conformation selected for the highest activity molecule in the active site of the TRSSP enzyme.

Based on MCET descriptors, a 4D-QSAR model was proposed to explain and predict the effects of substituents on the metastatic activity of 41 compounds on hydrophobic, electrostatic, steric, donor and receptor domains. The predicted activities of the molecules in the training and test set were shown with statistical values, and the accuracy of the established model was proven to be a measure of these values. A model was confirmed with statistical results for 41 molecules using Klopman index values ($q^2 = 0.998$, $r^2 = 0.993$). The predicted strength of the model found by the MCET method is confirmed in an external test set and is shown in Table 3 with the molecules marked "*". During modeling, the compounds in the training set were used outside the test set. The 3D model, validated by the activities of the ligands in the internal test set, was used to estimate the ligands in the external test set. The graph values between the estimated and observed activities using the model for both sets are shown in Figure 3.

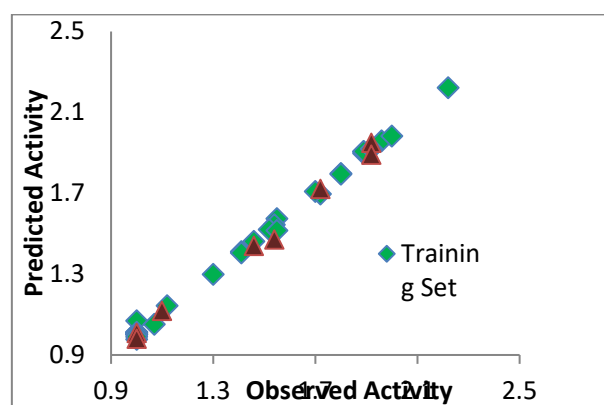


Figure 3. Observed and predicted activity graph of training and test sets.

3.2. Molecular docking results

Molecular docking was performed to investigate the stability of the previously formed 4D-QSAR model and to the interaction between the molecule (n30) and the TMRSS4 enzyme (PDB ID: 5CE1) and was shown in Figure 4.

4. CONCLUSIONS

4D-QSAR was used to investigate the structure-activity relationship of new 2-hydroxydiarylamide derivatives as a metastasis inhibitor. 4D-QSAR calculations have been developed by using a receptor-affected and representing others among multiple conformers. The Klopman index, which was first used as a new LRD descriptor in QSAR calculations, could be applied in the MCET method as a simplified formula. This new descriptor shows higher statistical results than other typical LRD descriptors. This descriptor, which includes both atomic charges and atomic coefficients in boundary orbitals, can be safely used in L-R interactions. Not only statistically high results are enough, but also exactly confirmed by docking. Molecular docking was performed according to the serine protease enzyme. Primarily from the protein data bank (PDB: 5CE1) TMPRSS4, the proteins acting on were tested one by one starting with the lowest RMSD value. The binding affinity with the FlexX docking program was found to be $\Delta G = -11.42$ kcal/mol.

ACKNOWLEDGEMENTS

This work was financially supported by Erciyes University Scientific Research Projects (BAP) of Turkey (Grant no. FDK-2016-6547).

Conflict of interests

Authors declare that there is no a conflict of interest with any person, institute, company, etc.

REFERENCES

- World Health Organization. WHO "Cancer" February 2006 Retrieved on 2009-02-12
- Kang, S.; Min, H. J.; Kang, M. S.; Jung, M. G.; Kim, S. *Bioorg. Med. Chem. Lett.* **2013**, *23*, 1748-1751.
- Min, H. J.; Lee, M. K.; Lee, J. W.; Kim, S. *Biochem. Biophys. Res. Commun.* **2014**, *446*, 1-7.
- Hooper, J. D.; Clements, J. A.; Quigley, J. P.; Antalis, T. M. *J. Biol. Chem.* **2001**, *276*, 857-860.
- Netzel-Arnett, S.; Hooper, J. D.; Szabo, R.; Madison, E. L.; Quigley, J. P.; Bugge, T. H.; Antalis, A. M. *Cancer Metastasis Rev.* **2003**, *22*, 237-258.
- Szabo, R.; Wu, Q. Y.; Dickson, R. B.; Netzel-Arnett, S.; Antalis, T. M.; Bugge, T. H. *Thromb. Haemost.* **2003**, *90*, 185-193.
- Szabo, R.; Bugge, T. H. *Int. J. Biochem. Cell Biol.* **2008**, *40*, 1297-1316.
- Kim, S.; Kang, H. Y.; Nam, E. H.; Choi, M. S.; Zhao, X. F.; Hong, C. S.; Lee, J. W.; Lee, J. H.; Park, Y. K. *Carcinogenesis* **2010**, *31*, 597-606.
- Larzabal, L.; Nguewa, P. A.; Pio, R.; Blanco, D.; Sanchez, B.; Rodriguez, M. J.; Pajares, M. J.; Catena, R.; Montuenga, L. M.; Calvo, A. *Br. J. Cancer.* **2011**, *105*, 1608-1614.
- Jung, H.; Lee, K. P.; Park, S. J.; Park, J. H.; Jang, Y. S.; Choi, S. Y.; Jung, J. G.; Jo, K.; Park, D. Y.; Yoon, J. H.; Park, J. H.; Lim, D. S.; Hong, G. R.; Choi, C.; Park, Y. K.; Lee, J. W.; Hong, H. J.; Kim, S.; Park, Y. W. *Oncogene.* **2008**, *27*, 2635-2647.
- Ou-Yang, S. S.; Lu, J. Y.; Kong, X. Q.; Liang, Z. J.; Luo, C.; Jiang, H. L. *Acta Pharmacol. Sin.* **2012**, *33*, 1131-1140.
- Lionta, E.; Spyrou, G.; Vassilatis, D. K.; Couronia, Z. *Curr. Top. Med. Chem.* **2014**, *14*, 1923-1938.
- Andrade, C. H.; Pasqualoto, K. F. M.; Ferreira, E. I.; Hopfinger, A. J. *Molecules* **2010**, *15*, 3281-3294.
- Kizilcan, D. S.; Turkmenoglu, B.; Guzel, Y. *Struct Chem* **2020**, *31*, 1339-1351
- Alp Tokat, T., Türkmenoğlu, B., Kızılcan, D. Ş., Güzel, Y. *J. Mol. Model.* **2019**, *25*, 1-13.
- Turkmenoglu, B.; Guzel, Y. *Comput. Biol. Chem.* **2018**, *76*, 327-337.
- Guzel, Y.; Aslan, E.; Turkmenoglu, B.; Su, E. M. *Curr. Comput-Aid. Drug.* **2018**, *14*, 207-220.
- Yilmaz, H.; Boz, M.; Turkmenoglu, B.; Guzel, Y. *Trop. J. Pharm. Res.* **2014**, *13*, 117-126.
- Yilmaz, H.; Guzel, Y.; Onal, Z.; Altiparmak, G.; Kocakaya, S. O. *Bull. Korean Chem. Soc.* **2011**, *32*, 4352-4360.
- Türkmenoğlu, B., Yılmaz, H., Su, E.M., Alp Tokat, T. Güzel, Y. *Int.J. Chem. Technol.* **2017**, *1*, 14-23.
- Su, E. M., Turkmenoglu, B., Guzel, Y. *Int. J. Innov. Stud. Sci. Eng. Technol.* **2016**, *02*, 67-75.
- Turkmenoglu, B.; Guzel, Y.; Su, E.M.; Kizilcan, D. S. *Mater. Today Commun.* **2020**, *25*, 101583
- Klopman, G. *J. Am. Chem. Soc.* **1968**, *90*, 223-243.
- Salem, L. *J. Am. Chem. Soc.* **1968**, *90*, 543-552.
- Salem, L. *J. Am. Chem. Soc.* **1968**, *90*, 553-566.

26. Fujimoto, H., Fukui, K. *In Chemical Reactivity and Reaction Paths*, John Wiley&Sons: New York, 1974.

27. Jain, A. N. *J. Comput. Aid. Mol. Des.* **2007**, *21*, 281-306.

28. Spitzer, G. M.; Wellenzohn, B.; Laggner, C.; Langer, T.; Liedl, K. R. *J. Chem. Inf.* **2007**, *47*, 1580-1589.

29. Holt, P. A.; Chaires, J. B.; Trent, J. O. *J. Chem. Inf. Model.* **2008**, *48*, 1602-16158. Ghorbani, M.; Seyedin, O.; Aghamohammadhassan, M. *J. Environ. Manage.* **2020**, *254*, 109814-109919.



The activity of ceria supported complex in hydrogen generation

Dilek KILINÇ^{1,*}, Ömer ŞAHİN²¹ University of Siirt Faculty of Science and Arts Department of Chemistry, Siirt, Turkey² University of Siirt Faculty of Engineering, Department of Chemical Engineering, Siirt, Turkey

Received: 22 June 2020; Revised: 26 April 2021; Accepted: 26 April 2021

*Corresponding author e-mail: dkilinc@siirt.edu.trCitation: Kılınç, D. ; Şahin, Ö. *Int. J. Chem. Technol.* 2021, 5 (1), 26-32.

ABSTRACT

In this study, we studied the ceria supported Ni complex preparation and using it as a catalyst in NaBH₄ hydrolysis for H₂ production. NaBH₄ hydrolysis system was studied in different parameters, as concentration of Ni complex, concentration of NaBH₄, concentration of NaOH, amount of catalyst and temperature. Additionally, catalyst was characterized by several analysis methods. Finally, the kinetic calculation of NaBH₄ hydrolysis reaction was studied at 20 °C-50 °C the activation energy was found to be 27.581 kJmol⁻¹. The aim of this study is to emphasize that ceria support can be used to increase the catalyst surface and to obtain the high hydrogen generation activity through hydrolysis of NaBH₄. The experimental results show that ceria supported Ni complex was an effective catalyst in hydrolysis of NaBH₄.

Keywords: Ni-complex, Sodium borohydride, Hydrogen generation.

1. INTRODUCTION

Hydrogen is a renewable energy sources which deliver sufficient energy that was clean and environmentally friendly.¹ But, two important impediments are present to hydrogen generation and storage for using hydrogen. Due to its H₂ evolution at low temperature, great 10.8 % H₂ content, delivered non-toxic byproducts and stability in alkaline solutions NaBH₄ is commonly used.²



The use of heterogeneous catalysts was considered one of the ways to control the hydrolysis of NaBH₄.³ NaBH₄ hydrolysis reaction is controlled by different noble or

Seryum oksit destekli kompleksin hidrojen üretimindeki aktivitesi

ÖZ

Bu çalışmada, seryum oksit destekli Ni kompleksinin hazırlanışını ve NaBH₄ den hidrojen üretiminde katalizör olarak kullanılışını inceledik. seryum oksit destekli Ni kompleks katalizli NaBH₄ hidroliz reaksiyonu; NaBH₄ ve NaOH konsantrasyonuna, sıcaklığa, katalizör miktarına ve katalizör içerisindeki Ni kompleksinin konsantrasyonuna bağlı olarak çalışıldı. Ayrıca sentezlenen katalizör farklı analiz yöntemleriyle karakterize edildi. Son olarak da 20 °C-50 °C sıcaklık aralığında sodyum borhidrürün hidroliz reaksiyonunun kinetik verileri incelendi, reaksiyonun aktivasyon enerjisi 27.581 kJmol⁻¹ olarak bulundu. NaBH₄ hidrolizinde seria destekli Ni kompleksinin etkin bir katalizör olduğu görüldü.

Anahtar Kelimeler: Ni-kompleks, Sodyum borhidrür, Hidrojen üretimi.

non-noble metal (Pt, Ru, Pd Co, Ni, and Cu) catalysts in many forms.⁴⁻¹¹

To improve of the catalyst different studies have been tried.¹²⁻¹⁵ Between them a different support materials using is started to attract attention and be widely used.^{16, 17} Typical catalyst supports include TiO₂¹⁸⁻²⁰, Al₃O₂²¹⁻²³, MgO²⁴, clays²⁵, SiO₂^{26, 27}, CeO₂²⁸, activated carbon²⁹, etc... Though activated carbon is a good support material, the fabrication of activated carbon is expensive since it requires high-temperature values. Ceria support (CeO₂) is important material in hydrogen generation due to its storage performance, reducing activation energy and effect of oxygenation.³⁰⁻³²

Herein, the Ni complex (4-4'-methylenebis-(2,6-diethyl) aniline-3,5-di-tert-butylsalisylaldimine-Ni)³³ was used to supported on ceria and the catalytic effects was

investigated on sodium borohydride hydrolysis for hydrogen production. The catalytic studies were realized by different parameters at 30 °C. The aim of this study is to emphasize that ceria support can be used to increase the catalyst surface and to obtain the high hydrogen generation activity through hydrolysis of NaBH₄. The experimental results show that the ceria supported Ni complex was an effective catalyst in hydrolysis of NaBH₄. Moreover, ceria supported Ni complex catalyst was characterized with BET, FT-IR, XRD and SEM.

2. MATERIALS AND METHODS

2.1. Materials

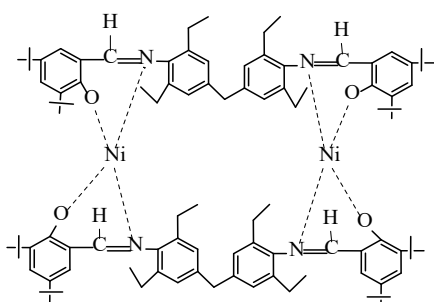
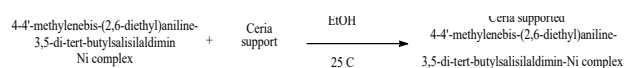
All solvents: chloroform (CHCl₃), methyl alcohol (CH₃OH), ethyl alcohol (CH₃CH₂OH), and the main chemicals: NiCl₂·6H₂O, 4-4'-methylenebis-(2,6-diethyl)aniline, 3,5-ditertbutylsilylaldehyde, and cerium oxide, NaBH₄, NaOH were purchased from Merck and they were used without applying any purification.

Infrared spectrum was measured in the range of 4000-400 cm⁻¹ on a PerkinElmer Spectrum 100 FTIR (ATR sampling accessory) spectrophotometer. With using Rigaku X-Ray diffractometer, the XRD patterns were determined. By using Brunauer–Emmett–Teller (BET) surface area measurement the important surface area parameters were identified. SEM results were determined with JEOL JSM 5800.

2.2. Methods

2.2.1. Synthesis of ceria Supported-Ni complex

By using mechanical mixing techniques ceria supported Ni complex catalyst was prepared. With varied amount of Ni complex was dissolved in ethanol (10 mL). Then 0.1 g ceria was added in this solution and stirred 72 h before filtration. In Figure 1 preparation of ceria supported Ni complex catalyst was shown.



4-4'-methylenebis-(2,6-diethyl)aniline-3,5-di-tert-butylsilylalimine-Ni complex

Figure 1. Preparation of Ceria supported Ni complex

2.2.2. Catalytic sodium borohydride hydrolysis reaction

Catalytic hydrogen generation system occurred from 0.01 g catalyst that including 5 % Ni complex, with 10 % NaOH in 10 mL 2.0 % NaBH₄ solution at 30 °C. The generated hydrogen amount was measured by using graduated cylinder. The proposed hydrogen volume is 560 mL for Equation 1.

3. RESULTS AND DISCUSSION

3.1. The influence of different parameters on the catalytic activity of ceria Supported-Ni complex in hydrogen generation

To research influence of NaOH concentration on the H₂ generation, different NaOH concentrations from 0 to 10 % were tried with using ceria supported-Ni complex catalyst, while the concentration of 2 % NaBH₄ at 30 °C. The hydrogen generation rates increased as 8193.60; 8343.40; 11550.20; 14123.00; 16535.40 mL H₂ g_{cat}⁻¹ min⁻¹ in order of 0 %, 5 % 7 %, and 10 % NaOH and the reaction times decreased (Figure 2). In this study, H₂ production rates increased with the increasing concentration of NaOH.

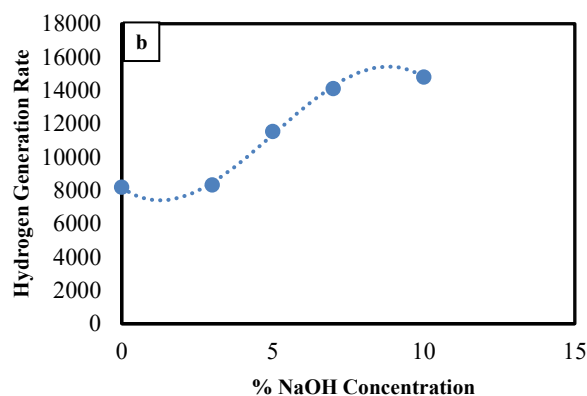
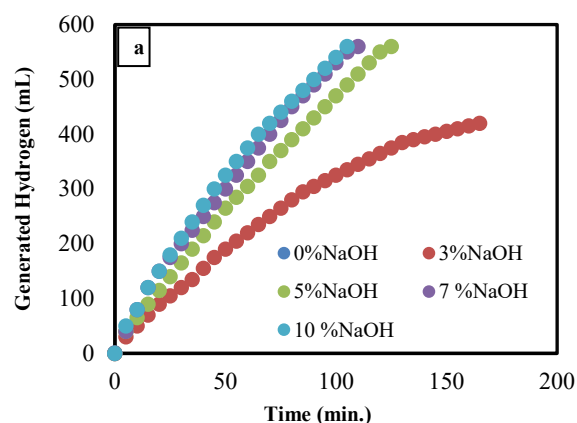


Figure 2. a) Influence of NaOH concentration, b) Graph of % NaOH concentration to hydrogen generation rate (in 2 % NaBH₄, 0.01 g catalyst at 30 °C)

To investigate the influence of Ni complex concentration in hydrogen generation, 5%, 10%, 15%, 20% Ni complex concentrations were tried. For ceria supported Ni complex and tried in hydrogen generation reaction (Figure 3).

In Figure 3, it is seen that with increasing Ni complex concentration hydrogen generation rates were started to decrease as 16535.40; 7540.40; 5560.53; 4758.15 mL H₂ g_{cat}⁻¹min⁻¹ from 5 % to 20 % Ni complex

concentration. In this study, hydrogen generation rates decreased with the increasing concentration of Ni complex concentration in ceria supported Ni complex catalyst. The lower values from 5 % was also investigated with 4 % Ni complex concentration, but surprisingly hydrogen generation rate was become to decrease to 16402.50 mL H₂ g_{cat}⁻¹min⁻¹ with generated 500 mL hydrogen. So that for this study % 5 Ni complex was preferred to use in ceria supported Ni complex catalys

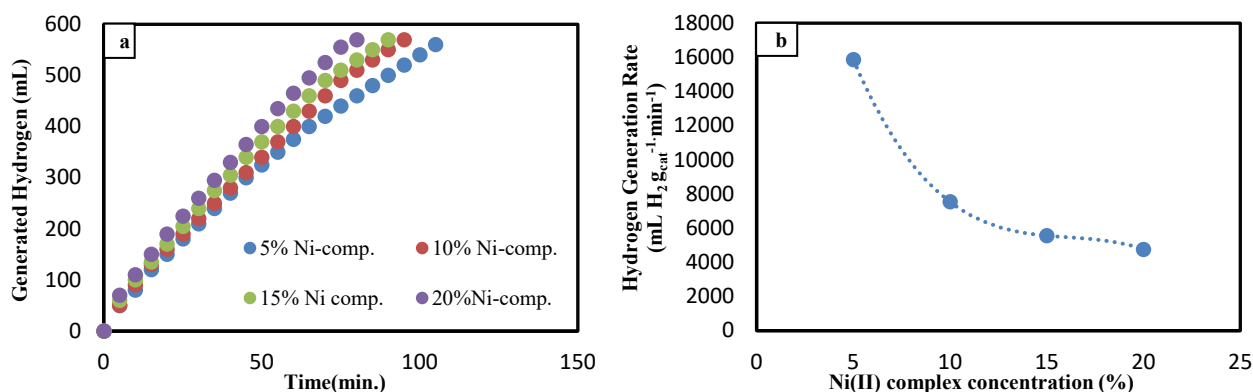


Figure 3. a) Influence of Ni complex concentration in hydrogen generation b) Graph of % Ni concentration to hydrogen generation rate (in 2 % NaBH₄, 10 % NaOH, 0.01 g catalyst at 30 °C)

The effect of catalyst amount on hydrogen generation rate was investigated with several ceria supported Ni complex catalyst amounts as 0.005, 0.01, 0.025, and 0.05 g including 5% Ni complex in 2 % NaBH₄ and 10 % NaOH solution at 30 °C and the results are seen in Figure 4. As seen from Figure 4, there is an opposite ratio towards the H₂ generation rates and amounts of catalyst

as 20452.00; 16535.40; 6140.00; 3569.00 mL H₂ g_{cat}⁻¹min⁻¹. So that, H₂ generation rates decreased with amounts of supported Ni complex increasing due to the catalyst surface saturation. However, 0.005 g catalyst has the best hydrogen generation rate (20452.00), the predicted hydrogen volume is not provided (490 mL). So it was decided that the suitable catalyst amount is 0.01 g for this reaction (560 mL).

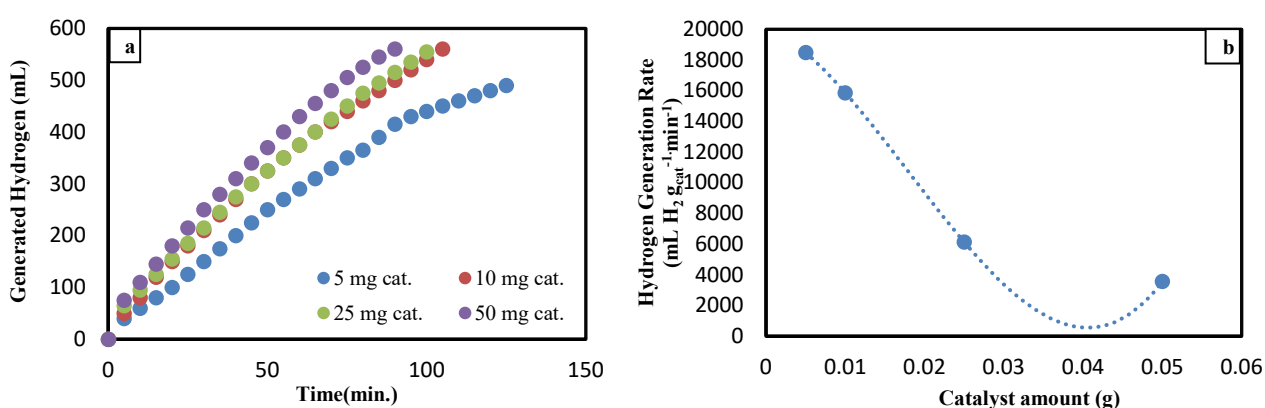


Figure 4. a) Influence of catalyst amount in hydrogen generation b) Graph of catalyst amount to hydrogen generation rate (in 2 % NaBH₄, 10 % NaOH at 30 °C)

In order to check the sodium borohydride concentration on H₂ generation rate, the different concentration of NaBH₄ as 2 %, 5 %, 7 %, 10 % was tried in 10 % NaOH solution with 0.01 g ceria supported Ni complex at 30 °C. Ceria supported Ni complex was highly active catalyst,

despite the improving NaBH₄ percentage as shown in Figure 5. There was any important difference in H₂ generation rates as NaOH concentration increased. It was shown that ceria supported Ni complex catalyzed NaBH₄ hydrolysis was not depend on NaBH₄ amount.

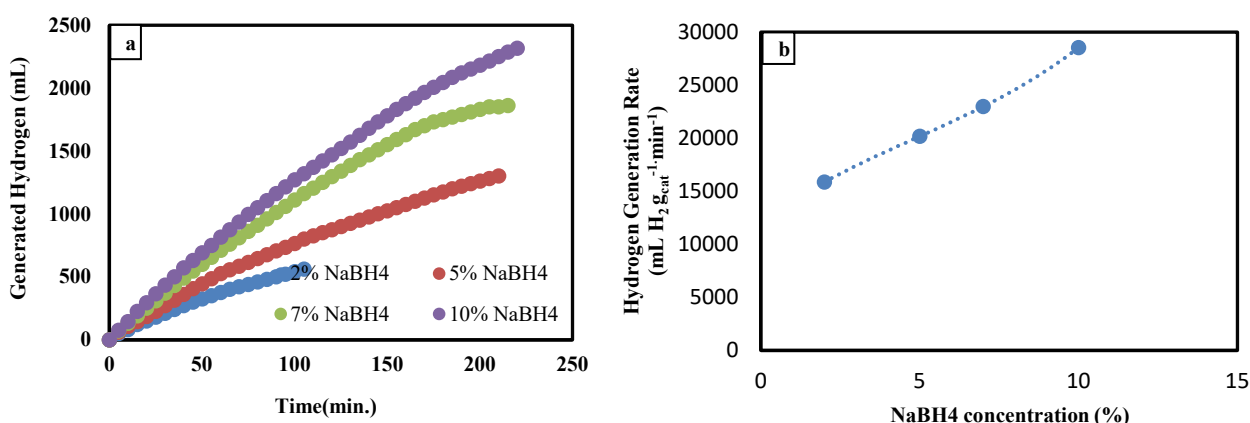


Figure 5. a) Influence of NaBH₄ concentration in hydrogen generation b) Graph of % NaBH₄ concentration to hydrogen generation rate (in 10 % NaOH, 0.01 g catalyst at 30 °C)

To research the effect of temperature on hydrogen generation rates, the studies were carried out at different temperatures as 20, 30, 40, 50 °C with 2 % NaBH₄ and 10 % NaOH solution and 0.01 g ceria supported-Ni

complex catalyst. As shown in Figure 6 the hydrogen production rates increased with increasing reaction temperature as 8571.00; 16535.40; 20772.00; 23320.00 mL H₂ g_{cat}⁻¹ min⁻¹ respectively.

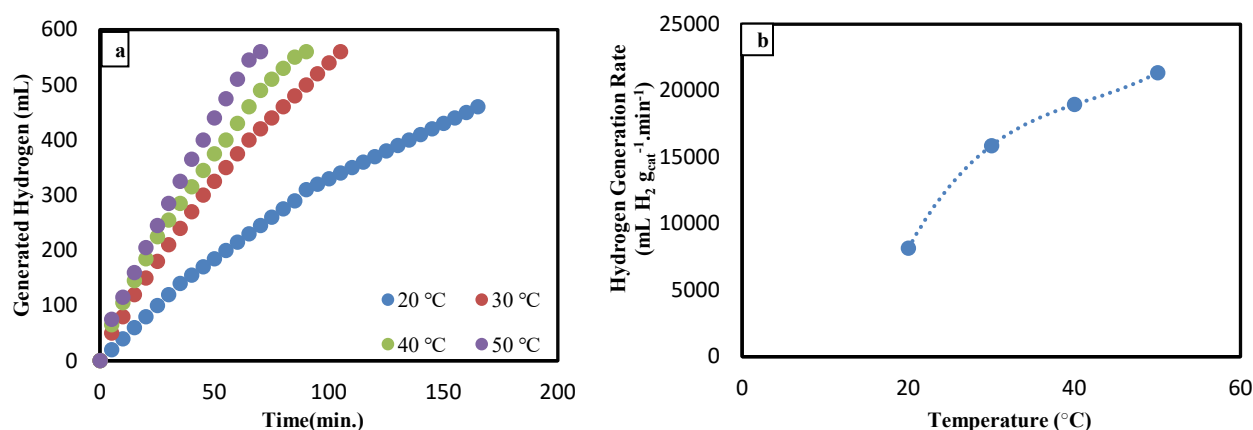


Figure 6. a) Influence of temperature on the hydrogen generation b) Graph of different temperatures to hydrogen generation rate (in 2 % NaBH₄, 10 % NaOH, 0.01 g catalyst)

3.2. Kinetic studies of hydrogen generation

Kinetic studies of ceria supported Ni complex catalyzed hydrogen generation reaction are described from nth order reaction equation as;

$$-r_{\text{NaBH}_4} = -\frac{dC_{\text{NaBH}_4}}{dt} = k \cdot C_{\text{NaBH}_4}^n \quad (2)$$

Separating and integrating, we obtain:

$$-\int_{C_{\text{NaBH}_4 0}}^{C_{\text{NaBH}_4}} \frac{dC_{\text{NaBH}_4}}{C_{\text{NaBH}_4}^n} = k \int_0^t dt \quad (3)$$

$$\frac{1}{(n-1)} \left(\frac{1}{C_{\text{NaBH}_4}^{n-1}} - \frac{1}{C_{\text{NaBH}_4 0}^{n-1}} \right) = kt \quad (4)$$

$$\frac{1}{C_{\text{NaBH}_4}^{n-1}} = (n-1)k \cdot t + \frac{1}{C_{\text{NaBH}_4 0}^{n-1}} \quad (5)$$

In Equation 5 the reaction rate order, n was recorded as 0.25. From Figure 7 the rate constants, k was obtained. A linear curve was displayed in Figure 8 with Plotting Ln (k) versus to (1/T).

$$k = A \exp(-E_a / RT) \quad (6)$$

The activation energy (E_a) was recorded as 27.581 kJ mol⁻¹.

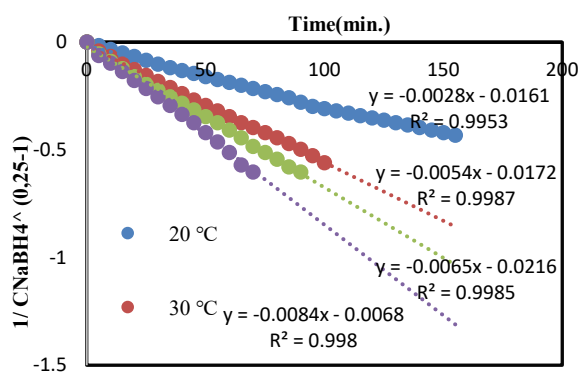


Figure 7. The linear regression based on n^{th} -order at 20 °C-50 °C

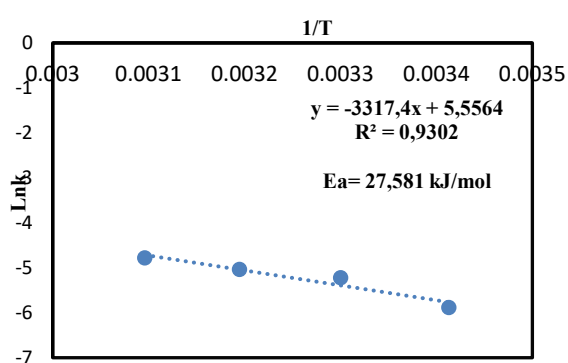


Figure 8. Arrhenius equation according to n^{th} -order reaction

3.3. Reusability of Ceria Supported Ni Complex Catalyst

The stability of the ceria supported Ni complex catalyst was tried in the hydrolysis of NaBH₄ by using in five times. Before reuse the catalyst washed with distilled water to take out the dirtiness on the catalyst. Ceria supported Ni complex exhibited excellent catalytic activity by providing 98 % efficiency even in the 5th cycle as shown in Figure 9.

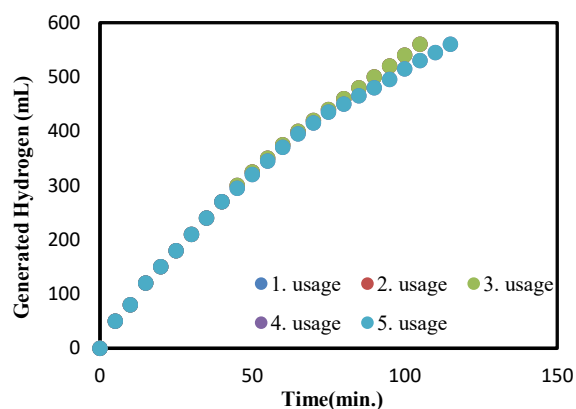


Figure 9. The reusability of ceria supported Ni complex catalyst by using five times in the hydrolysis of NaBH₄

The experimental results indicate that the ceria supported Ni complex catalyst is highly stable in hydrolysis of NaBH₄.

3.7. Characterization of ceria supported ni complex

3.7.1. FT-IR Spectrum

The FT-IR measurement was performed to investigate with compare the ceria supported Ni complex and Ni complex [1]. In Table 1 the band that occurred at 2896 cm⁻¹ are due to the free -OH groups or intramolecular OH...N which seen both ceria supported Ni complex and Ni complex. Both ceria supported Ni complex and Ni complex the band that occurred at 2745-2976 cm⁻¹ was corresponding to methyl group. At 1602-1619 cm⁻¹ band for Ni complex, for azomethine (C=N) group was changed as 1607-1623 cm⁻¹ in ceria supported Ni complex. For phenolic -C=O- the bands were occurred at 1692-1733 cm⁻¹ and 1689-1748 cm⁻¹ as ceria supported Ni complex and pure Ni complex respectively.

5 % Ni complex containing ceria supported Ni complex catalyst has the stronger bands in 512 cm⁻¹ that verified the formation of complex on the oxygen atom to metal atom (M-O) and at 421 cm⁻¹ corresponded to vibrations of nitrogen atom and metal atom (M-N), and the same bands are present on pure Ni complex.

Table 1. The results of FT-IR spectrum for Ceria supported Ni complex

Complex	cm ⁻¹					
	$\bar{\nu}$ -O-H (intramolecular)	δ -CH ₃	$\bar{\nu}$ -C=N-	$\bar{\nu}$ -C=O-	$\bar{\nu}$ -M-N	$\bar{\nu}$ -M-O
Ni complex	2896	2745 - 2976	1602 - 1619	1689 - 1748	421	512
Ceria supported Ni complex	2896	2753 - 2977	1607 - 1623	1692 - 1733	421	512

3.7.2. X-Ray Diffractograms (XRD)

In Figure 10, the XRD patterns of ceria supported-Ni complex were displayed.

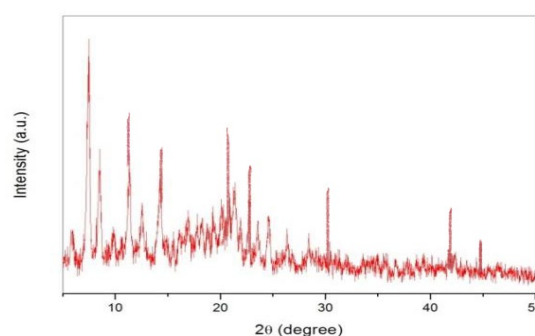


Figure 10. XRD results of Ceria supported Ni complex

It was understood that the catalyst has a completely crystal structure. For ceria supported-Ni complex, the major diffraction peaks were observed at 8.62; 9.69; 12.77; 14.92; 20.86; 23.41; 30.79; 43.06 and 44.91 respectively.

3.7.3. Brunauer-Emmett-Teller surface area analysis (BET)

Ceria supported Ni complex has a big surface area and that provide to increase the catalytic activity. For pure Ni (II) complex the surface area was recorded as 33.284 m^2g^{-1} and for ceria supported Ni complex, it was 64.377 m^2g^{-1} as indicated in Table 2. For ceria supported Ni complex the pore volumes increased almost more than 2 times than pure Ni complex.

Table 2. BET analysis results of catalyst

Catalyst	Average Pore Ratio (nm)	Pore Volume (cm^3g^{-1})	S BET (m^2g^{-1})
Ni Complex	10.569	0.132	33.284
Ceria supported Ni Complex	14.245	0.235	64.377

3.7.4. Scanning electron microscopy analysis (SEM)

For ceria supported Ni complex the SEM images were displayed in Figure 11. It was clearly seen that ceria supported Ni complex catalyst display completely homogeneous structure. According to SEM results the surface of ceria supported Ni complex catalyst was fully coated by Ni complex as shown in Figure 11.

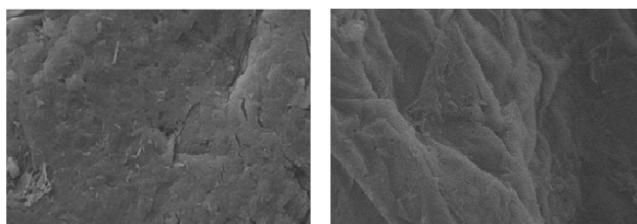


Figure 11. SEM images of Ceria supported Ni complex

generation. ceria supported Ni complex catalyst catalysts was characterized with using the SEM, BET, XRD and FTIR. The highest hydrogen generation rate was 16535.40 $\text{mL H}_2 \text{g}_{\text{cat}}^{-1}\text{min}^{-1}$ and 23320.00 $\text{mL H}_2 \text{g}_{\text{cat}}^{-1}\text{min}^{-1}$ at 30 °C and 50 °C respectively by using 0.01 g ceria supported-Ni complex catalyst. In summary, ceria supported Ni complex catalyst exhibited greater activity

in hydrogen generation. The activation energy (E_a) was recorded as 27.581 kJ/mol. The reusability tests showed the catalyst retained 98 % of its activities after fifth cycles. The hydrogen generation performance the comparison of ceria supported Ni complex and various Ni based catalysts in NaBH_4 hydrolysis reaction is shown in Table 3. Consequently, the prepared ceria supported Ni complex catalyst can be used as highly active, practical and low-cost materials for hydrogen generation in sodium borohydride hydrolysis.

Table 3. The hydrogen generation performance comparison of ceria supported Ni complex catalyst and various Ni catalysts in NaBH_4 hydrolysis reaction

Catalyst	Hydrogen Generation Rate ($\text{mL H}_2 \text{g}_{\text{cat}}^{-1}\text{min}^{-1}$)	References
Ceria / Ni-complex	16535.40	In This Study
Ni-Co/r-GO	1280.00	34
CoB/Ni-foam	1930.00	35
Co-Ni-Mo-P/g-Al ₂ O ₃	10125.00	36
Ni(II)-complex	2240.00	37
NiCo ₂ O ₄	1000.00	38

4. CONCLUSIONS

In present study, ceria supported Ni complex was prepared for NaBH_4 hydrolysis reaction to hydrogen generation. ceria supported Ni complex catalyst catalysts was characterized with using the SEM, BET, XRD and FTIR. The highest hydrogen generation rate was 16535.40 $\text{mL H}_2 \text{g}_{\text{cat}}^{-1}\text{min}^{-1}$ and 23320.00 $\text{mL H}_2 \text{g}_{\text{cat}}^{-1}\text{min}^{-1}$ at 30 °C and 50 °C respectively by using 0.01 g ceria supported-Ni complex catalyst. In summary, ceria supported Ni complex catalyst exhibited greater activity in hydrogen generation. The activation energy (E_a) was recorded as 27.581 kJ/mol. The reusability tests showed the catalyst retained 98 % of its activities after fifth cycles. The hydrogen generation performance the comparison of ceria supported Ni complex and various Ni based catalysts in NaBH_4 hydrolysis reaction is shown in Table 3. Consequently, the prepared ceria supported Ni complex catalyst can be used as highly active, practical and low-cost materials for hydrogen generation in sodium borohydride hydrolysis.

Conflict of interests

Authors declare that there is no a conflict of interest with any person, institute, company, etc.

REFERENCES

- Dillon, A.C.; Jones, K.M.; Bekkedahl, T.A.; Kiang, C.H.; Bethune, D.S.; Heben, M.J. *Nature*. **1997**, 386, 377–379.
- Sahiner, N, Sengel, SB. *Fuel Process Technol.* **2017**, 158, 1-8.
- Kaufman, C.M.; Sen, B. *J. Chem. Soc. Dalton Trans.* **1985**, 307–313.
- Schlapbach, L.; Züttel, A. *Nature*. **2001**, 414, 353-8.
- Sahiner, N.; Yasar, A.O.; Aktas, N. *J. Ind. Eng. Chem.* **2015**, 23, 100-8.
- Kojima, Y.; Kawai, Y.; Nakanishi, H.; Matsumoto, S. *J. Power Sources*. **2004**, 135, 36-41.
- Kilinc, D.; Saka, C.; Sahin, O. *J. Power Sources*. **2012**, 217, 256-261.
- Ceyhan, A.A.; Edebalı, S.; Fangaj, E. *Int. J. Hydrogen Energ.* **2020**, 45, 34761-34772.
- İzgi, MS.; Baytar, O.; Şahin, O.; Horoz, S. *Dig. J. Nanomater. Bios.* **2019**, 14, 1005-1012.
- Kilinc, D.; Sahin O.; *Int. J. Hydrogen Energ.* **2018**, 43, 10717-10727.
- Kilinc, D. *Energ Sources Part A.* **2018**, 40, 873-885.
- Iwasa, N.; Masuda, S.; Ogawa, N.; Takezawa, N. *Appl. Catal. A-Gen.* **1995**, 125, 145–157.
- Iwasa, N.; Mayanagi, T.; Nomura, W.; Arai, M.; Takezawa, N. *Appl. Catal. A-Gen.* **2003**, 248,153–160.
- Glisenti, A.; Galenda, A.; Natile, M.M. *Appl. Catal. A- Gen.* **2013**, 453, 102–112.
- Krajci, M.; Tsai, A.P.; Hafner, J. *J. Catal.* **2015**, 330, 6–18.
- Hernández, R.P.; Martínez, A.G. ; Mayoral, A.; Deepak, F.L.; García, M.E.F.; Galicia, G.M.; Miki, M.; Yacamán, M. *J. Adv. Mater. Res.* **2010**, 132, 205–219.
- Friedrich, M.; Teschner, D.; Gericke, A.K.; Armbrüster, M. *J. Phys. Chem. C.* **2012**, 116, 14930–14935.
- Hannauer, J; Demirci, UB; Pastor, G; et al. *Energ. Environ. Sci.* **2010**, 3, 1796.
- Larichev, YV; Netskina, OV; Komova, OV; et al. *Int. J. Hydrogen Energ.* **2010**, 35, 6501-7.
- Kilinc D.; Sahin O.; *Int. J. Hydrogen Energ.* **2019**, 44, 18858-18865.
- Xu, D; Zhao, L; Dai, P; et al. *J. Nat. Gas Chem.* **2012**, 21, 488-94.
- Wu C; Williams PT. *Appl. Catal. B-Environ.* **2009**, 87, 152-61.
- Kilinc, D.; Sahin, O.; *Int. J. Hydrogen Energ.* **2019**, 44, 28391-28401.
- Crisafulli, C.; Scir, S; Salanitri, M; et al. *Int. J. Hydrogen Energ.* **2011**, 36, 3817-26.
- Tian, H; Guo, Q; Xu D. *J. Power Sources.* **2010**, 195, 2136-42.
- Yan, K; Li, Y; Zhang, X; et al. *Int. J. Hydrogen Energ.* **2015**, 40, 16137-16146.
- Kilinc, D. *J. Baun Inst. Sci. Technol.* **2018**, 20, 296-310.
- Greluk, M.; Rotko, M.; Surdacka, ST. *Renew. Energ.* **2020**,155, 378-395.
- Crisafulli, C; Scire, S; Zito, R; et al. *Catal. Lett.* **2012**, 142, 882-8.
- Levalley, T.L.; Richard, A.R.; Fan, M. *Int. J. Hydrogen Energ.* **2014**, 39, 16983–17000.
- Ciambelli, P.; Palma, V.; Ruggiero, A. *Appl. Catal. B-Environ.* **2010**, 96, 18–27.
- Piedras, A.C.; Zamora, R. M.R.; Vázquez, B.C.A.; Martínez, A.G.; Galicia, G.M.; Anzures, F.M.; Hernández, R.P. *Catal. Today.* **2020**, Article in Press.
- Sahin, O.; Kilinc, D.; Saka, C. *J. Energy Institut.* **2016**, 89, 617-626.
- Chou, C.C.; Hsieh, C.H.; Chen, B.H. *Energy.* **2015**, 50, 1973-1982.
- Guoa, S.; Wua, Q.; Sun, J.; Chen, T.; Feng, M.; Wang, Q.; Wang, Z.; Zhao, B.; Ding, D. *Int. J. Hydrogen Energ.* **2017**, 42, 21063-21072.
- Wang, L.; Li, Z.; Zhang, P.; Wang, G.; Xie G. *Int. J. Hydrogen Energ.* **2016**, 41, 1468-1476.
- Kilinc, D.; Sahin, O.; Saka, C. *Int. J. Hydrogen Energ.* **2017**, 42, 20625-20637.
- Jadhav, A.R.; Bandal, H.A.; Kim H. *Mater. Lett.* **2017**, 198, 50-53.



Silica-coated magnetic Fe₃O₄ nanoparticles as efficient nano-adsorbents for the improvement of the vapor-phase adsorption of benzene

Mehmet Şakir ECE^{1,*}, Sinan KUTLUAY², Ömer ŞAHİN²

¹Vocational High School of Health Services, Mardin Artuklu University, Mardin, 47100, Turkey

²Department of Chemical Engineering, Faculty of Engineering, Siirt University, Siirt, 56100, Turkey

Received: 21 June 2020; Revised: 13 April 2021; Accepted: 16 March 2021

*Corresponding author e-mail: sakirece@artuklu.edu.tr

Citation: Ece, M. Ş.; Kutluay, S.; Şahin, Ö. *Int. J. Chem. Technol.* 2021, 5 (1), 33-41.

ABSTRACT

This study focused on the preparation of silica-coated Fe₃O₄ (Fe₃O₄@SiO₂) for the improvement of the vapor-phase adsorption of benzene. The Fe₃O₄@SiO₂ was prepared via the co-precipitation method, while its characterization was carried out using FT-IR, SEM and BET surface area analyses. The experimental parameters were evaluated for the vapor-phase adsorption of benzene using response surface methodology (RSM). The Fe₃O₄@SiO₂ adsorbed 197.50 mg g⁻¹ of the vapor-phase benzene under the following optimum conditions: 39.93 min residence time, 13.57 mg l⁻¹ initial benzene concentration and 26.87°C temperature. The vapor-phase adsorption mechanism of benzene on the Fe₃O₄@SiO₂ was clarified by investigating the isotherms including Dubinin-Radushkevich (D-R), Freundlich and Langmuir, and the experimental data were well fitted to the D-R model. The vapor-phase adsorption kinetics of benzene on the Fe₃O₄@SiO₂ was clarified by investigating the kinetics such as pseudo first-order (PFO) model and pseudo second-order (PSO) model, and the experimental results obeyed the PSO model. This study demonstrated the application potential of magnetic Fe₃O₄@SiO₂ as promising low-cost nano-adsorbent.

Keywords: Fe₃O₄@SiO₂ magnetic nanoparticles, response surface methodology, vapor-phase adsorption of benzene.

Benzenin buhar-fazı adsorpsiyonunun iyileştirilmesi için etkili nano-adsorbentler olarak silika-kaplı manyetik Fe₃O₄ nanoparçacıkları

ÖZ

Bu çalışma, benzenin buhar-fazı adsorpsiyonunun iyileştirilmesi için silika-kaplı Fe₃O₄ (Fe₃O₄@SiO₂) hazırlanmasına odaklandı. Fe₃O₄@SiO₂ birlikte çökeltme yöntemi ile hazırlanırken karakterizasyonu FT-IR, SEM ve BET yüzey alanı analizleri kullanılarak gerçekleştirildi. Deneysel parametreler, yanıt yüzey metodolojisi (RSM) kullanılarak benzenin buhar-fazı adsorpsiyonu için değerlendirildi. Fe₃O₄@SiO₂, aşağıdaki optimum koşullar altında 197,50 mg g⁻¹ buhar-fazı benzeni adsorbe etti: 39,93 dakika kalma süresi, 13,57 mg l⁻¹ başlangıç benzen konsantrasyonu ve 26,87°C sıcaklık. Benzenin Fe₃O₄@SiO₂ üzerindeki buhar fazı adsorpsiyon mekanizması, Dubinin-Radushkevich (D-R), Freundlich ve Langmuir dahil izotermeler incelenerek netleştirildi ve deneysel veriler D-R modeline iyi bir şekilde uyduruldu. Benzenin Fe₃O₄@SiO₂ üzerindeki buhar-fazı adsorpsiyon kinetiği, sözde birinci-dereceden (SBD) model ve sözde ikinci dereceden (SİD) model gibi kinetikler incelenerek netleştirildi, ve deneysel sonuçlar SİD modele uydu. Bu çalışma, Fe₃O₄@SiO₂'nin umut verici düşük maliyetli nano-adsorbent olarak uygulama potansiyelini gösterdi.

Anahtar Kelimeler: Benzenin buhar-fazı adsorpsiyonu, Fe₃O₄@SiO₂ manyetik nanoparçacıklar, yanıt yüzey metodu.

1. INTRODUCTION

Benzene, one of the important volatile organic compounds (VOCs), is an important material in chemical processing industries. VOCs are important air pollutants

because of such detrimental effects as allergic reactions, nausea, throat irritation, nose, eye and headache. Besides, they cause dangerous environmental problems such as photochemical smog, suspended particulate matter, stratospheric ozone depletion and global warming.

Hence, VOCs with low concentrations have an important potential for environmental problem. This toxic product (benzene), which is extremely hazardous for human health and the environment, is emitted from automotive exhaust or fuels that evaporate from tanks, vehicle carburetors, and gas stations, particularly during oil refining operations, petrochemical production, and oil storage processes.¹⁻⁴ In general, the quality and amount of air pollutant emissions from the exhaust pipes are closely related to the fuel composition. Emissions from consumer products, building materials, paints, and adhesives are also influential in this situation. Besides, tobacco smoke is a source of this pollutant.⁵ Industrial sectors considerably disrupt the gas rates in the air. The adverse effects on air quality create unfavorable conditions in terms of health. It is a necessity to decrease the entry of poisonous gases into the environmental atmosphere and to develop reduction strategies. To this end, pollutant removal methods have become essential. In this regard, nanotechnology presents effective solutions compared to traditional ones in adsorption technology as in all other fields.⁶⁻⁷ In adsorption technology, magnetic nanomaterials with unique properties such as paramagnetism or ferromagnetism have drawn much attention. Magnetite (Fe_3O_4) is a common material widely examined in nanotechnological research.⁸ It attracted considerable attention because of its magnetic properties such as biocompatibility, low-toxicity, low cost and high surface area.⁹ Functionalization of Fe_3O_4 nanoparticles with functional groups both reduces agglomeration and provides new active sites for adsorption.¹⁰⁻¹¹ Fe_3O_4 , which is one of many magnetic materials, facilitates recovery in the separation steps due to its magnetic feature. The pore volume of Fe_3O_4 nanoparticles has a well-developed pore structure producing a large number of active sites. Pore volume declines in the active areas due to agglomeration. Coating with organic or inorganic surfactants is a method to prevent particle agglomeration.¹² Silica (SiO_2) has extraordinary physical and chemical properties as an inorganic surfactant.¹⁰

This study focused on the preparation of silica-coated Fe_3O_4 ($\text{Fe}_3\text{O}_4@\text{SiO}_2$) magnetic nanoparticles and their application for the improvement of the vapor-phase adsorption of benzene. The $\text{Fe}_3\text{O}_4@\text{SiO}_2$ was prepared via the co-precipitation method, while its characterization was carried out using FT-IR, SEM and BET surface area analyses. Experimental parameters were evaluated for the vapor-phase adsorption of benzene by using the Box-Behnken design (BBD) with the response surface method (RSM). The vapor-phase adsorption mechanism of benzene on the $\text{Fe}_3\text{O}_4@\text{SiO}_2$ was clarified by investigating the isotherms including Dubinin-Radushkevich (D-R), Freundlich and Langmuir. The vapor-phase adsorption kinetics of benzene on the $\text{Fe}_3\text{O}_4@\text{SiO}_2$ was clarified by investigating the kinetics

such as pseudo first-order (PFO) model and pseudo second-order (PSO) model.

2. MATERIALS AND METHODS

2.1. Materials

The tetraethyl orthosilicate (TEOS, $\text{Si}(\text{OC}_2\text{H}_5)_4$), benzene (C_6H_6), iron (II) chloride tetrahydrate ($\text{FeCl}_2 \cdot 4\text{H}_2\text{O}$), ethanol ($\text{CH}_3\text{CH}_2\text{OH}$), iron (III) chloride hexahydrate ($\text{FeCl}_3 \cdot 6\text{H}_2\text{O}$), and ammonia (NH_3) were purchased from MERCK, ALFA AESAR, SIGMA-ALDRICH, MERCK, SIGMA-ALDRICH and VWR Chemical Companies, respectively. All solvents and chemicals employed in the study have analytical purity.

2.2. Preparation of the $\text{Fe}_3\text{O}_4@\text{SiO}_2$ magnetic nanoparticles

Fe_3O_4 was prepared by co-precipitation of Fe (III) and Fe (II). The mixture of $\text{FeCl}_2 \cdot 4\text{H}_2\text{O}$ and $\text{FeCl}_3 \cdot 6\text{H}_2\text{O}$ salts, in which the ratio of $\text{Fe}^{+2}/\text{Fe}^{+3}$ was stoichiometrically 1/2, was mixed for 30 min at 80°C under argon gas in 50 ml deionized water. The color of the homogenized solution immediately became orange. 10 ml NH_3 solution was added drop-by-drop to obtain the co-precipitation. The color of the bulk solution instantly changed from orange to black. Amalgamation was continued under argon for 30 min. The Fe_3O_4 obtained as a product was washed five times with ethanol and deionized water. Fe_3O_4 was dried in a vacuum oven at 60°C for 24 h. 0.5 g of Fe_3O_4 was dispersed in a flask in 20 ml of deionized water, 5 ml of ammonia and 100 ml of ethanol. The solution of mixture was homogenized by ultrasonication for 30 min to create an uniform distribution. Then 0.4 ml of TEOS was added drop-by-drop to the solution under a strong mixture. The amalgamation was continued under argon gas for 12 h at room temperature. The $\text{Fe}_3\text{O}_4@\text{SiO}_2$, obtained as a product, was separated by a magnet, washed five times with deionized water and ethanol. The $\text{Fe}_3\text{O}_4@\text{SiO}_2$ was dried in a vacuum oven at 60°C for 24 h.¹³ Schematic representation of the preparation of the $\text{Fe}_3\text{O}_4@\text{SiO}_2$ was presented in Figure 1.

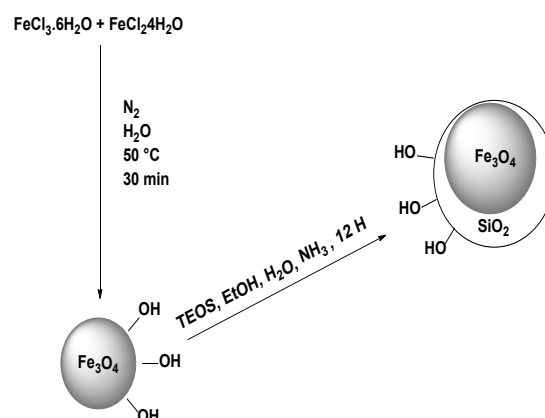


Figure 1. Schematic representation of the preparation of the Fe₃O₄@SiO₂ magnetic nanoparticles

2.3. Removal of benzene vapor by adsorption process

The adsorption process practiced in the removal of benzene vapor by using Fe₃O₄@SiO₂ magnetic nanoparticles was defined with the previously published study.¹⁴ The nitrogen (N₂) flow rate for the removal of benzene vapor was chosen as 100 ml min⁻¹. The optimum dosage of Fe₃O₄@SiO₂ employed for the removal of benzene vapor was 0.09 g. The adsorption capacity, q (mg g⁻¹) for benzene vapor was defined with Eq. (1):¹⁵

$$q = \frac{F}{m} \int_0^t (C_{in} - C_{eff}) dt \quad (1)$$

Here m is the optimum dosage of Fe₃O₄@SiO₂ (g), F is the flow rate (l min⁻¹), C_{in} and C_{eff} are the initial and output benzene vapor concentrations (mg l⁻¹), respectively, and t is the residence time (min).

2.4. Characterization

Fourier Transform Infrared Spectroscopy (FT-IR) spectra were taken using a Bruker-Vertex 70v FT-IR spectrometer. Scanning Electron Microscopy (SEM) images were taken by a ZEISS-EVO 50 instrument. Brunauer–Emmett–Teller (BET) surface area was determined by means of a Quantachrome-Nova instrument. Mathematical modeling for experimental

data were conducted by applying Design Expert 12.0.8.0 Software (Free Trial Version).

3. RESULTS AND DISCUSSION

3.1. Characterization of the Fe₃O₄@SiO₂ magnetic nanoparticles

Characterization of the Fe₃O₄@SiO₂ magnetic nanoparticles was conducted based on SEM, FTIR, and BET surface area. SEM images, FTIR spectra and N₂ gas adsorption/desorption isotherms of these nanoparticles were presented in Figure 2, Figure 3, and Figure 4, respectively.

3.1.1. SEM analysis

SEM analysis was used to observe the surface morphology of the Fe₃O₄ and Fe₃O₄@SiO₂ magnetic nanoparticles. Figure 2 presented SEM microphotographs (scale length = 500 nm) of Fe₃O₄ and Fe₃O₄@SiO₂. It was understood that Fe₃O₄, which had good dispersion, had a rough surface. It was observed that the pore structure was rough and spongy. Pores and voids were clearly noticeable on the surface of Fe₃O₄@SiO₂. It was understood that the intrusions, protrusions, and roughness increased the surface area in the microstructure of the Fe₃O₄@SiO₂. Considering the scale length, it is understood that the diameters of the magnetic nanoparticle spheres are approximately 70-110 nm.¹⁶

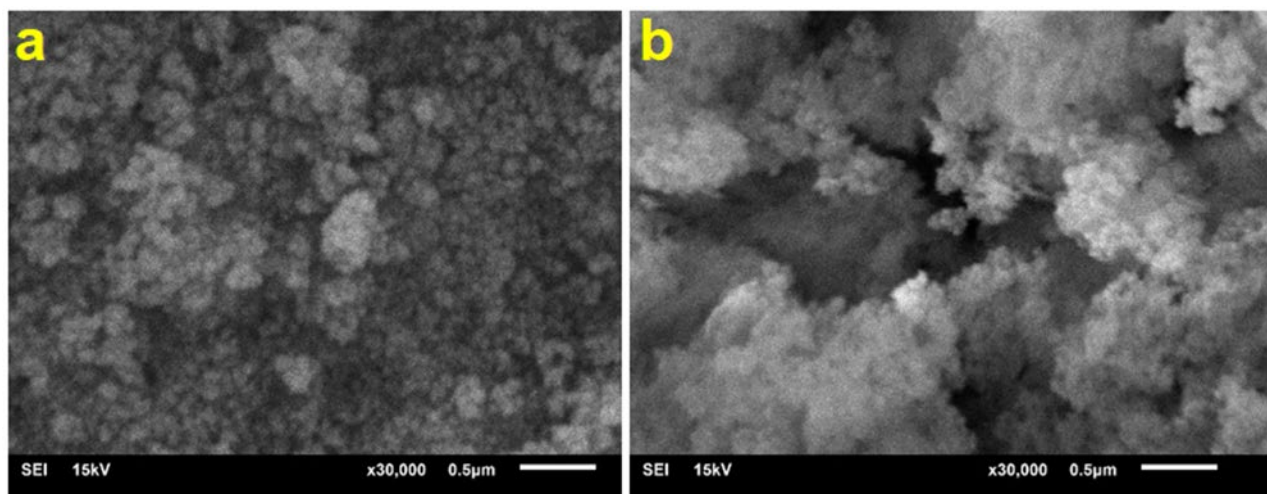


Figure 2. SEM images of the Fe₃O₄ (a) and Fe₃O₄@SiO₂ (b) magnetic nanoparticles.

3.1.2. FTIR analysis

FTIR spectra of Fe₃O₄ and Fe₃O₄@SiO₂ magnetic nanoparticles were presented in Figure 3. The characteristic absorption peak at 552 cm⁻¹ observed in the FTIR spectrum of Fe₃O₄ belonged to the Fe-O bond, which verified the presence of Fe₃O₄. The peaks observed around 3446 cm⁻¹, 1654 cm⁻¹ and 1480 cm⁻¹ were peaks of stretching, bending, and deforming vibrations of the

adsorbed water (-OH). The new peaks at 570 cm⁻¹ and 964 cm⁻¹ observed in the FTIR spectrum of the Fe₃O₄@SiO₂ were the peaks of the bending vibration of the Si-O bond and the stretching vibration of the Si-OH bond, respectively. The peak at 1082 cm⁻¹ belonged to the asymmetric stretching vibration of the Si-O-Si bond. This peak indicated that the surface of Fe₃O₄ was successfully coated with SiO₂. The FTIR spectra observed for Fe₃O₄ and Fe₃O₄@SiO₂ complied with the literature.¹⁷

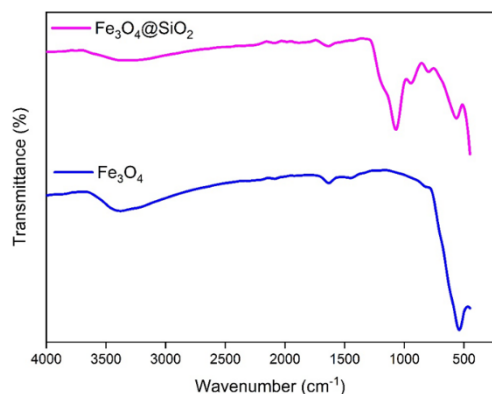


Figure 3. FT-IR spectrum of the Fe_3O_4 and $\text{Fe}_3\text{O}_4@\text{SiO}_2$ magnetic nanoparticles

3.1.3. BET analysis

The adsorption and desorption isotherms of $\text{Fe}_3\text{O}_4@\text{SiO}_2$ magnetic nanoparticles with BET surface area of $28.97 \text{ m}^2 \text{ g}^{-1}$ were presented in Figure 4. When Figure 4 was analyzed, it was understood that $\text{Fe}_3\text{O}_4@\text{SiO}_2$ fitted the H3 type hysteresis cycle and IV type curve according to the IUPAC classification criteria. It was also estimated that there were homogeneous mesoporous layers. The low surface area of $\text{Fe}_3\text{O}_4@\text{SiO}_2$ indicated that the surface area was affected by the SiO_2 modification. It was because SiO_2 was a shell of magnetic nanoparticles, and SiO_2 infiltrated into the spaces on the surface.

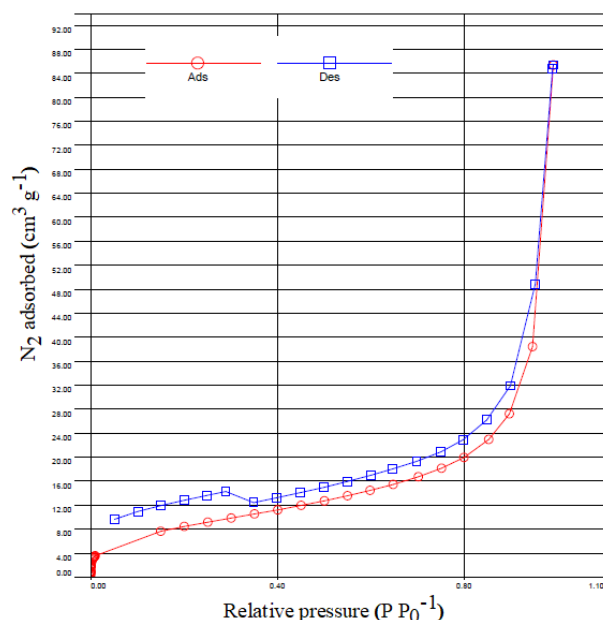


Figure 4. N_2 adsorption and desorption isotherms of the $\text{Fe}_3\text{O}_4@\text{SiO}_2$ magnetic nanoparticles

3.2. Experimental design and optimization

In the present study, RSM, which is an experimental method for the development, improvement, and optimization of the design process, was applied to

determine the importance of the potential interactions of the functioning parameters. The approach of RSM-based BBD was employed to perform statistical analyses and obtain the regression model. In the vapor-phase adsorption of benzene, all statistical analyzes for modeling and optimization of experimental studies were evaluated. Effective parameters and interactions were evaluated by the program through variance analysis (ANOVA) and three-dimensional graphics. The general quadratic model equation was obtained with ANOVA test and BBD approach to analyze the relationship between the obtained results and parameters. The predicted adsorption capacity values were defined depending on the parameter values selected by employing the obtained quadratic model equation. The significance of the model predicted by the program was evaluated with the R^2 obtained, and the p-value, adeq precision and F-value results achieved by the program were analyzed. In the study, a three-variable BBD was used to determine the effect of different parameters upon response. The residence time, initial benzene concentration, and temperature were chosen as the essential independent parameters affecting the vapor-phase adsorption. The adsorption capacity of the vapor-phase benzene was considered as the response. The parameters analyzed in the BBD were displayed in three coded values. Experimental design levels with independent factors and the results obtained by the BBD approach were presented in Table 1 and Table 2 respectively. The compatibility of the results was presented with ANOVA analysis in Table 3. According to ANOVA results, the p-value of the proposed model was calculated as 0.0001, which shows that 99.99% of the results obtained in the laboratory conditions of the experiments predicted by the program can be defined with the model obtained with the program. Besides, the high R^2 value, F-value (>4), and adeq precision (>4) results, which were determined as 99.89, 678.81 and 80.50% respectively, showed that the experimental data well defined with the predicted model.¹⁸⁻¹⁹ Besides, the fact that the actual and predicted adsorption capacities presented in Table 2 were close to each other indicated the suitability of the predicted model.

Table 1. Experimental design levels with independent factors

Factors	Coded values		
	-1	0	+1
Residencetime (X_1) (min)	20	30	40
Concentration (X_2) (mg l^{-1})	10	12.5	15
Temperature (X_3) ($^{\circ}\text{C}$)	25	30	35

Figure 5 presented three-dimensional (3D) plots achieved with the program, showing the influence of initial benzene concentration, adsorption temperature and residence time on the vapor-phase adsorption capacity of benzene. It could be observed in Figure 5a that the vapor-phase adsorption capacity of benzene increased with the increase in residence time.

Table 2. Experiment design results obtained for the vapor-phase adsorption of benzene by the Fe₃O₄@SiO₂ magnetic nanoparticles.

Run	Time (min)	Concentration (mg l ⁻¹)	Temperature (°C)	Actual adsorption capacity (mg g ⁻¹)	Predicted adsorption capacity (mg g ⁻¹)
1	30	12.5	30	80	83
2	20	15	30	50	57
3	20	10	30	41	40
4	30	15	35	60	58
5	40	12.5	35	150	162
6	30	12.5	30	80	86
7	20	12.5	25	45	53
8	40	15	30	185	190
9	40	10	30	160	157
10	30	12.5	30	82	85
11	30	15	25	110	116
12	40	12.5	25	198	201
13	30	10	25	70	68
14	30	12.5	30	80	89
15	30	10	35	55	57
16	20	12.5	35	36	28
17	30	12.5	30	80	85

Table 3. ANOVA results created in accordance with the BBD approach

Source	Sum of squares	df	F-value	p-value	
Model (quadratic)	20627.11	9	678.81	< 0.0001	Significant
X ₁	8532.50	1	5005.50	< 0.0001	
X ₂	8247.96	1	115.09	< 0.0001	
X ₃	191.84	1	274.47	< 0.0001	
X ₁ X ₂	1545.57	1	9.44	0.0180	
X ₁ X ₃	0.0071	1	56.10	0.0001	
X ₂ X ₃	3.64	1	45.18	0.0003	
X ₁ ²	1242.51	1	598.85	< 0.0001	
X ₂ ²	1181.88	1	3.73	0.0948	
X ₃ ²	472.13	1	10.96	0.0129	

R² = 0.9989, Adeq precision = 80.50

The adsorption process reached equilibrium after a specific residence time because of the limited number of active areas on the surface of Fe₃O₄@SiO₂.²⁰ As observed in Figure 5b, the temperature had an adverse effect on vapor-phase adsorption. Adsorption capacity decreased as the temperature rose. Also, it could be said that the decrease in the amount adsorbed with the increased temperature might be caused by the destruction of the active bond sites on the adsorbent.²¹ When the surface plot for the initial benzene concentration versus temperature in Figure 5c was considered, it was evident that the initial benzene concentration did not have a meaningful effect on the vapor-phase adsorption capacity. The increase seen in the vapor-phase adsorption

of benzene was caused by the less interest in Fe₃O₄@SiO₂. Similar behaviors have been observed in previous studies.^{14, 22}

Process parameters were optimized to define the vapor-phase adsorption capacity of benzene by applying Fe₃O₄@SiO₂. Based on the model equation for the actual values predicted by the quadratic model, the mathematically optimum conditions were defined. With the help of the predicted model equation, optimum values were determined to be 39.93 min for residence time, 13.57 mg l⁻¹ for initial benzene concentration, and 26.87°C for temperature. The vapor-phase adsorption capacity of benzene with Fe₃O₄@SiO₂ was determined as 197.50 mg g⁻¹.

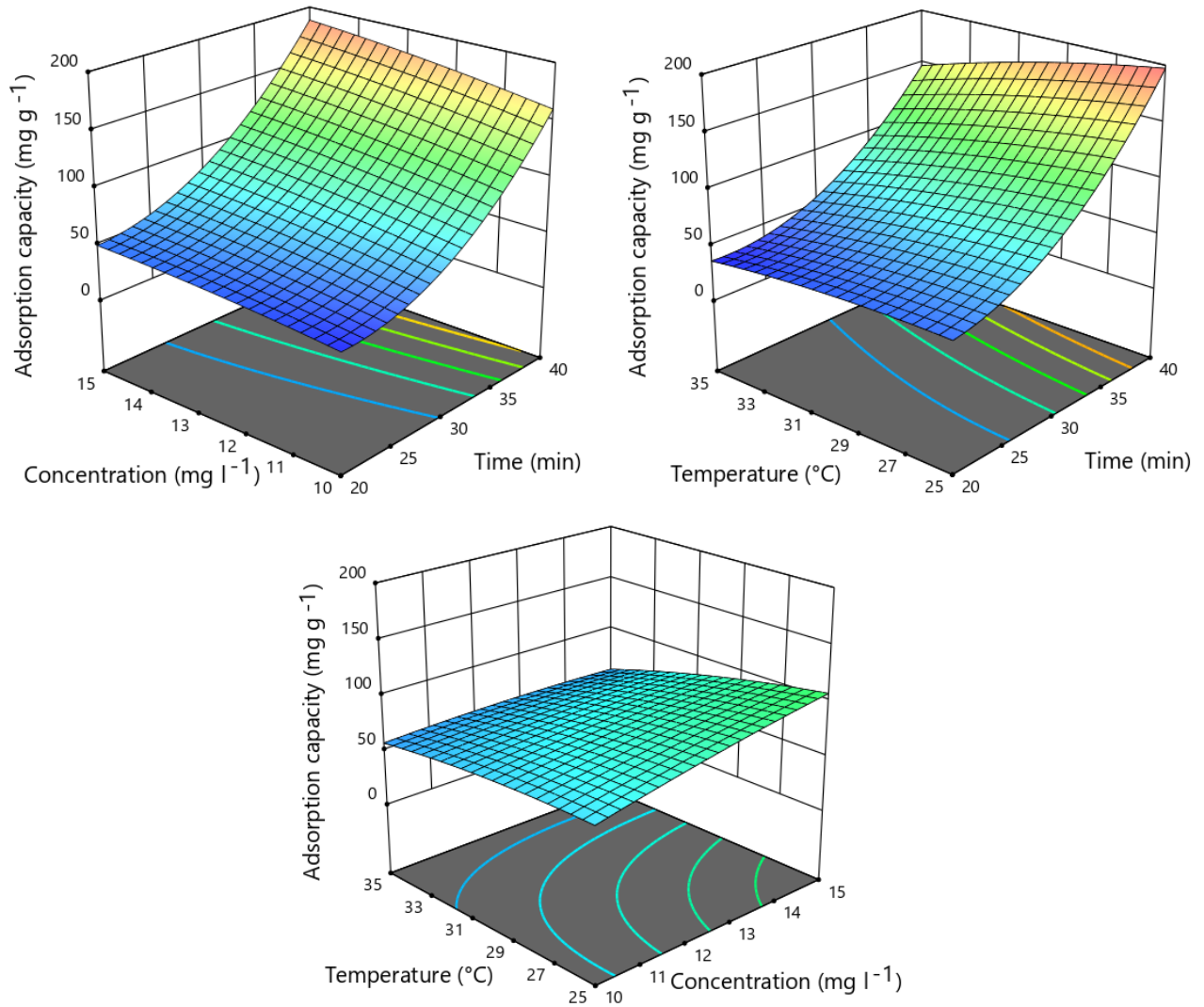


Figure 5. The influence of parameters on the vapor-phase adsorption capacity of benzene.

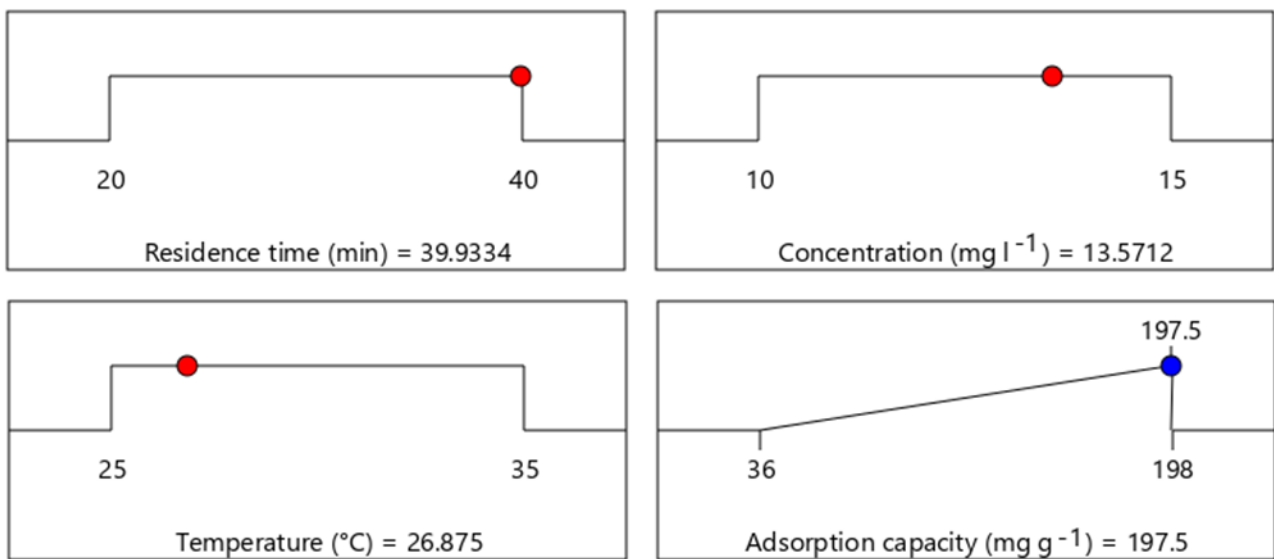


Figure 6. Optimum values for the vapor-phase adsorption of benzene

3.3. Kinetic studies

Under optimum conditions defined by RSM, the vapor-phase adsorption kinetics of benzene on the $\text{Fe}_3\text{O}_4@\text{SiO}_2$ was clarified by investigating the kinetics such as pseudo first-order (PFO) model and pseudo second-order (PSO) model. PFO model defines the adsorption rate proportional to the number of empty sites.²³ PFO model was related to the change of concentration over time. The non-linear form of the PFO model kinetic equation was presented in Eq. (2). The PSO model equation, based on the capacity of the adsorption equilibrium, suggests that the rate of adsorption is related to the concentration of active sites on the surface of the adsorbent.²³ The non-linear form of the PSO model was given with the Eq. (3).²⁴

$$q_t = q_e(1 - e^{-k_f t}) \quad (2)$$

$$q_t = \frac{k_s q_e^2 t}{1 + k_s q_e t} \quad (3)$$

Where, q_e and q_t indicate the adsorption capacity at equilibrium and t time (mg g^{-1}), respectively, and k_f represents the PFO model rate constant (min^{-1}), k_s is the PSO model rate constant ($\text{g mg}^{-1} \text{min}^{-1}$).

In the vapor-phase adsorption process of benzene by the $\text{Fe}_3\text{O}_4@\text{SiO}_2$, the experimental results obeyed the PSO model (Figure 7 and Table 4).

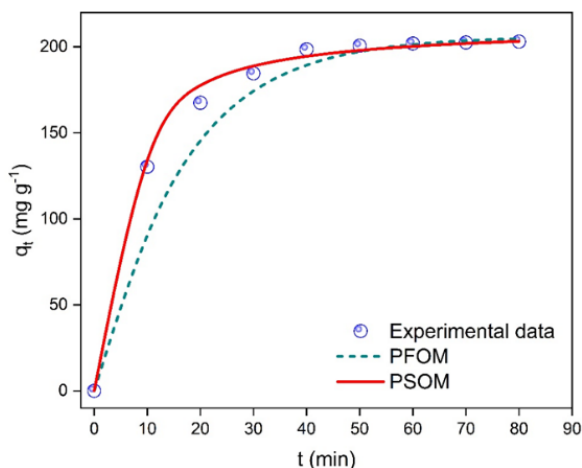


Figure 7. Adsorption kinetic models of benzene by the $\text{Fe}_3\text{O}_4@\text{SiO}_2$ magnetic nanoparticles

Table 4. Adsorption kinetic parameters of benzene by the $\text{Fe}_3\text{O}_4@\text{SiO}_2$ magnetic nanoparticles

Kinetic models	Parameters	Values
PFO model	q_e	205.952
	k_f	0.0648
	R^2	0.967
PSO model	q_e	212.45
	k_s	0.0013
	R^2	0.990

3.4. Isotherm studies

Under optimum conditions defined by RSM, The vapor-phase adsorption mechanism of benzene on the $\text{Fe}_3\text{O}_4@\text{SiO}_2$ was clarified by investigating the isotherms including Dubinin-Radushkevich (D-R), Freundlich and Langmuir. The Langmuir adsorption isotherm applies to single-layer surface adsorption, including a limited number of identical regions. The model assumes that the adsorption energies on the surface are the same and that there is no adsorbate migration at the surface plane. Based on these assumptions, the Langmuir model is formulated in Eq. (4). The Freundlich isotherm theory puts forward that the ratio of the amount of solute adsorbed on a particular sorbent mass to the concentration of the solute is not constant at different concentrations. The non-linear form of the Freundlich isotherm model was given in Eq. (5).²⁵ The D-R isotherm model was developed to describe the effect of the porous structure of adsorbents. It is based on the theory of the adsorption potential and suggests that in contrast to the layered adsorption on pore walls, the adsorption process is associated with the filling of the microporous volume.²⁶⁻²⁷ The non-linear form of this model was presented in Eq. (6).²⁸ In Eq. (6), β gives E which represents the average free energy of adsorption per particle. E was presented in Eq. (8).²⁸

$$q_e = \frac{q_{max} K_L C_e}{1 + K_L C_e} \quad (4)$$

$$q_e = K_F C_e^{\frac{1}{n}} \quad (5)$$

$$q_e = q_m \exp(-\beta \varepsilon^2) \quad (6)$$

$$\varepsilon = RT \ln \left(1 + \frac{1}{C_e} \right) \quad (7)$$

$$E = \frac{1}{\sqrt{2\beta}} \quad (8)$$

Where, C_e (mg l^{-1}) is the equilibrium concentration of the adsorbate, q_e (mg g^{-1}) is the adsorption capacity at equilibrium, q_{max} (mg g^{-1}) is the maximum monolayer adsorption capacity, K_L (l mg^{-1}) is Langmuir isotherm constant, K_F [$(\text{mg g}^{-1}) (\text{l mg}^{-1})^{1/n}$] is the Freundlich isotherm constant, n is the adsorption density, if n is between 1 and 10, this situation indicates a suitable adsorption process, q_m is the maximum adsorption capacity (mg g^{-1}), β is the activity coefficient constant ($\text{mol}^2 \text{kJ}^{-2}$), ε is the polanyi potential (J mol^{-1}), R and T represent the gas constant ($8.314 \text{ J mol}^{-1} \text{ K}^{-1}$), absolute temperature (K), respectively, If $E < 8 \text{ kJ mol}^{-1}$, physical adsorption is dominant. However, in the situation indicating $8 \text{ kJ mol}^{-1} < E < 16 \text{ kJ/mol}$ and $E > 16 \text{ kJ mol}^{-1}$, adsorption occurs by ion exchange and diffusion, respectively.²⁹

In the study, the estimated q_{max} from the Langmuir model was $237.192 \text{ mg g}^{-1}$, K_L was 0.281 l mg^{-1} . The R^2 value

was 0.999, indicating the equilibrium isotherm data of benzene in the vapor-phase adsorption process by the $\text{Fe}_3\text{O}_4@\text{SiO}_2$ better fitted to the D-R model. The calculated E value in the study was determined as $0.463 \text{ kJ mol}^{-1}$, indicating that the vapor-phase adsorption process of benzene was physical (Figure 8 and Table 5). In addition, the n value of Freundlich model was calculated as 3.472, indicating that the vapor-phase adsorption process of benzene was suitable.³⁰

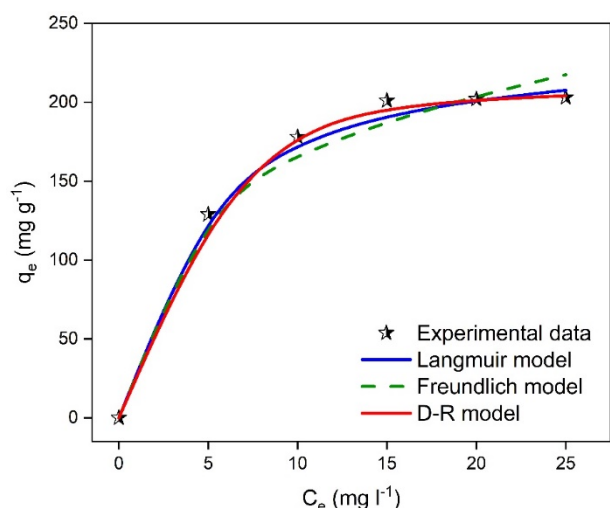


Figure 8. Adsorption isotherm models of benzene by the $\text{Fe}_3\text{O}_4@\text{SiO}_2$ magnetic nanoparticles

Table 5. Adsorption isotherm parameters of benzene by the $\text{Fe}_3\text{O}_4@\text{SiO}_2$ magnetic nanoparticles

Isotherm models	Parameters	Values
Langmuir	q_{max}	237.192
	K_L	0.281
	R^2	0.997
	K_F	86.056
Freundlich	n	3.472
	R^2	0.991
	q_m	208.721
D-R	β	2.334×10^{-6}
	E	0.463
	R^2	0.999

4. CONCLUSIONS

The present study focused on the preparation of $\text{Fe}_3\text{O}_4@\text{SiO}_2$ for the improvement of the vapor-phase adsorption of benzene. The $\text{Fe}_3\text{O}_4@\text{SiO}_2$ was prepared via the co-precipitation method, while its characterization was carried out using FT-IR, SEM and BET surface area analyses. The experimental parameters were evaluated for the vapor-phase adsorption capacity of benzene using BBD under RSM. The $\text{Fe}_3\text{O}_4@\text{SiO}_2$ adsorbed 197.50 mg g^{-1} of the vapor-phase benzene under the following optimum conditions: 39.93 min residence time, 13.57 mg l^{-1} initial benzene concentration and 26.87°C temperature. The vapor-phase adsorption mechanism of benzene on the $\text{Fe}_3\text{O}_4@\text{SiO}_2$ was clarified by investigating the isotherm models such as Dubinin-Radushkevich (D-R), Freundlich and Langmuir, and the

experimental data were well fitted to the D-R model. The vapor-phase adsorption kinetics of benzene on the $\text{Fe}_3\text{O}_4@\text{SiO}_2$ was clarified by investigating the kinetics such as PFO model and PSO model, and the experimental results obeyed the PSO model. This study demonstrated the application potential of magnetic $\text{Fe}_3\text{O}_4@\text{SiO}_2$ as promising low-cost nano-adsorbents for the vapor-phase adsorption of benzene.

ACKNOWLEDGEMENTS

The authors are grateful to the Mardin Artuklu University Research Fund (MAUBAP, Project No. MAÜ.BAP.18.SHMYO.030) for their financial support.

Conflict of interests

I declare that there is no a conflict of interest with any person, institute, company, etc.

REFERENCES

- Ece, M. Ş.; Kutluay, S.; Şahin, Ö.; Horoz, S. *Ind. Eng. Chem. Res.* **2020**, *59* (48), 21106-21123.
- Kutluay, S. *Fuel* **2021**, *287*, 119691.
- Kutluay, S.; Temel, F. *Colloid Surf. A-Physicochem. Eng. Asp.* **2021**, *609*, 125848.
- Şahin, Ö.; Kutluay, S.; Horoz, S.; Ece, M. Ş. *Environ. Sci. Pollut. Res.* **2021**, *28* (5), 5231-5253.
- Wallace, L. A. *Environ. Health Perspect.* **1989**, *82*, 165-169.
- Yang, X.; Yi, H.; Tang, X.; Zhao, S.; Yang, Z.; Ma, Y.; Feng, T.; Cui, X. *J. Environ. Sci.* **2018**, *67*, 104-114.
- Wibowo, N.; Setyadhi, L.; Wibowo, D.; Setiawan, J.; Ismadji, S. *J. Hazard. Mater.* **2007**, *146* (1-2), 237-242.
- de las Nieves Piña, M.; Rodríguez, P.; Gutiérrez, M. S.; Quiñonero, D.; Morey, J.; Frontera, A. *Chem. Eur. J.* **2018**, *24* (49), 12820-12826.
- Connie, Z. Y.; Ariya, P. A. *J. Environ. Sci.* **2015**, *31*, 164-174.
- Roto, R.; Yusran, Y.; Kuncaka, A. *Appl. Surf. Sci.* **2016**, *377*, 30-36.
- Mohamed, E. F. *Environ. Dev. Sustain.* **2017**, *6* (2).
- Duan, S.; Xu, X.; Liu, X.; Wang, Y.; Hayat, T.; Alsaedi, A.; Meng, Y.; Li, J. *J. Colloid Interface Sci.* **2018**, *513*, 92-103.
- Zandipak, R.; Sobhan Ardakani, S.; Shirzadi, A. *Sep. Sci. Technol.* **2020**, *55* (3), 456-470.
- Kutluay, S.; Baytar, O.; Şahin, Ö. *J. Environ. Chem. Eng.* **2019**, *7* (2), 102947.
- Zhao, Z.; Wang, S.; Yang, Y.; Li, X.; Li, J.; Li, Z. *Chem. Eng. J.* **2015**, *259*, 79-89.

16. Yousefi, V.; Tarhriz, V.; Eyvazi, S.; Dilmaghani, A. *J. Nanobiotechnology* **2020**, *18* (1), 155.
17. Ma, C.; Li, C.; He, N.; Wang, F.; Ma, N.; Zhang, L.; Lu, Z.; Ali, Z.; Xi, Z.; Li, X. *J. Biomed. Nanotechnol.* **2012**, *8* (6), 1000-1005.
18. Kutluay, S.; Ece, M. Ş.; Şahin, Ö. *Int. J. Chem. Technol.* **2020**, *4* (2), 146-155.
19. Temel, F.; Kutluay, S. *New J. Chem.* **2020**, *44* (30), 12949-12961.
20. Vohra, M. S. *Arab. J. Sci. Eng.* **2015**, *40* (11), 3007-3017.
21. Padmavathy, V. *Bioresour. Technol.* **2008**, *99* (8), 3100-3109.
22. Kutluay, S.; Baytar, O.; Şahin, Ö. *Res. Eng. Struct. Mater.* **2019**, *5* (3), 279-298.
23. Ali, R. M.; Hamad, H. A.; Hussein, M. M.; Malash, G. F. *Ecol. Eng.* **2016**, *91*, 317-332.
24. Vora, S.; Khimani, M.; De, C. *Ecol. Eng.* **2013**, *34* (7), 947-956.
25. Salih, W. M.; Gzar, H. A.; Hassan, N. F. *J. Eng.* **2012**, *18* (9), 1042-1054.
26. Laskar, I. I.; Hashisho, Z. *Sep. Purif. Technol.* **2020**, 116681.
27. Abbas, A.; Abussaud, B. A.; Al-Baghli, N. A.; Khraisheh, M.; Atieh, M. A. *J. Nanomater.* **2016**, 2016.
28. Hu, Q.; Zhang, Z. *J. Mol. Liq.* **2019**, *277*, 646-648.
29. Sadeghalvad, B.; Azadmehr, A.; Hezarkhani, A. *RSC Adv.* **2016**, *6* (72), 67630-67642.
30. Wang, C.; Zhong, H.; Wu, W.; Pan, C.; Wei, X.; Zhou, G.; Yang, F. *ACS Omega* **2019**, *4* (1), 1652-1661.



Structural and theoretical study based on DFT calculations of 3-Methyl-4-[3-ethoxy-(2-*p*-metilbenzenesulfonyloxy)-benzylidenamino]-4,5-dihydro-1*H*-1,2,4-triazol-5-one

Gül Kotan^{1,*}, Faruk Kardaş²

¹Department of Chemistry and Chemical Processing Technologies, Kars Vocational School, Kafkas University, Kars, 36000, Turkey

² Education Faculty, Erzincan Binali Yıldırım University, Erzincan, 24100 Turkey

Received: 22 March 2021; Revised: 31 May 2021; Accepted: 01 June 2021

*Corresponding author e-mail: gulkemer@hotmail.com

Citation: Kotan, G.; Kardaş, F. *Int. J. Chem. Technol.* 2021, 2 (1), 42-51.

ABSTRACT

The molecular structure optimization of 3-Methyl-4-[3-ethoxy-(2-*p*-metilbenzenesulfonyloxy)-benzylidenamino]-4,5-dihydro-1*H*-1,2,4-triazol-5-one was obtained using the HF method and "B3LYP, B3PW91" functionals in the DFT method at the 6-31G (d, p) basis sets. The structure characterization performed using infrared (FT-IR), ¹³C-NMR and ¹H-NMR spectral tools. Computational IR data was obtained at the Veda4f program. Theoretical ¹H/ ¹³C-NMR(DMSO) isotropic shift values were assigned according to the GIAO method in the DMSO solvent. All the experimental data were available in the literature, these values are consistent with the calculated. Also, the theoretical results of different functionals were compared with each other. The HOMO-LUMO energies and energy difference (eV) were calculated and three-dimensional images are drawn. The no need to use the electronic parameters have been found using the energy difference (ΔE). The thermodynamics properties, mulliken atomic charges, geometric properties, dipole moments, total energy were calculated. The non linear optical (NLO) analysis was carried out. Additionally, with the MEP surface map, the nucleophilic and electrophilic regions of the molecule were determined.

Keywords: GIAO, Veda4f, MEP, HOMO, LUMO, NLO.

3-Metil-4-[3-etoksi-(2-*p*-metilbenzensülfoniloksi)-benzilidenamino]-4,5-dihidro-1*H*-1,2,4-triazol-5-on'un DFT hesaplamalarına dayalı yapısal ve teorik çalışması

ÖZ

3-Metil-4-[3-etoksi-(2-*p*-metilbenzensülfoniloksi) - benziliden amino]-4,5-dihidro-1*H*-1,2,4-triazol-5-on moleküler yapı optimizasyonu 6-31G (d, p) temel setinde HF metodu ve DFT metodunda B3LYP, B3PW91 fonksiyonları kullanılarak elde edilmiştir. Yapı karakterizasyonu kızılötesi (FT-IR), ¹³C-NMR ve ¹H-NMR spektral araçları kullanılarak gerçekleştirildi. Hesapsal IR verileri Veda4f programında elde edilmiştir. Teorik ¹H/¹³C-NMR isotropik kimyasal kayma değerleri DMSO çözücüsünde GIAO metoduna göre belirlenmiştir. Literatürde tüm deneysel veriler mevcuttu, bu değerler hesaplananlar ile uyumludur. Ayrıca farklı fonksiyonların teorik sonuçları birbirleriyle karşılaştırıldı. HOMO-LUMO enerjileri ve enerji farkı (eV) hesaplanmış ve üç boyutlu şekilleri çizilmiştir. Birçok elektronik parametre bu enerji farkı kullanılarak bulunmuştur. Termodinamik özellikler, mulliken atomik yükleri, geometrik özellikleri, dipol moment, toplam enerji hesaplanmıştır. Doğrusal olmayan optik (NLO) analizi gerçekleştirildi. Ayrıca MEP yüzey haritası ile molekülün nükleofilik ve elektrofilik bölgeleri belirlenmiştir.

Anahtar Kelimeler: GIAO, Veda4f, MEP, HOMO, LUMO, NLO.

1. INTRODUCTION

Schiff's bases, which are synthesized from the reaction of aromatic/heteroaromatic carbonyl groups such as aldehydes or ketones with primary amines. These are

significant compound for organic chemistry. 1,2,4-Triazol derivatives are well-known organic compounds. Therefore, many studies that include their molecular, biological and structural properties are available in the literature.¹⁻⁷ Functional groups in the structure of Schiff

bases determine their active biological activity characteristics.⁸⁻¹⁰ Theoretical studies for Schiff bases have been done on a computer. In this study, we surveyed many calculations parameters of molecule with different functionals. The compound characterized theoretically and experimentally with different techniques such as ¹H/¹³C-NMR, FT-IR. All computations were done with DFT(B3LYP/ B3PW91) and HF methods at the 6-31G(d,p) basis set in the Gaussian 09 W packet program.¹¹⁻¹³ Vibration frequencies at the same theoretical levels were calculated, and the optimized structure (Figure 1) and vibration band spectrum were made with Gauss-View program.¹⁴ The theoretical calculations ¹H/¹³C-NMR were performed by using HF/ B3PW91/ B3LYP 6-31G(d,p) and carbon/ proton chemical shifts were assigned using the method GIAO.¹⁵ Calculated and experimental values were written in the necessary places at equation $\delta_{exp} = a + b \cdot \delta_{calc}$. δ_{calc} and graphics were drawn. Experimental data in the literature¹⁶ were used. To determine the theoretical data, the Veda4f program was used.¹⁷ The theoretical IR values in the gas phase were calculated at the HF and DFT 6-31G (d, p) basis sets, these data are scaled by scaled factors¹⁸. In addition, finally, the LUMO-HOMO energies, $E_{LUMO} - E_{HOMO}$ energy gap (ΔE_g), dipole moments, Mulliken charges, total energy, geometric properties, electronic parameters (ionization potential (I), softness (σ), electronegativity (χ), electron affinity (A) and global hardness (η)), thermodynamics some data (entropy (S), thermal energies (E) and thermal capacity (CV)) were examined. Thus, many substantial theoretical properties of the compound were studied by variant calculation lines. Substances showing nonlinear optical properties can change the frequency, reflection, polarization, and phase of the incident light. For this reason, these materials have started to be used in the production of optical devices, photonics industry, telecommunications, information processing, and computer technology.¹⁹ In recent years, theoretical properties, especially the non-linear properties for organic and organometallic compounds in the numerous studies have been investigated.²⁰⁻²² It is understood from the literature that, organic compounds containing metal complexes with coordinated metal centres attract more attention.²³ The delocalization of conjugated π electrons and π bond conjugation are present in the structure of nonlinear optics. In addition, the optical properties of organic compounds can be increased by adding donor-acceptor groups to the structure. In this study, the HF method and different two function such as B3PW91, B3LYP of the DFT method have also been used to examine the nonlinear optical properties of a substance and theoretically the parameters such as the static dipole moment μ (Debye), the static polarizability α (esu) and the static first-order hyperpolarizability β (esu) are calculated. Theoretical NLO analysis results were

crosscheck the data of the urea reference in the literature.²⁴

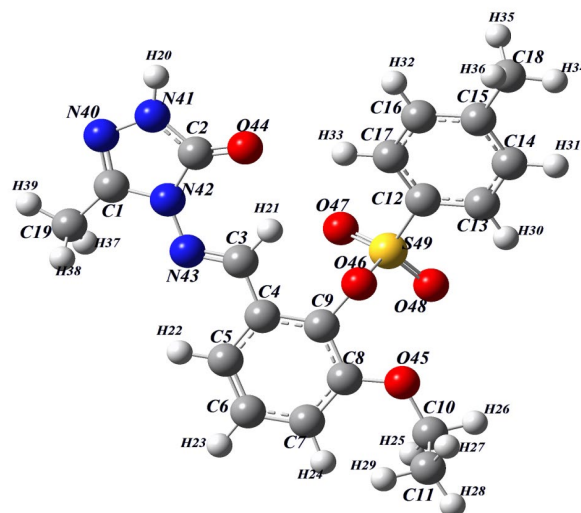


Figure 1. The Gausview structure of the molecule.

2. RESULTS AND DISCUSSION

2.1. NMR analysis

¹³C and ¹H-NMR spectral values calculated no need with using the gauge invariant atomic orbitals method are listed in Table 1 together with the experimental values. While the experimental NH proton signal in the ¹H-NMR is at 11.83 ppm (DMSO), the calculated values with B3PW91, B3LYP, HF are 8.72, 8.63, 7.80 (DMSO) ppm, respectively. This is because of the characteristic NH proton. In the ¹H-NMR, peak of N=CH proton was found for 9.62 ppm (experimental), 11.57 ppm (B3PW91), 11.35 ppm (B3LYP), 10.62 ppm (HF). The aromatic protons were assigned 7.39-7.71 ppm in the experimental and 8.24-9.82 ppm (B3PW91), 8.07-8.95 ppm (B3LYP), 8.16-9.32 ppm (HF). ¹³C NMR spectra of compound showed at 145.63 (C1), 147.6 (C2), 151.73 (C3), 116.48-150.73 and 128.14-144.05 (aromatic C) in the experimental, and 147.15 for B3PW91, 150.84 for B3LYP, 145.60 for HF (C1), 149.86 for B3PW91, 153.31 for B3LYP, 146.99 for HF (C2), 150.00 for B3PW91, 152.56 for B3LYP, 146.94 for HF (C3), 116.45-134.13 and 129.37-148.71 for B3PW91, 118.98-156.99 and 131.51- 151.60 for B3LYP, 118.01- 146.43 and 122.54-147.80 (HF) in the calculation. In the theoretical R² values are B3PW91 (DMSO): ¹H: 0.8985, ¹³C: 0.9983; B3LYP (DMSO): ¹H: 0.9011, ¹³C: 0.9976; HF (DMSO): ¹H: 0.8824, ¹³C: 0.9940. A linear graph was obtained for the experimental and theoretical chemical shift values by looking at the R values (Table 2), the graphs (Figure 2.1 and Figure 2.2).

Table 1. $^1\text{H}/^{13}\text{C}$ -NMR(DMSO) isotropic chemical shifts (δ/ppm) B3PW91, B3LYP, HF

No	Experimental	B3PW91	Differ. B3PW91	B3LYP	Differ. B3LYP	HF	Differ. HF
C1	145.63	147.15	-1.52	150.84	-5.21	145.60	0.03
C2	147.6	149.86	-2.26	153.31	-5.71	146.99	0.61
C3	151.73	150.00	1.73	152.56	-0.83	146.94	4.79
C4	128.75	134.13	-5.38	137.03	-8.28	126.58	2.17
C5	117.27	117.19	0.08	119.67	-2.40	118.01	-0.74
C6	128.22	129.38	-1.16	131.76	-3.54	126.14	2.08
C7	116.48	116.45	0.03	118.98	-2.50	123.19	-6.71
C8	150.73	153.62	-2.89	156.99	-6.26	146.43	4.30
C9	137.39	138.74	-1.35	142.71	-5.32	134.65	2.74
C10	64.23	67.84	-3.61	71.84	-7.61	60.04	4.19
C11	13.99	18.91	-4.92	22.54	-8.55	11.89	2.10
C12	132.21	137.01	-4.80	141.52	-9.31	124.46	7.75
C13	128.14	129.37	-1.23	131.51	-3.37	128.91	-0.77
C14	129.81	130.63	-0.82	132.67	-2.86	122.54	7.27
C15	144.05	148.71	-4.66	151.60	-7.55	147.80	-3.75
C16	129.81	131.60	-1.79	133.81	-4.00	123.77	6.04
C17	128.14	129.71	-1.57	132.40	-4.26	129.04	-0.90
C18	20.94	27.83	-6.89	30.54	-9.60	17.82	3.12
C19	10.95	18.32	-7.37	21.03	-10.08	10.50	0.45
H20	11.83	8.72	3.11	8.63	3.20	7.80	4.03
H21	9.62	11.57	-1.95	11.35	-1.73	10.62	-1.00
H22	7.41	8.93	-1.52	8.74	-1.33	8.75	-1.34
H23	7.4	8.55	-1.15	8.37	-0.97	8.28	-0.88
H24	7.39	8.24	-0.85	8.07	-0.68	8.16	-0.77
H25	3.92	5.38	-1.46	5.30	-1.38	3.95	-0.03
H26	3.92	5.48	-1.56	5.41	-1.49	4.58	-0.66
H27	1.15	2.17	-1.02	2.50	-1.35	0.86	0.29
H28	1.15	1.97	-0.82	1.94	-0.79	1.35	-0.20
H29	1.15	2.55	-1.40	2.15	-1.00	1.19	-0.04
H30	7.71	9.11	-1.40	8.95	-1.24	8.91	-1.20
H31	7.49	8.62	-1.13	8.49	-1.00	8.11	-0.62
H32	7.49	8.82	-1.33	8.60	-1.11	8.27	-0.78
H33	7.71	9.82	-2.11	9.71	-2.00	9.32	-1.61
H34	2.35	3.06	-0.71	3.14	-0.79	2.58	-0.23
H35	2.35	3.62	-1.27	3.52	-1.17	2.98	-0.63
H36	2.35	3.55	-1.20	3.25	-0.90	2.88	-0.53
H37	2.25	3.41	-1.16	3.33	-1.08	2.81	-0.56
H38	2.25	3.40	-1.15	3.32	-1.07	2.86	-0.61
H39	2.25	3.08	-0.83	2.97	-0.72	2.54	-0.29

Table 2. The correlation data for chemical shifts

	^{13}C				^1H			
	R^2	S. hata	a	b	R^2	S. hata	a	b
B3PW91	0.9983	1.9748	1.0339	-6.5366	0.8985	1.0691	0.9970	-1.0278
B3LYP	0.9976	2.3632	1.0340	-9.6467	0.9011	1.0553	1.0137	-1.0110
HF	0.9940	3.7231	0.9940	2.4840	0.8824	1.1509	0.9406	-0.0659

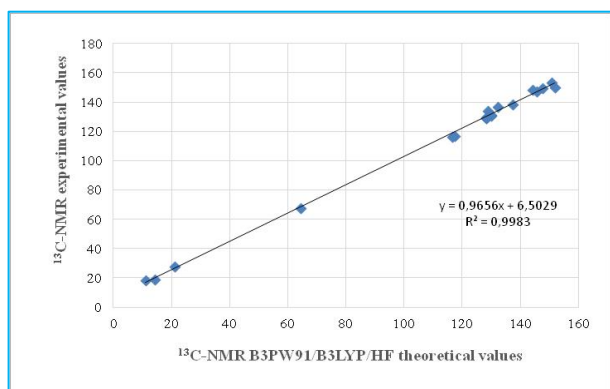


Figure 2.1. The ^{13}C -NMR correlation graphs for B3LYP/B3PW91/HF 6-31G(d,p)/DMSO chemical shifts

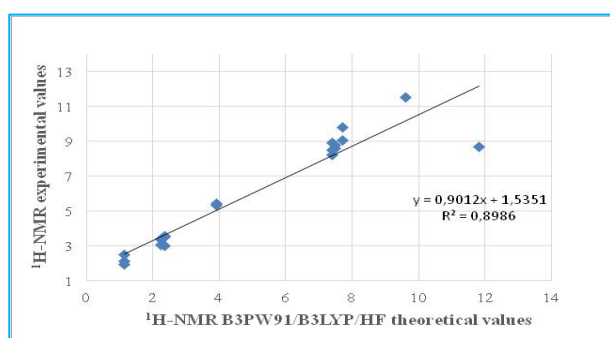


Figure 2.2. The ^1H -NMR correlation graphs for B3LYP/B3PW91/HF 6-31G(d,p)/DMSO chemical shifts

2.2. FT-IR analysis

Infrared vibration frequency values were obtained using the Veda 4 program and these values were multiplied with appropriate scale factors such as 0.9576 for B3PW91/ 6-31G(d,p) level, 0.9617 for B3LYP/ 6-31G(d,p) level, 0.8992 for HF/ 6-31G(d,p) level. The frequency data found in the calculations are positive. The vibration bands of the N-H in the experimental IR spectrum are observed at 3171 cm^{-1} and the theoretical N-H peaks are calculated in the 3562 cm^{-1} for B3PW91, 3114 cm^{-1} for B3LYP, 3104 cm^{-1} for HF. Single weak band at 1696 cm^{-1} in the experimental spectrum was assigned to C=O vibration, the calculated peaks for B3PW91/B3LYP/HF are observed $1754/1739/1763\text{ cm}^{-1}$, respectively. While the experimental C-N peak is at 1596 cm^{-1} , the calculated C-N peak is at 1613 cm^{-1} (B3PW91), 1621 cm^{-1} (B3LYP) and 1718 cm^{-1} (HF). Two weak bands at 1341 and 1152 cm^{-1} in the experimental spectrum were assigned to S=O and S-O vibrations, and respective calculated values are $1341, 1152\text{ cm}^{-1}$ (B3PW91), $1312, 1099\text{ cm}^{-1}$ (B3LYP) and $1310, 1100\text{ cm}^{-1}$ (HF). IR spectra were drawn with obtained values according to DFT(B3PW91/ B3LYP), HF methods (Figure 3). Theoretically IR values were compared with experimentally IR values. The experimental and calculated harmonic vibrational frequencies of molecule were found a linear correlation and are shown in the Figure 3. The results of this comparison were found corresponding with each other of values and were listed in the Table 3.

Table 3. Significant vibrational frequencies (cm^{-1})

Vibrational frequencies	Experimental (cm^{-1})	Computational		
	IR	Scaled B3PW91	Scaled B3LYP	Scaled HF
ν NH	3171	3562	3114	3104
ν C=O	1696	1754	1739	1763
ν C=N	1596	1613	1621	1718
ν S=O	1341 and 1152	1312 and 1099	1288 and 1121	1310 and 1100

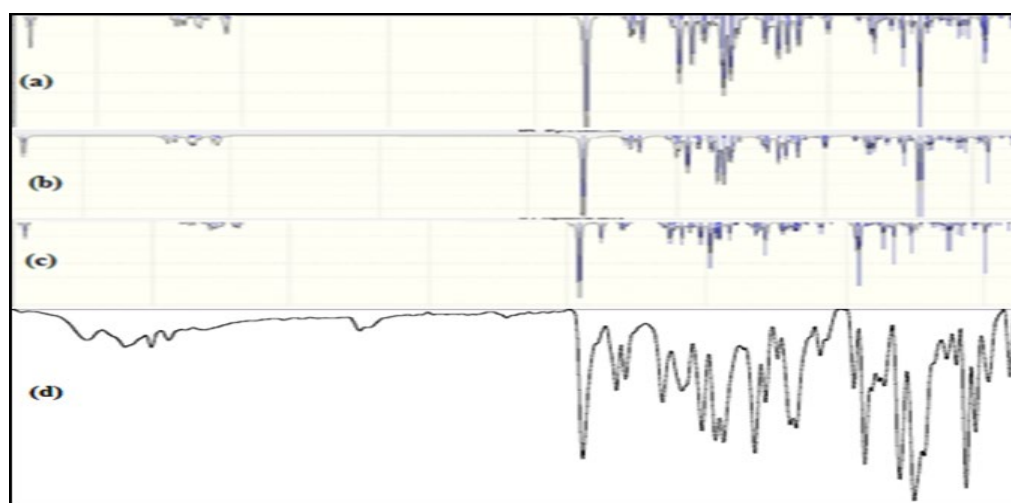


Figure 3. Theoretical IR spectrums and simulated with B3PW91(a)/ B3LYP(b)/ HF(c)/ Experimental(d)

2.3. Molecular geometry

The bond lengths, mulliken atomic charges and bond angles calculated by the HF and DFT method with 6-31G(d,p) basis set (Table 4-6). According to this data, the highest bond length is between C(49)-C(12) atoms that these values are 1.779/1.770/1.754 Å for B3LYP/B3PW91/HF methods. Additionally, respective the bond lengths in the triazole ring N40-N41, N40-C1, C2-O44, C2-N42, N42-C1 are calculated

1,381/1.372/1,371;1,226/1.224/1.205;1.415/1.411/1.38; 1.415/1.411/1.385 Å at the HF/ B3LYP/ B3PW91 (Table 4). In the literature, N-N, C=O, N=C bond lengths are assigned as 1.404, 1.212, 1.280 Å.^{25,26} The calculated bond length values are consistent with literature values. The highest bond angle is between N(41)-C(2)-N(44), which is 129.412/129.466/129.028° for B3LYP/ B3PW91/HF (Table 5). The mulliken charge distribution of the atoms was done²⁷.

Table 4. The calculated bond lengths with B3LYP/ B3PW91/ HF 6-31G(d,p)

Bond Lengths	B3LYP	B3PW91	HF	Bond Lengths	B3LYP	B3PW91	HF
C(1)-N(40)	1.300	1.299	1.269	C(11)-H(27)	1.093	1.093	1.086
C(1)-N(42)	1.388	1.384	1.378	C(11)-H(28)	1.095	1.094	1.083
C(1)-C(19)	1.486	1.481	1.488	C(11)-H(29)	1.093	1.093	1.084
N(41)-N(40)	1.381	1.372	1.371	C(8)-C(9)	1.411	1.409	1.390
N(41)-H(20)	1.006	1.005	0.990	C(9)-C(4)	1.403	1.400	1.390
N(41)-C(2)	1.368	1.365	1.344	C(9)-O(46)	1.394	1.388	1.384
C(2)-O(44)	1.226	1.224	1.205	O(46)-S(49)	1.694	1.681	1.612
C(2)-N(42)	1.415	1.411	1.385	S(49)-O(47)	1.461	1.457	1.425
N(42)-N(43)	1.375	1.365	1.367	S(49)-O(48)	1.459	1.454	1.420
N(43)-C(3)	1.288	1.286	1.258	S(49)-C(12)	1.779	1.770	1.754
C(3)-H(21)	1.082	1.084	1.069	C(12)-C(13)	1.394	1.391	1.383
C(4)-C(3)	1.465	1.462	1.477	C(12)-C(17)	1.396	1.395	1.388
C(5)-C(4)	1.406	1.404	1.391	C(13)-C(14)	1.392	1.391	1.384
C(9)-C(4)	1.403	1.400	1.390	C(13)-H(30)	1.083	1.084	1.073
C(5)-H(22)	1.083	1.083	1.072	C(14)-H(31)	1.086	1.086	1.075
C(5)-C(6)	1.385	1.383	1.379	C(14)-C(15)	1.401	1.398	1.389
C(6)-H(23)	1.085	1.086	1.075	C(15)-C(16)	1.402	1.402	1.393
C(6)-C(7)	1.399	1.397	1.385	C(16)-H(32)	1.086	1.086	1.075
C(7)-H(24)	1.082	1.083	1.074	C(16)-C(17)	1.392	1.389	1.379
C(8)-C(7)	1.398	1.396	1.384	C(17)-H(33)	1.085	1.086	1.074
C(8)-O(45)	1.353	1.348	1.349	C(15)-C(18)	1.509	1.504	1.509
O(45)-C(10)	1.431	1.425	1.417	C(18)-H(34)	1.093	1.092	1.083
C(10)-H(25)	1.096	1.097	1.086	C(18)-H(35)	1.097	1.096	1.086
C(10)-H(26)	1.093	1.093	1.081	C(18)-H(36)	1.093	1.094	1.084
C(10)-C(11)	1.524	1.519	1.518				

Table 5. The calculated bond angles with B3LYP/ B3PW91/HF 6-31G(d,p)

Bond Angle	B3LYP	B3PW91	HF	Bond Angle	B3LYP	B3PW91	HF
N(40)-C(1)-N(42)	111,513	111,396	111,345	C(8)-O(45)-C(10)	120,154	119,832	117,816
N(40)-N(41)-C(2)	114,522	114,668	113,736	O(45)-C(10)-H(25)	110,123	110,168	109,841
N(40)-N(41)-H(20)	120,440	120,393	120,993	O(45)-C(10)-H(26)	104,239	104,265	104,837
H(20)-N(41)-C(2)	125,037	124,938	125,265	O(45)-C(10)-C(11)	112,321	112,391	110,708
N(41)-C(2)-O(44)	129,412	129,466	129,028	C(10)-C(11)-H(27)	110,190	110,189	109,686
O(44)-C(2)-N(42)	129,285	129,315	128,958	C(10)-C(11)-H(28)	109,929	109,990	110,562
N(40)-C(1)-C(19)	125,131	125,260	125,417	C(10)-C(11)-H(29)	112,010	112,052	111,496
N(42)-C(1)-C(19)	123,356	123,344	123,238	C(9)-O(46)-S(49)	114,563	116,841	119,909
C(1)-C(19)-H(37)	110,904	110,896	110,474	O(46)-S(49)-O(47)	107,146	107,217	106,916
C(1)-C(19)-H(38)	110,978	110,959	110,537	O(46)-S(49)-O(48)	110,244	109,417	109,150
H(39)-C(19)-C(1)	108,650	108,621	108,548	S(49)-C(12)-C(13)	118,735	118,746	119,105
H(37)-C(19)-H(38)	107,340	107,388	107,886	S(49)-C(12)-C(17)	119,463	119,446	119,528
H(37)-C(19)-H(39)	109,498	109,501	109,736	C(12)-C(13)-C(14)	118,724	118,717	119,022
H(38)-C(19)-H(39)	109,450	109,457	109,653	C(12)-C(13)-H(30)	119,906	119,848	120,005
N(42)-N(43)-C(3)	118,260	118,335	119,143	H(30)-C(13)-C(14)	121,369	121,434	120,971
N(43)-C(3)-H(21)	122,415	122,445	122,518	C(13)-C(14)-H(31)	119,352	119,354	119,290
H(21)-C(3)-C(4)	118,122	118,289	117,909	H(31)-C(14)-C(15)	119,552	119,545	119,931
C(3)-C(4)-C(5)	122,025	121,978	121,745	C(13)-C(14)-C(15)	121,095	121,101	120,878
C(4)-C(5)-H(22)	118,657	118,600	118,873	C(14)-C(15)-C(18)	120,768	121,029	120,931
H(22)-C(5)-C(6)	121,361	121,469	120,831	C(14)-C(15)-C(16)	118,603	118,603	118,860
C(4)-C(5)-C(6)	119,981	119,930	120,295	C(15)-C(16)-H(32)	119,625	119,614	119,771
C(5)-C(6)-H(23)	119,879	119,896	119,920	H(32)-C(16)-C(17)	118,946	118,978	119,081
H(23)-C(6)-C(7)	118,986	118,970	119,641	C(16)-C(17)-H(33)	120,392	120,521	120,338
C(5)-C(6)-C(7)	121,129	121,127	120,394	H(33)-C(17)-C(12)	121,258	121,110	120,937
C(6)-C(7)-H(24)	119,517	119,485	120,858	C(15)-C(18)-H(34)	111,529	111,621	111,406
H(24)-C(7)-C(8)	120,349	120,333	118,745	C(15)-C(18)-H(35)	110,844	110,894	110,541
C(7)-C(8)-C(9)	120,132	118,405	118,693	C(15)-C(18)-H(36)	111,399	111,212	111,042
C(7)-C(8)-O(45)	125,717	125,785	121,215				

The electronegative nitrogen (N), oxygen (O) atoms have negative charge values. C2 atom is surrounded by three electronegative atoms (N41, N42, O44) have negative charges values. The H20-H39 have positive atomic charge values. Also, there is an exceptional case where the sulfur atom is electronegative atom but positive

charged and has the highest mulliken charge. This value is 1.273/1.299/1.723⁰ for B3LYP/B3PW91/HF methods (Table 6). This is because, the sulfur atom is surrounded by three oxygen atoms which are more electronegative atom than the sulfur.

Table 6. The calculated mulliken charges datas B3LYP/ B3PW91/HF 6-31G(d,p)

	B3LYP	B3PW91	HF		DFT	B3PW91	HF
C1	0.524	0.535	0.594	H26	0.125	0.131	0.134
C2	0.824	0.858	1.062	H27	0.128	0.154	0.111
C3	0.153	0.149	0.230	H28	0.110	0.142	0.137
C4	0.088	0.053	-0.071	H29	0.118	0.135	0.125
C5	-0.119	-0.140	-0.131	H30	0.134	0.168	0.209
C6	-0.091	-0.129	-0.145	H31	0.091	0.127	0.158
C7	-0.133	-0.166	-0.167	H32	0.098	0.141	0.165
C8	0.369	0.202	0.402	H33	0.164	0.154	0.248
C9	0.210	0.373	0.305	H34	0.119	0.159	0.129
C10	0.045	-0.014	0.099	H35	0.135	0.134	0.145
C11	-0.335	-0.409	-0.352	H36	0.123	0.196	0.137
C12	-0.203	-0.242	-0.376	H37	0.146	0.172	0.161
C13	-0.072	-0.098	-0.090	H38	0.141	0.166	0.152
C14	-0.128	-0.150	-0.172	H39	0.140	0.167	0.160
C15	0.132	0.104	0.017	N40	-0.335	-0.338	-0.351
C16	-0.127	-0.153	-0.170	N41	-0.433	-0.466	-0.565
C17	-0.067	-0.091	-0.091	N42	-0.408	-0.443	-0.617
C18	-0.382	-0.048	0.347	N43	-0.330	-0.332	-0.328
C19	-0.368	-0.434	-0.359	O44	-0.547	-0.557	-0.670
H20	0.288	0.311	0.339	O45	-0.512	-0.510	-0.670
H21	0.167	0.194	0.236	O46	-0.631	-0.626	-0.795
H22	0.105	0.141	0.184	O47	-0.529	-0.527	-0.681
H23	0.092	0.128	0.163	O48	-0.502	-0.504	-0.641
H24	0.094	0.129	0.172	S49	1.273	1.299	1.723
H25	0.106	0.153	0.102				

2.4. FMO's analysis

Frontier molecular orbitals were defined the electronic transitions, kinetic stability, optical and electric properties.²⁸ The molecular orbital surfaces for LUMO: lowest unoccupied molecular orbital, HOMO: highest occupied molecular orbital are shown in Figure 4. The energy levels are 4.4307/4.4186/10.976 eV for different HF- DFT methods. The energy difference (ΔE_g) between LUMO - HOMO orbitals is a basic feature that provides important information about the stability and some electronic properties of the structure.²⁹ We can say

that, the structure calculated with the DFT (B3LYP) set is more stable than the others. The positions of the LUMO-HOMO orbitals of the molecule were calculated with all three basic sets, and it was seen that these orbitals are usually concentrated in the triazole and benzene ring. The electronic properties of molecule such as electron affinity (A), softness (S), chemical potential (P_i), electronegativity (χ), Nucleophilic index (IP), global hardness (η), electrophilic index (ω), chemical potential (μ) and ionization potential (I) was calculated using the equations given below for B3PW91/B3LYP/HF basis sets are showed in Table 7.

Table 7. The calculated electronic structure parameters of the molecule

	eV	B3PW91	B3LYP	HF
	LUMO	-1,57632	-1,50067	2,30556
	HOMO	-6,0005	-5,91914	-8,67015
A	Electron affinity	1,57632	1,50067	-2,30556
I	Ionization potential	6,0005	5,91914	8,67015
ΔE	Energy gap	4,42419	4,41847	10,9757
χ	Electronegativity	3,78841	3,70991	3,18229
Pi	Chemical potential	-3,78841	-3,70991	-3,18229
ω	Electrophilic index	0,02144	0,02053	0,03753
IP	Nucleophilic index	-0,30798	-0,30121	-0,6418
S	Molecular softness	334,716	335,148	134,92
η	Molecular hardness	2,21209	2,20924	5,48785

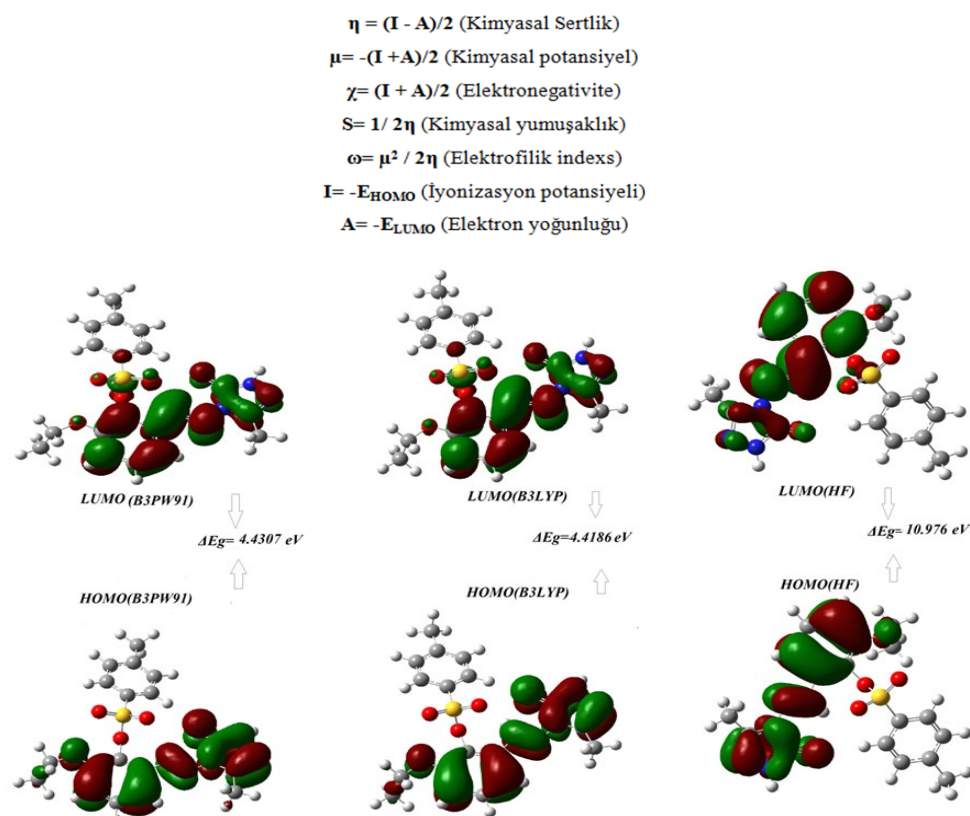


Figure 4. HOMO-LUMO and ΔE_g energy of the molecule

2.5. Thermodynamics properties

Thermodynamics calculations were calculated with diverse three method such as HF and B3PW91, B3LYP at the 6-31G(d,p) basis set under 1 atm pressure and at 298.150 K. The electronic, rotational, translational and vibrational data, Entropy, Enthalpy were computed and were seen in table 8. The zero-point vibrational energies were calculated as 238.0056, 237.1275, 254.8937 kcal/mol by different methods. The computed thermal energy (E), heat capacity (Cv), entropy (S) values are 255.394/254.559/271.244kcal/mol;190.252/189.833/184.120 cal; 103.033/103.369/95.763 cal for B3PW91/B3LYP/ HF, respectively.

2.7. The surface maps

The immersive shapes of MEP known as molecular electrostatic potential maps. The surface of MEP map was shown molecular shape, size, charge distribution and electrostatic potential value. Molecular electrostatic potential, molecular electrophilic and nucleophilic determination of regions where reactions may occur and the formation of intramolecular hydrogen bonds provides important information. The regions with the highest electron density are around the O44, O45, O46, O47, O48 atoms. The section of the electronegativity oxygen atom is red colour in the MEP. The around of hydrogen atoms

are positive potential region. The -NH region is the region with the lowest electron density and is blue in the MEP map. Furthermore, the total density, contour maps (the electrostatic potential, the electron spin potential (ESP) map, the electron density are shown in Figure 5.

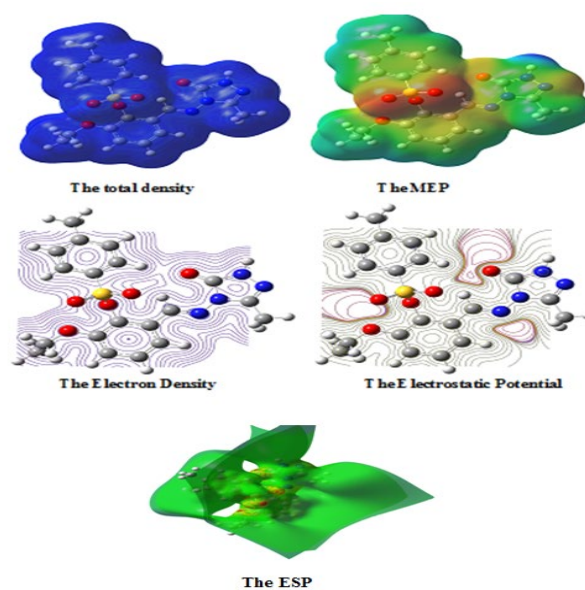


Figure 5. The calculated molecular surface maps of the molecule

Table 8. The thermodynamics parameters of the molecule

Parameters	B3PW91	B3LYP	HF
Rotational temperatures (Kelvin)			
A	0.00773	0.00767	0.00853
B	0.00621	0.00621	0.00615
C	0.00371	0.00369	0.00396
Rotational constants (GHZ)			
A	0.16111	0.15973	0.17765
B	0.12940	0.12941	0.12819
C	0.07727	0.07681	0.08252
Thermal Energies E(kcal/mol)			
Translational	0.889	0.889	0.889
Rotational	0.889	0.889	0.889
Vibrational	253.616	252.781	269.467
Total	255.394	254.559	271.244
Thermal Capacity CV(cal/mol-K)			
Translational	2.981	2.981	2.981
Rotational	2.981	2.981	2.981
Vibrational	97.071	97.407	89.801
Total	103.033	103.369	95.763
Entropy S(cal/mol-K)			
Translational	43.968	43.968	43.968
Rotational	36.543	36.558	36.390
Vibrational	109.741	109.308	103.762
Total	190.252	189.833	184.120
Zero-point correction (Hartree/Particle)	0.379286	0.377887	0.406199
Thermal correction to Energy	0.406996	0.405665	0.432255
Thermal correction to Enthalpy	0.407940	0.406609	0.433199
Thermal correction to Gibbs Free Energy	0.317545	0.316413	0.345718
Sum of electronic and zero-point Energies	-1728.381703	-1728.935236	-1720.276579
Sum of electronic and thermal Energies	-1728.353993	-1728.907458	-1720.250523
Sum of electronic and thermal Enthalpies	-1728.353048	-1728.906514	-1720.249578
Sum of electronic and thermal Free Energies	-1728.443443	-1728.996710	-1720.337060
Zero-point vibrational energy (Kcal/mol)	238.00565	237.12754	254.89372

2.7. NLO analysis

The compound within gaseous phase, the dipole moment (μ), the static polarizability (α) and the static hyperpolarizability (β) values were computed by the B3PW91/B3LYP/HF 6-31G(d,p) levels. Then, the μ_{total} , α_{total} , $\Delta\alpha$ and β values were calculated by using the following equation 1-4. In the Gaussian 09W program, the 10 values obtained from the frequency output file provide the components " β_{xxx} , β_{xxy} , β_{xyy} , β_{yyy} , β_{xxz} , β_{xyz} , β_{yyz} , β_{xzz} , β_{yzz} , β_{zzz} " and 6 values provide " α_{xx} , α_{xy} , α_{yy} , α_{xz} , α_{yz} , α_{zz} " components, respectively. The polarizability α and hyperpolarizability β values are found in the Gaussian 09 W output in atomic units (au), but the calculated values (α : 1 a.u. = 0.1482×10^{-24} esu; β : 1 a.u. = 8.6393×10^{-33} esu) have been converted into electrostatic units (esu).³⁰ As a result of the calculation, the

polarizability α (esu) 40.5608, 40.7313, 35.3210; the hyperpolarizability β (esu) 44.726, 38.434, 25.514; $\Delta\alpha$ (esu) 30.7458, 43.872, 24.4372; total energy values E_{total} (Hartree) -1728.7609, -1729.3131, -1720.6827; dipole moments μ_{total} (Debye) 2.9995, 2.8513, 4.3705 for B3PW91/B3LYP/HF, respectively are obtained and are listed in the Table 9. These values were compared with urea used as reference material for NLO analysis.²⁴ The lowest values for static α_{total} , $\Delta\alpha$ and β_0 parameters are calculated for HF 6-31G(d,p) basis set. The calculated highest values are DFT 6-31G(d,p). When NLO values were compared with the urea reference, it was seen that the calculated values were high. This result showed that the target molecule studied could be a good non-linear optics. The calculated highest dipole moment and energy values are equal to 4.3705 D, -1720.6827 Hartree for HF 6-31G(d,p).

$$\mu_{total} = (\mu_x^2 + \mu_y^2 + \mu_z^2)^{1/2} \quad (1)$$

$$\alpha_{total} = \frac{1}{3}(\alpha_{xx} + \alpha_{yy} + \alpha_{zz}) \quad (2)$$

$$\Delta\alpha = \frac{1}{\sqrt{2}}[(\alpha_{xx} - \alpha_{yy})^2 + (\alpha_{yy} - \alpha_{zz})^2 + (\alpha_{zz} - \alpha_{xx})^2 + 6\alpha_{xz}^2 + 6\alpha_{xy}^2 + 6\alpha_{yz}^2]^{1/2} \quad (3)$$

$$\beta_0 = [(\beta_{xxx} + \beta_{xyy} + \beta_{xzz})^2 + (\beta_{yyy} + \beta_{yzz} + \beta_{yxx})^2 + (\beta_{zzz} + \beta_{zxx} + \beta_{zyy})^2]^{1/2} \quad (4)$$

Table 9. The total energy E_{total} (Hartree), the electric dipole moment μ (Debye), the polarizability α_{total} (10^{-24} esu) and first hyperpolarizability β_{total} (10^{-30} esu) of molecule

	B3PW91	B3LYP	HF
E_{total}	-1728.7609	-1729.3131	-1720.6827
μ_x	-1.4211	-1.3036	0.9292
μ_y	-0.2443	-0.1692	0.3656
μ_z	-2.6302	-2.5303	-4.2549
μ_{total}	2.9995	2.8513	4.3705
α_{xx}	52.0842	52.4450	43.9587
α_{xy}	-2.1511	-2.0712	-0.6171
α_{yy}	49.2834	49.6355	42.3741
α_{xz}	0.9258	-0.096	-1.7200
α_{yz}	3.5654	-0.05480	-3.3081
α_{zz}	20.3148	20.1135	19.6304
α_{total}	40.5608	40.7313	35.3210
$\Delta\alpha$ (esu)	30.7458	43.8721	24.4372
β_{xxx}	-174.5371	-222.6027	-87.7462
β_{xxy}	2147.0301	2144.3528	1267.0015
β_{xyy}	-524.7104	-392.4142	345.8169
β_{yyy}	1762.4370	1534.7716	1091.8588
β_{xxz}	-301.1789	-58.9649	41.2330
β_{xyz}	-144.6296	-163.6300	-342.266
β_{yyz}	-907.5031	-922.0171	-184.9104
β_{xzz}	-82.9623	-126.6322	-275.2913
β_{yzz}	185.603	17.9446	176.7186
β_{zzz}	2225,8537	49.3528	370.4360
β_{total}	44.726	38.434	25.514

3. CONCLUSIONS

In this theoretical work, different calculations of determining target molecule were carried out by HF and DFT methods with the 6-31G(d, p) basis sets at the program package Gaussian G09W. The $^1\text{H}/^{13}\text{C}$ -NMR chemical shifts and FT-IR data in the calculations are seen to be compatible with the empirical data. A linear correlation was observed in the R^2 values, but there is a slight deviation in the H-NMR correlation graph. The reason for this deviation is the N-H acidic proton (H20) in the molecule. Also, the infrared data was not found negative frequency and the only reason for this is the stability of the molecule. In addition, the LUMO-HOMO energy, geometric properties, ΔE energy gap, total energy, electronic some properties, dipole moments, thermodynamics data were calculated. The reliability of different methods in theoretical computation was discussed. The surface maps of molecule were visualized, and the most electrophilic and nucleophilic regions were detected. In addition, NLO analysis results were examined. The hyperpolarizability β , the polarizability α were compared with urea, and NLO "the non-linear optical" properties of the target compound were defined to be good.

Conflict of interests

I declare that there is no a conflict of interest with any person, institute, company, etc.

REFERENCES

1. Yamada, S. *Coord. Chem. Rev.* **1999**, 190, 537-555.
2. Cozzi, P. G. Metal-alen Schiff base complexes in catalysis: practical aspects, *Chem. Soc. Rev.* **2004**, 33, 410-421.
3. Akiyama, T.; Itoh, J.; Yokota, K.; Fuchibe, K. Enantio selective Mannich-Type Reaction Catalyzed by a Chiral Bronsted Acid, *Angew. Int. Ed.* **2004**, 43, 1566-1568.
4. Gupta, K. C.; Sutar, A. K. *Coord. Chem. Rev.* **2008**, 252, 1420-1450.
5. Sakmar, T. P.; Franke, R. R.; Khorana, H.G. *PNAS.* **1989**, 86, 8309-8313.
6. Dharmaraj, N.; Viswanathamurthi, P.; Natarajan, K. Complexes Containing Bidentate Schiff Bases and Their Antifungal Activity, *Trans.Met.Chem.* **2001**, 26, 105-109.
7. Pandeya, S. N.; Sriram, D.; Nath, G.; DeClercq, E.. Synthesis, antibacterial, antifungal and anti-HIV activities of Schiff and Mannich bases derived from isatin derivatives and N-[4-(4'chlorophenyl)thiazol-2-yl] thiosemicarbazide, *Eur. J.Pharm.Sci.* **1999**, 9, 25-31.
8. Sztanke, K.; Maziarka, A.; Osinka, A.; Sztanke, M. *Bioorg.Med. Chem.* **2013**, 21, 3648-3666.

9. Vicini, P.; Geronikaki, A.; Incerti, M.; Busonera B.; Poni G.; Cabras C. A.; La Colla P. *Bioorg. Med. Chem.* **2003**, 11, 4785-4789.
10. Pandeya, S. N.; Sriram, D.; Nath, G.; De Clercq, E. *Pharm. Acta Helv.* **1999**, 74, 11-17.
11. Becke, A. D. *The J. Chem. Phys.* **2009**, 98, 5648.
12. Lee, C.; Yang, W. T.; Parr, R. G. Development of the Colle-Salvetti correlation-energy formula into a functional of the electron density. *Phys. Rev. B*, **1988**, 37, 785.
13. Frisch, M. J.; Trucks, G. W.; Schlegel, H. B.; Scuseria, G. E.; Robb, M. A.; Mennucci, B.; Petersson, G. A.; Nakatsuji, H.; Caricato, M.; Li, X. et al. *Gaussian 09, Revision C.01*, Gaussian, Inc., Wallingford, CT. **2009**.
14. Dennigton, II R.; Keith, T.; Millam, J. *GaussView, Version 4.1.2*, Semichem, Inc., Shawnee Mission, KS. **2007**.
15. Wolinski, K.; Hilton, J. F. and Pulay, P. *J. Am. Chem. Soc.* **1990**, 112, 512.
16. Kardaş, F.; Manap, S.; Gursoy Kol, Ö.; Beytur, M.; Yüksek, H. Synthesis and Antioxidant Properties of Some 3-Alkyl(Aryl)-4-[3-ethoxy-2-(4-toluenesulfonyloxy)-benzylidenamino]-4,5-dihydro-1H-1,2,4-triazol-5-ones, *Der. Pharm. Chem.* **2016**, 8(18), 274-281.
17. Jamróz, M. H. *Vibrational Energy Distribution Analysis: VEDA 4 program*, Warsaw. **2004**.
18. Merrick, J. P.; Moran, D.; Radom, L. An Evaluation of Harmonic Vibrational Frequency Scale Factors, *J. Phys. Chem.* **2007**, 111 (45), 11683-11700.
19. Nalwa, H.S.; Miyata, S.; *Nonlinear Optics of Organic Molecules and Polymers*, CRC Press, BocaRaton, **1997**.
20. Ulufer, S.; Gürsoy-Kol, Ö.; Yüksek, H. & Kayalar, M. T. 3-Metil-4-[3-(2-metilbenzoksi)-benzilidenamino]-4,5 - dihidro - 1H - 1,2,4 - triazol - 5 - on Bileşiğinin Spektroskopik Özelliklerinin Deneysel ve Teorik Olarak İncelenmesi. *KAÜ Fen Bil. Enst. Derg.* **2004**, 7(1),15-28.
21. Ulaş, Y. Experimental and Theoretical Studies of 2-(naphthalen-1-yl (piperidin-1-yl) methyl) phenol Compound. *J. Chem. Soc. Pak.* **2020**, 42(6), 818-826.
22. Ulaş, Y. Natural bond orbital (NBO) population analysis and non-linear optical (NLO) properties of 2-(azepan-1-yl (naphthalen-1-yl) methyl) phenol. *Int. J. Chem. Technol.* **2020**, 4(2), 138-145.
23. Liyanage, P. S.; Silva de R. M. & Silva de K. N. Nonlinear optical (NLO) properties of novel organometallic complexes: high accuracy density functional theory (DFT) calculations. *J. Mol. Struct.: Theochem*, **2003**, 639(1-3), 195-201.
24. J., Ed. *Molecular Non linear Optics: Materials, Physics and Devices*, Zyss, Boston: Academic Press, **1994**.
25. Ocak, N.; Çoruh, U.; Kahveci, B.; Şaşmaz, S.; Vazquez-Lopez, EM.; Erdönmez, A. 1- Acetyl-3-(p-chlorobenzyl)-4-(p- chlorobenzylidenamino)- 4,5-dihydro-1H-1,2,4-triazol-5-one, *Acta Cryst. Sec. E.* **2003**, 59(6), 750-752.
26. Ustabas, R.; Çoruh, U.; Sancak, K.; Ünver, Y.; Vazquez-Lopez, E. M. 1-(benzoylmethyl)-4-[(2,4-dichlorobenzylidene)amino]-3-(2-thienylmethyl)4,5-dihydro-1H-1,2,4-triazol-5-one, *Acta Cryst. Sec. E.* **2007**, 63, 2982-3051.
27. Mulliken, R. S. Electronic Population Analysis on LCAO-MO Molecular Wave Functions, *Int. J. Chem. Phys.* **1955**, 23, 1833-1840.
28. Fleming, I. *Frontier Orbitals and Organic Chemical Reactions*. Wiley, London. **1976**.
29. Pearson, R.G. Absolute elektronegativity and hardness correlated with molecular orbital theory. *Proc. Natl. Acad. Sci.* **1986**.
30. Ahmed, A. B.; Feki, H.; Abid, Y.; Boughzala, H. & Mlayah, A. Structural, vibrational and theoretical studies of l-histidine bromide. *J. Mol. Struct.*, **2008**, 888(1-3), 180-186.



The anticancer activity of chalcone compounds against human prostate carcinoma cell and human colon colorectal adenocarcinoma

Bedriye Seda KURŞUN AKTAR¹, Ayşe ŞAHİN YAĞLIOĞLU^{2,*}, Emine Elçin ORUÇ-EMRE³

¹Department of Property Protection and Security, Yapraklı Vocational School, Çankırı Karatekin University, 18000, Çankırı, Turkey

²Technical Sciences Vocational School, Department of Chemistry and Chemical Process Technology, Amasya University, 05200, Amasya, Turkey

³ Department of Chemistry, Faculty of Arts and Sciences, Gaziantep University, 27000, Gaziantep, Turkey

Received: 4 April 2021; Revised: 01 June 2021; Accepted: 01 June 2021

*Corresponding author e-mail: aysesahin1@gmail.com

Citation: Kurşun, Atar, B. S.; Şahin, Yağlıoğlu, A.; Oruç- Emre, E. E. *Int. J. Chem. Technol.* 2021, 5 (1), 52-58.

ABSTRACT

Cancer is the second most common cause of death in our country and also worldwide. In the cancer treatment are used many methods such as surgery, chemotherapy, radiotherapy and hormone therapy. Despite these methods, a decrease is not observed in cancer cases and in the mortality. In addition, cancer drugs cause serious side effects. Therefore, there is a need for new anticancer drugs. Chalcones have broad anticancer activity against various cancer cells. In this study, the anticancer activities of the chalcone compounds were investigated against PC3 (Human Prostate Carcinoma Cell) and HT29 (Human colon colorectal adenocarcinoma) cell lines. The anticancer activity tests were performed using the BrdU ELISA method. 5-Fluorouracil (5-FU) was used as the positive control. Compound 1-7 (except Compound 3) were determined having higher anticancer activity than 5-FU against PC3 cancer cells. IC₅₀ values of the compounds 1-7 against PC3 cancer cells were 2.53±0.02 µM; 4.40±0.03 µM; 5.86±0.02 µM; 4.36±0.03 µM; 1.76±0.02 µM; 1.78±0.03 µM; 2.31±0.03 µM, respectively.

Keywords: HT29, PC3, Chalcone, 5-Fluorouracil, Fluor atom, anticancer activity.

Kalkon bileşiklerinin insan prostat karsinom hücresi ve kolon kolorektal adenokarsinomuna karşı antikanser aktivitesi

ÖZ

Kanser, ülkemizde ve dünya çapında en yaygın ikinci ölüm nedenidir. Kanser tedavisinde ameliyat, kemoterapi, radyoterapi ve hormon tedavisi gibi birçok yöntem kullanılmaktadır. Bu yöntemlere rağmen kanser vakalarında ve ölümlerde azalma gözlenmemektedir. Ayrıca kanser ilaçları ciddi yan etkilere neden olur. Bu nedenle yeni antikanser ilaçlara ihtiyaç vardır. Kalkonlar, çeşitli kanser hücrelerine karşı geniş bir antikanser aktivitesine sahiptir. Bu çalışmada kalkon türevlerinin antikanser aktiviteleri PC3 (insan prostat karsinom hücresi) ve HT29 (İnsan kolon kolorektal adenokarsinom) hücre hatlarına karşı araştırılmıştır. Antikanser aktivite testleri BrdU ELISA yöntemi kullanılarak yapıldı. Pozitif kontrol olarak 5-Fluorourasil (5-FU) kullanıldı. Bileşik 1-7 (Bileşik 3 hariç), PC3 kanser hücrelerine karşı 5-FU'dan daha yüksek antikanser aktiviteye sahip olduğu belirlendi. Bileşik 1-7'nin PC3 kanser hücrelerine karşı IC₅₀ değerleri sırasıyla, 2.53±0.02 µM; 4.40±0.03 µM; 5.86±0.02 µM; 4.36±0.03 µM; 1.76±0.02 µM; 1.78±0.03 µM; 2.31±0.03 µM'di.

Anahtar Kelimeler: HT29, PC3, Kalkon, 5-Fluorourasil, Flor atomu, Antikanser aktivite.

1. INTRODUCTION

Cancer is the second most common cause of death in our country and also worldwide. One out of every 5 people

in the world gets cancer during their lifetime. 1 in every 8 men and 1 in every 11 women die of cancer.¹ The most common cancers seen in men are lung, prostate and colorectal cancers. In women, breast, lung, colorectal and

cervical cancers are seen the most common.¹ According to current estimates, 19.3 million new cases were diagnosed in 2020, and the cancer burden increased to 19.3 million new cases and 10.0 million deaths in 2020.¹ The top 5 most common types of cancer in our country in 2020 were lung cancer (17.6%), breast cancer (10.3%), colorectal (colon) cancer (9.1%), prostate cancer (8.3%) and thyroid cancer (5.9%). These 5 types of cancer accounted for more than 50% of all cancers.²

Worldwide, 14 million new cases of prostate cancer diagnosed and 375,304 prostate cancer (PCA) deaths occurred in 2020. The second most common cancer in men is PCA in 2020.¹ This type of cancer ranks fifth among cancer-related deaths. PCA is the most common cancer among men in more than half of the countries of the world. (105 out of 185); particularly in America, Northern and Western Europe, Australia/New Zealand and a large part of Sub-Saharan Africa.³ The natural course of this disease is quite heterogeneous and is still poorly understood. As a result of autopsy studies, prostate cancer is diagnosed in about one out of every three men over the age of 50. 80% of these tumours are 0.5 cm in size and low grade. In addition, the majority are considered to be clinically insignificant.⁴ Increasing incidences and mortality due to PCA and the failure of traditional chemo and radiotherapy of advanced invasive PCA show that essentially new approaches are needed to control this malignancy.^{5,6}

In 2020, there were more than 1.9 million new colorectal cancer diagnoses and 935,000 deaths. This situation shows that approximately one out of every 10 cases of cancer results in death. Generally, colorectal cancer ranks third in terms of the incidence and second in mortality.³ If diagnosed and treated at the early stages, colorectal cancer is one of the most treatable types of cancer.⁷ Various systemic treatments such as surgery, chemotherapy, radiotherapy and hormone therapy are

used for cancer treatment.^{8,9} Despite these treatment methods, a decrease is not observed neither in the number of patients with this disease nor in the mortality rate.⁹ In addition, cancer drugs cause toxicity in normal cells and tissues, causing serious side effects such as vomiting, nausea, hair loss, and resistance development.^{3,10-11} Therefore, there is a need for anticancer drugs that are reliable, powerful, non-toxic, economical and environment friendly. In a study we conducted in 2017, we synthesized the chalcone derivatives included in the present article and investigated the anticancer activities against HeLa and C6 cancer cells. As a result of our research, it was determined that these molecules showed higher anticancer effects than 5-Fluorouracil and Cisplatin, which were used as positive controls.¹² Thus, we examined the anticancer activities of these chalcone derivatives against PC3 (Human Prostate Carcinoma Cell) and HT29 (Homo sapiens colon colorectal adenocarcinoma) cell lines in the manuscript. The chalcone compounds in this study contain morpholine rings in the structure of cancer drugs such as Alectinib, Gefitinib and Canertinib (Figure 1). In addition, these chalcone compounds contain fluorinated organic structures such as 5-Fluorouracil, Floxuridin and Flutamid, which are also used in cancer treatment (Figure 1)

Chalcones consist of aryl rings linking to an α,β -unsaturated ketone group. The easy synthesis of chalcones from various benzaldehyde and acetophenones enables them to be used in drug synthesis. Chalcones possess a number of biological effects such as antimalaria, antibacterial, antiinflammatory and anticancer.¹³

Fluorine atom provides two kinds of biological and chemical effects to the molecule. The organofluorine compounds have some features as shown in Table 1.¹⁴

Table 1. The chemical and biological effects of organofluorine compounds.

Chemical effect	Biological effect
Small size	Electronegativity of neighboring groups
Lipophilic	Strong C-F bonds resistant to metabolic processes
High electronegativity	Increases lipid solubility (bioavailability)
Low reactivity	Synthesis of isosteric analogues of drugs Useful for studying biochemical processes

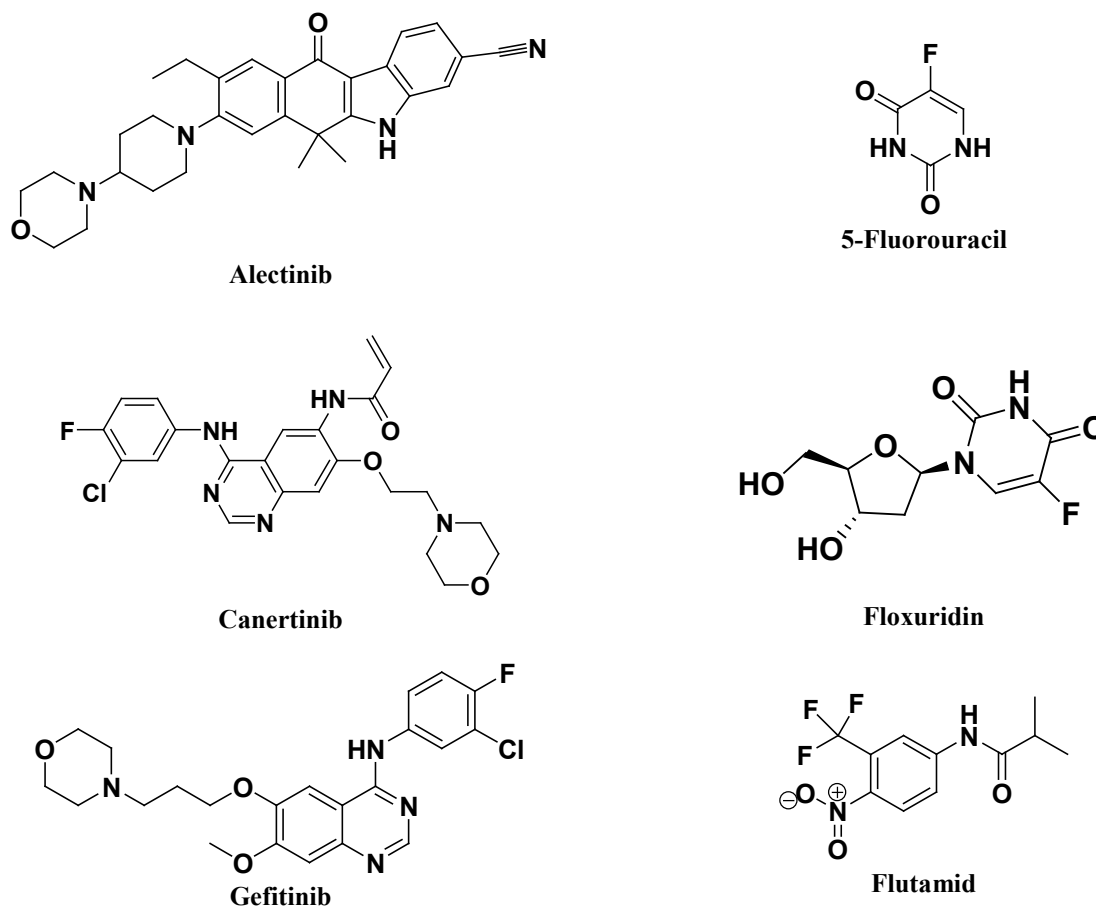


Figure 1. The anticancer drugs

2. MATERIALS AND METHODS

2.1. Preparation of compounds solution

The compounds and 5-Fluorouracil (5-FU) were dissolved in dimethyl sulfoxide (DMSO). The solution was diluted with Dulbecco's Modified Eagle Medium (DMEM). DMSO amount was below 0.1% in the solutions. 5-FU was used as the positive control.

2.2. Anticancer activity method

The tests were carried out on PC3 and HT29. The cells were purchased from the American Type Culture Collection (ATCC) with codes of HT-29 (ATCC® HTB38™) and PC-3 (ATCC® CRL-1435™). The cells were cultured in DMEM (10% of fetal bovine serum (FBS)- 2% of penicillin-streptomycin). DMEM was refreshed once in three days at 37 °C and 5% CO₂ in an incubator. 5-FU was used as the standard drug. The microplate wells were pipetted with 30,000 cells, then incubated for 30 minutes in CO₂ incubator. At the end of 30 h, the wells were added to the sample solutions on four concentrations. Then, the microplates were incubated

overnight in same conditions. The tests were carried out in accordance with the BrdU ELISA kit protocol. Measurements were measured in ELISA reader at 450 nm. The activity was calculated as follows:

$$[1 - (A_{\text{treatments}} / A_{\text{vehicle control}})] \times 100.$$

IC₅₀ was calculated by ED50 plus v1.0, and the results were specified as means ± SD of six values. The statistical analysis was made with SPSS 13.5 (p<0.01).

3. RESULTS AND DISCUSSION

Anticancer effects of all the samples and 5-fluorouracil (5-FU) were determined against HT29 cells at 100, 50, 25 and 5 μM. The IC₅₀ values of all the samples were given at Table 2. The anticancer activities of all the samples were observed as showing dose-dependent increase in activity against HT29 cells (Figure 2). Compound 6 against HT29 cells were determined as having an effect fairly close to 5-FU. However, other compounds have better anticancer activities than 5-FU at high concentrations. The potency of inhibitions (at 100 μM) against HT29 cells were: compound 7 > compound 3 ~ compound 6 > 5-FU > compound 2 > compound 4 ~ compound 1 > compound 4 > compound 5.

Table 2. The IC₅₀ values (μM) of compounds 1-7 against HT29 and PC3 cancer cells

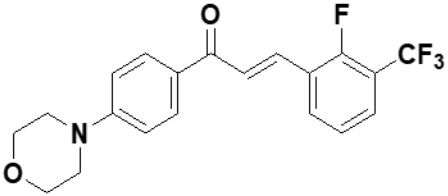
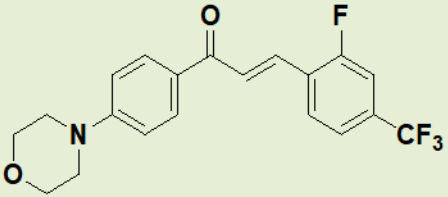
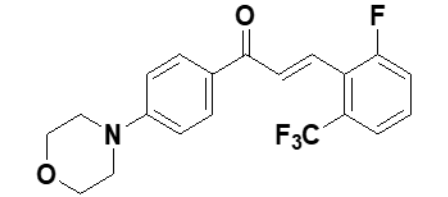
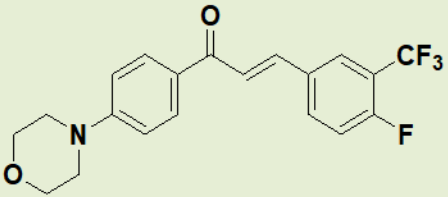
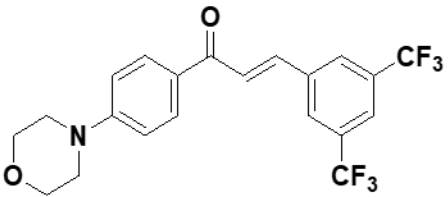
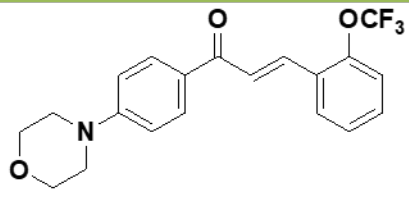
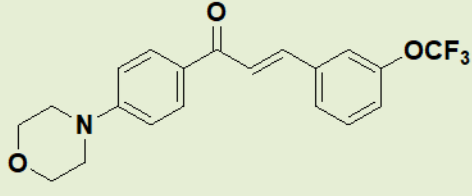
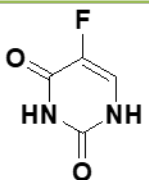
No	Compound structure and name	IC ₅₀	
		HT29	PC3
1	 <p>(<i>E</i>)-3-(2-fluoro-3-(trifluoromethyl)phenyl)-1-(4-morpholinophenyl) prop-2-en-1-one</p>	6.26±0.03	2.53±0.02
2	 <p>(<i>E</i>)-3-(2-fluoro-4-(trifluoromethyl)phenyl)-1-(4-morpholinophenyl) prop-2-en-1-one</p>	5.50±0.02	4.40±0.03
3	 <p>(<i>E</i>)-3-(2-fluoro-6-(trifluoromethyl)phenyl)-1-(4-morpholinophenyl) prop-2-en-1-one</p>	7.03±0.02	5.86±0.02
4	 <p>(<i>E</i>)-3-(4-fluoro-3-(trifluoromethyl)phenyl)-1-(4-morpholinophenyl) prop-2-en-1-one</p>	7.89±0.05	4.36±0.03
5	 <p>(<i>E</i>)-3-(3,5-bis(trifluoromethyl)phenyl)-1-(4-morpholinophenyl) prop-2-en-1-one</p>	3.38±0.01	1.76±0.02

Table 2. Continued

6	 <p>(<i>E</i>)-1-(4-morpholinophenyl)-3-(2-(trifluoromethoxy)phenyl)prop-2-en-1-one</p>	2.11±0.01	1.78±0.03
7	 <p>(<i>E</i>)-1-(4-morpholinophenyl)-3-(3-(trifluoromethoxy)phenyl)prop-2-en-1-one</p>	5.52±0.02	2.31±0.03
5-FU		2.04±0.01	5.69±0.02

against HT29 cell line

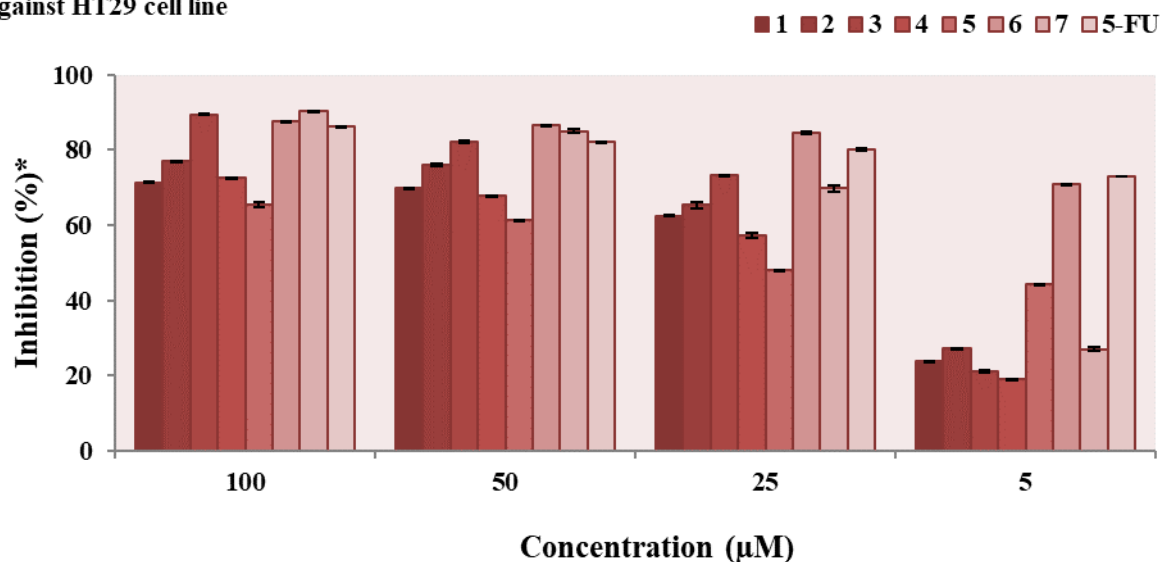


Figure 2. The anticancer activities of all the samples and 5-FU against HT29 cells. * tests were carried out as two experiments with triplicate (n=6; p<0.01).

Anticancer activities of all the samples and 5-FU were determined against PC3 cells at four concentrations (Figure 3). The IC₅₀ values of compounds 1-7 are given at Table 2. The anticancer activities of compounds 1-7 were observed as showing dose-dependent increase in

activity against PC3 cells (Figure 3). All of the compounds (except Compound 3) were determined to have higher anticancer activities compared with 5-FU which was used as the standard compound against PC3 cells. Compound 3 against HT29 cells were determined

to have fairly close to the 5-FU. The potency of inhibitions (at 100 μM) against PC3 cells were: compound 5~ compound 6> compound 7> compound 1> compound 4~ compound 2> 5-FU~ compound 3.

Compound 5 has the highest anticancer activity against PC3 cells (IC_{50} : 1.76 ± 0.02 μM). Compound 5 contains two CF_3 groups. It contains the highest number of CF_3 groups compared to the groups found in other molecules.

The fluorine atom has slightly more lipophilic property than hydrogen. However, trifluoromethyl (CF_3) is much more lipophilic than methyl or chlorine. This property often has the most important role in improving pharmacological activity.¹⁵ This supports the high activity of our compound 5.

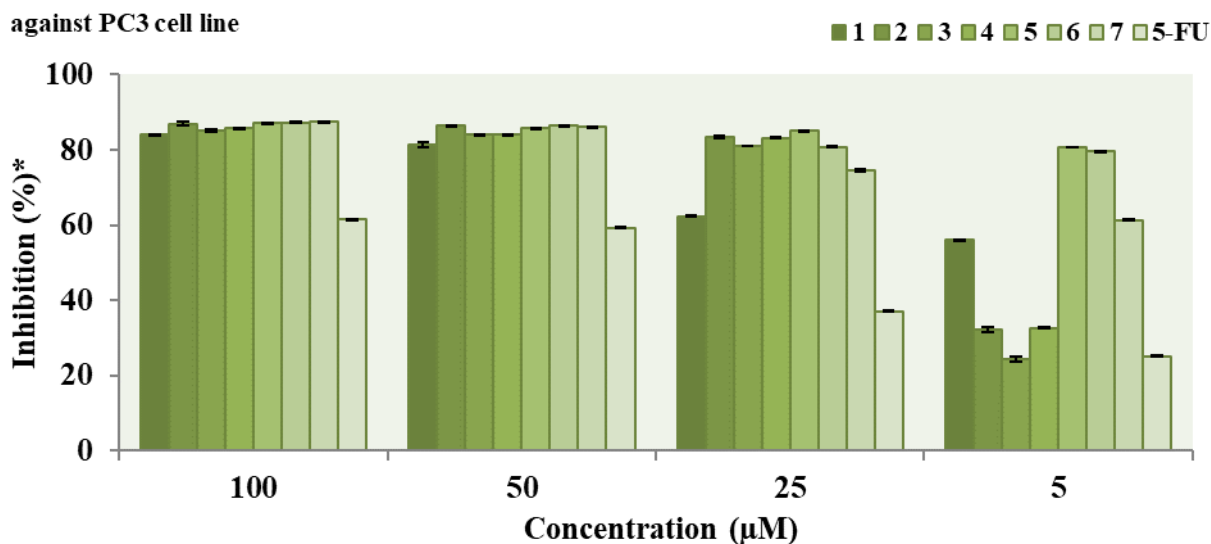


Figure 3. The anticancer activities of all the samples and 5-FU against PC3 cells. * tests were carried out as two experiments with triplicate ($n=6$; $p<0.01$).

The fluorine and trifluoromethyl (electron-withdrawing groups) groups attached to the phenyl ring of chalcone in compound 1 are in position at 2-fluor and 3-trifluoromethyl. The same groups are in position at 2-fluor and 4- trifluoromethyl in compound 2. IC_{50} values for compound 1 and compound 2 against PC3 cells are 2.53 ± 0.02 μM and 4.40 ± 0.03 , respectively. It was seen that the activity against PC3 cancer cells in the 2-3 position was higher than the one in the 2-4 position. F and CF_3 groups are in position at 2-fluor and 6-trifluoromethyl in compound 3, and IC_{50} value of the compound is determined as 5.86 ± 0.02 μM . When the fluorine and trifluoromethyl groups moved away from each other, a decrease in activity, such as compound 3, was detected. The anticancer activities of Compound 1-7 against PC3 were better than the ones against HT29.

The binding of a fluorine atom to a bioactive molecule causes minimal steric changes. Thus, it can facilitate the biomolecule's biological effects such as interaction with enzyme active sites, receptor recognition sites, and biological effects such as transport mechanisms. However, the addition of fluorine significantly changes the physicochemical properties of the bioactive molecule due to its great electronegativity. Therefore, these modified processes can affect biological activity.¹⁶ Bioisosteric derivatives of fluorine instead of the hydrogen atom are to further increase the activity of

biologically active molecules.^{14,17-19} Due to the chemical and biological properties of organofluorine compounds (Table 1), fluorine has become very important for predictions of new drugs and their development.^{15,20-22} Because of this, it affects the number of drugs that contain fluorine in the market today.²³ As in our study, fluorinated chalcone derivatives show anticancer activity.^{13,17,24,25}

4. CONCLUSIONS

Fluorine has chemical and biological properties. Thus it becomes very important for the planning and development of new drugs. Organofluorine structures affect the number of drugs that contain fluorine in the market today. In the study, fluorinated chalcone derivatives especially show higher anticancer activity against PC3 cancer cells compared to 5-FU.

ACKNOWLEDGEMENTS

This study was supported by the Gaziantep University Scientific Research Projects Governing Unit (BAPYB) (Project no: FEF.14.01), Turkey. The authors are also grateful to Esin Ekmekci for the grammatical revision of the manuscript.

Conflict of interests

I declare that there is no a conflict of interest with any person, institute, company, etc.

REFERENCES

1. WHO, 2020. <https://www.drozdogan.com/dunya-kanser-istatistikleri-2020-her-5-kisiden-biri-kanserle-karsilasiyor/> (accessed May 26, 2021).
2. TUIK (Turkey Statistical Institute), 2020. <https://www.drozdogan.com/turkiye-kanser-istatistikleri-2020/> (accessed May 27, 2021).
3. Sung, H.; Ferlay, J.; Siegel, R.L.; Laversanne, M.; Soerjomataram, I.; Jemal, A.; Bray, F. *CA Cancer J. Clin.* **2021**, *71*, 209–24.
4. Yatani, R.; Chigusa, I.; Akazaki, K.; Stemmermann, G.N.; Welsh, R.A.; Correa, P. *Int. J. Cancer.* **1982**, *29*, 611–616.
5. Koivisto, P.; Kolmer, M.; Visakorpi, T.; Kallioniemi, O.P. *Am. J. Pathol.* **1998**, *152*, 1–9.
6. Feldman, B.J.; Feldman, D. *Nat. Rev. Cancer* **2001**, *1*, 34–45.
7. Madhavi, S.; Sreenivasulu, R.; Yazala, J.P. *Saudi Pharm. J.* **2017**, *25*, 275–279.
8. Damyanov, C.; Maslev, I.; Pavlov, V.; Avramov, L. *Ann. Complement. Altern. Med.* **2018**, *1*, 1002.
9. Singh, S.P.; Mishra, A.; Shyanti, R.K.; Singh, R.P.; Acharya, A. *Biol. Trace. Elem. Res.* **2021**, *199*, 1316–1331.
10. Szakacs, G.; Paterson, J.K.; Ludwig, J. A.; Booth-Genthe, C.; Gottesman, M.M. *Nat. Rev. Drug. Discov.* **2006**, *5*, 219–234.
11. Karmous, I.; Pandey, A.; Haj, K.B.; Chaoui, A. *Biol. Trace. Elem. Res.* **2020**, *196*, 330–342.
12. Kursun Aktar, B.S.; Oruç-Emre, E.E.; Demirtas, I.; Sahin Yaglioglu, A.; Guler, C.; Adem, S.; Karaküçük İyidoğan, A. *J. Mol. Struct.* **2017**, *1149*, 632–639.
13. Lawrence, N.J.; Patterson, R.P.; Ooi, L.; Cook, D.; Ducki, S. *Bioorg. Med. Chem. Lett.* **2006**, *16*(22), 5844–5848.
14. Burmaoglu, S.; Algul, O.; Anıl, D.A.; Gobek, A.; Duran, G.G.; Ersan, R.H.; Duran, N. *Bioorg. Med. Chem. Lett.* **2016**, *26*(13), 3172–3176.
15. Filler, R.; Saha, R. *Future Med. Chem.* **2009**, *1*(5), 777–791.
16. Ojima, I. *Chem. Bio. Chem.* **2004**, *5*, 628–635.
17. Padhye, S.; Ahmad, A.; Oswa, N.; Dandawate, P.; Rub, R.A.; Deshpande, J.; Swamy, K.V.; Sarkar, F.H. *Bioorg. Med. Chem. Lett.* **2010**, *20*(19), 5818–5821.
18. Kurun, B.S.; Oruç-Emre, E.E.; Karaküçük-İyidoğan, A.; Sahin Yaglioglu, A.; Tekin, S.; Demirtaş İ. Turkish Patent Institute PATENT No: 2011/05601, 2011.
19. Sun, L.P.; Gao, L.X.; Ma, W.P.; Nan, F.J.; Li, J.; Piao, H.R. *Chem. Biol. Drug. Des.* **2001**, *80*(4), 584–90.
20. Ojima, I. *J. Org. Chem.* **2013**, *78*, 6358–6383.
21. Hagmann, W.K. *J. Med. Chem.* **2008**, *51*, 4359–4369.
22. Isanbor, C.; O'Hagan, D. *J. Fluorine Chem.* **2006**, *127*, 303–319.
23. Abad, A.; Agullo, C.; Cunat, A.C.; Gonzalez-Coloma, A.; Pardo, D. *Eur. J. Org. Chem.* **2010**, *11*, 2182–2198.
24. Nakamura, C.; Kawasaki, N.; Miyataka, H.; Jayachandran, E.; Kim, I. H.; Kirk, K. L. *Bioorg. Med. Chem.* **2002**, *10*(3), 699–706.
25. Lim, Y.H.; Oo, C.W.; Koh, R.Y.; Voon, G.L.; Yew, M.Y.; Yam, M.F.; Loh, Y.C. *Drug. Dev. Res.* **2020**, *81*, 994–1003.



Determination of electronic characteristics of tetrahydro pyrimidine derivatives and investigation of usability as anti-corrosion

Murat OKAY¹, Erdem ERGAN², Begüm Çağla AKBAŞ³, Esvet AKBAŞ^{1,*}

¹Department of Chemistry, Faculty of Science, Van Yuzuncu Yil University, 65080 Van-Turkey

²Department of Property Protection and Security, Van Security Vocational School, Van Yuzuncu Yil University, 65080, Van- Turkey

³ Faculty of Pharmacy, University of Inonu, 44210, Malatya, Turkey

Received: 13 May 2021; Revised: 19 May 2021; Accepted: 07 June 2021

*Corresponding author e-mail: esvakbas@hotmail.com

Citation: Okay, M.; Ergan, E.; Aktaş, B. Ç.; Akbaş, E. *Int. J. Chem. Technol.* 2021, 5 (1), 59-66.

ABSTRACT

Corrosion of metallic structures is a serious problem in most industries worldwide. This problem can be controlled by the addition of chemicals capable of adsorption onto the metal surface. The metal can be isolated from the corrosive environment. These chemicals are often selected from groups containing free electron pairs and / or π electrons, which are rich in functional groups. In this study, electronic structures Highest Molecular Orbital (HOMO), Lowest Occupied Molecular Orbital (LUMO), MEP, energy gap (ΔE), ionization potential (I), electron affinity (A), chemical structure of pyrimidine derivative compounds containing unpaired electron pairs, π electrons, functional groups such as N, O and S hardness and softness (S), general electrophilic index (ω), transmitted electron fraction index (ΔN) and recovery (back-donation) properties of quantum chemical calculation methods to investigate the properties of the selected compounds in this direction and adsorbed to the surface with the quantum chemical calculation methods. The aim of this study is to determine the efficiency of synthesized compounds as anti-corrosion materials and to provide new gains to the industry in this sense.

Keywords: Pyrimidine, DFT, Corrosion, Quantum chemical studies.

Tetrahidro pirimidin türevlerinin elektronik özelliklerinin belirlenmesi ve korozyon önleyici olarak kullanılabilirliğinin araştırılması

Öz

Metalik yapıların korozyonu, dünya çapındaki endüstrilerin çoğunda ciddi bir problemdir. Bu problem, metal yüzey üzerine, adsorpsiyon kabiliyetine sahip kimyasalların ilavesiyle kontrol edilebilir. İlgili kimyasallar sayesinde metal, bulunduğu korozif ortamdan izole edilebilir. Bu kimyasallar çoğunlukla işlevsel grup açısından zengin, serbest elektron çiftleri ve/veya π elektronları içeren gruplardan seçilir. Bu çalışmada yapısında eşleşmemiş elektron çiftleri, π elektronları, N, O ve S gibi fonksiyonel gruplar bulunduran pirimidin türevi bileşiklerin elektronik yapıları en yüksek dolu molekül orbitali (HOMO), en düşük boş molekül orbitali (LUMO), MEP, enerji gap (ΔE), iyonizasyon potansiyeli (I), elektron afinitesi (A), kimyasal sertlik ve yumuşaklığı (S), genel elektrofilik indeksi (ω), iletilen elektron fraksiyon indeksi (ΔN) ve geri kazanım ($\Delta E_{\text{back-donation}}$) özelliklerinin kuantum kimyasal hesaplama yöntemleri ile incelenmesi amaçlanmış ve bu doğrultuda seçilen bileşiklerin kuantum kimyasal hesaplama yöntemleri ile demir yüzeyine adsorbe olma yetenekleri ve korozyon önleyici etkileri çalışılmıştır. Bu çalışma ile sentezlenmiş bileşiklerin anti-korozyon malzeme olarak kullanım verimliliği tespit edilerek bu anlamda endüstriye yeni kazanımlar sağlanması hedeflenmiştir.

Anahtar Kelimeler: DFT, Elektronik özellikler, Korozyon, Pirimidin.

1. INTRODUCTION

Corrosion is the deterioration of metal by reacting with chemicals or the environment. Corrosive solutions are

used in many industrial applications. Acid solutions widely used in industry, especially in cleaning process causes significant mass loss on the surface.¹⁻³ There are very different techniques used to intercept corrosion. One

of the techniques of preventing corrosion is to use protective materials. Organic compounds are also one of the important materials used as protective materials. The organic compounds show high inhibition property when containing aromatic rings, heteroatoms and π electrons.⁴⁻⁸ Generally, inhibition between heteroatoms increases in the O < N < S sequence.^{9,10} Heteroatoms and π -bonds are capable of forming coordinate covalent bond with metal surface and thus exhibit excellent inhibitory properties.¹¹

It is preferred that the compounds used for corrosion inhibiting purpose are not harmful to nature. For this reason, pyrimidine derivatives have attracted great attention due to their less environmentally damaging properties.¹² Pyrimidine derivatives exhibit wide biochemical effects due to the activity of aromatic ring system, N atoms and π electrons.¹³ Due to these properties, pyrimidine compounds are promising for corrosion inhibition.^{14,15}

Many different methods are used in the development of corrosion inhibitors. Most of these methods are based on expensive experimental methods such as weight-loss, electrochemical impedance (*EI*), potentiodynamic polarization, etc.^{16,17} Although experiments mostly are time-consuming, costly, and lacking in explaining the mechanism of inhibition of the corrosion.^{18,19} Recently, it has been used frequently in computational methods as an alternative to expensive and time, consuming experimental methods. The quantum chemical calculation (QCC) method is one of these computational methods. This method was endorsed as a potent and easy tool to reduce the cost and time and can help in the interpretation of the experimental findings.^{20,21}

Heakal et al.²² used QCCs to determine the structural and electronic properties of imidazole-pyrimidine-based new ionic compounds. They compared the theoretical inhibition yields of the compounds prepared in this way. Molecules chosen as inhibitors must be capable of donating electrons to the empty *d*-orbital of the metal and also be suitable for forming anti-feedback bonds. Pyrimidine compounds have these properties. Therefore, these molecules are waited to be perfect corrosion inhibitors at industrial level.²³

The inhibition effect of the molecule is mostly related to the electronic structure of the compounds. QCC is widely used to find the electronic properties of compounds. According to the frontier orbital theory, the reaction is due to an interaction between the Highest Molecular Orbital (HOMO) and Lowest Occupied Molecular Orbital (LUMO) boundary orbits of the compounds. Therefore, correct interpretation of these energy levels is important to understand the inhibition effect. To understand the mechanism, it must be calculated in the energy gap (ΔE). The energy gap equals the difference

between E_{LUMO} and E_{HOMO} energies. Low values of ΔE will provide perfect inhibition effect.

In order to determine the ability of the molecule to prevent corrosion that may occur on the metal surface, the absolute *I*, *A*, *S*, ω , ΔN and $\Delta E_{back-donation}$ properties must be calculated. In this study, all these calculations were carried out according to Shojaie *et al.*²⁴ using Gaussian09.6²⁵⁻²⁹

2. MATERIALS AND METHODS

In this study, Gaussian 09 package program was used. The Gaussian 09 program is a product of the Gauss series. Gauss is the most widely used program for theoretical and density functional calculations and can also perform semi-empirical calculations. The first version of Gauss appeared in 1970 and Gaussian 09 appeared in 2009. It was developed by Gauss, John Pople et al, and has had a significant impact on the increasing use of QCCs by chemists. It is an easy to use program that allows many calculations that can be done with almost any quantum-mechanical method available.

Based on the fundamental laws of quantum mechanics, Gaussian09 enables us to predict the molecular properties, molecular structures, vibrational frequencies of compounds and reactions in a wide variety of chemical environments.

To find the optimum geometry theoretically, the molecular wave function and electronic energy are calculated for many different configurations of nuclei by varying bond lengths, bond angles and dihedral angles to find the minimum energy sequence. The geometric optimization calculation continues until the magnitude of the gradient is close to zero, indicating the presence of an energy minimum. In the vibration frequency calculation, the program calculates the molecular vibration frequencies. The vibration frequency calculation should follow the geometry optimization. Because it is unnecessary to calculate vibration frequency for a geometry where energy is not at minimum.

As the geometric optimization calculations of large molecules are made with high level methods, they are very time consuming processes. Large molecules can have a large number of conformers whose global minimum and energies make it difficult to find local minimums as low as fairly large molecules can have. There are many special methods for conformational scanning whose aim is to find the low energy conformer. Due to the large number of conformers in question, energy calculations in conformational scanning with large molecules are usually made by molecular mechanics.

In this work, the potentials of pyrimidine derivatives as corrosion inhibitors were calculated by density functional

theory (DFT) at the B3LYP / 6-31G (d, p) level using the Gaussian package program.

The aim of this study is to determine the efficiency of pyrimidine compounds as anti-corrosion materials and to provide new gains to the industry in this sense. For this purpose, the electronic structures; HOMO, LUMO, MEP, ΔE , I and A chemical structure of pyrimidine derivative compounds containing unpaired electron pairs, π electrons, functional groups such as N, O and S hardness and softness (S), general electrophilic index (ω), transmitted electron fraction index (ΔN) and recovery (backEback-donation) properties investigate the

properties of the selected compounds in this direction and adsorbed to the surface with the quantum chemical calculation methods.

3. RESULTS AND DISCUSSION

In this work, geometric optimizations and quantum chemical parameters used to determine their corrosion inhibition potential of previously synthesized pyrimidine compounds³⁰ (Figure 1) has been studied by DFT calculations

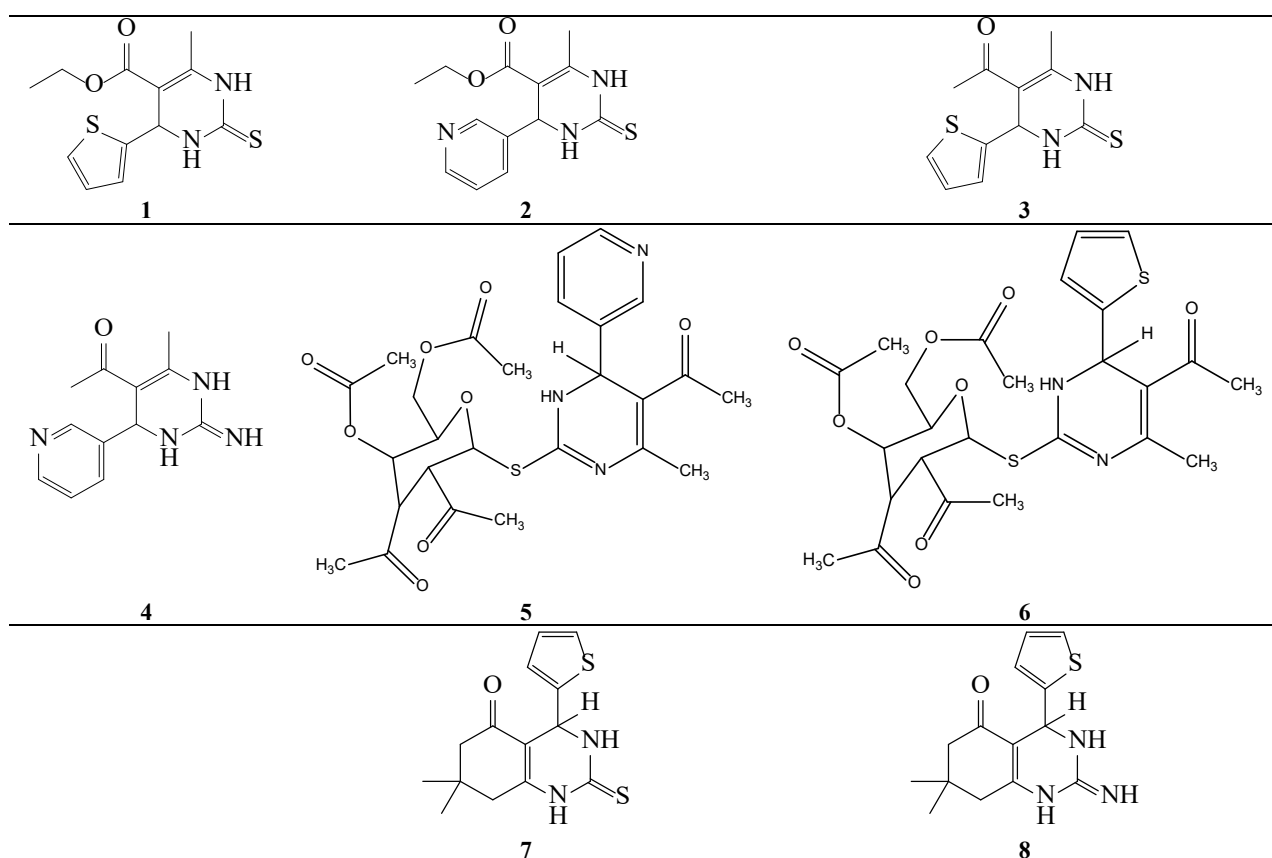


Figure 1. Molecular structures and schematic representation of pyrimidine derivatives

Theoretical calculations led to the development of experimental work. With theoretical calculations, corrosion activity parameters of the analyzed molecules against metal atoms can be calculated. Theoretical calculations have demonstrated that the molecule's filled highest energy orbital and empty lowest energy orbital values are the most important parameters in estimating the corrosion inhibition activity of the molecules against metal atoms. It can be found that molecules for which quantum chemical calculations are made are active molecules with parameters like E_{HOMO} , E_{LUMO} , ΔE , χ , μ , η , ω , σ .³¹

$$\mu = -\chi = \left(\frac{\partial E}{\partial N} \right)_{\theta(r)} \quad (1)$$

$$\eta = \frac{1}{2} \left(\frac{\partial^2 E}{\partial N^2} \right)_{\theta(r)} = \frac{1}{2} \left(\frac{\partial \mu}{\partial N} \right) \quad (2)$$

The I, A, χ , σ , η values of the studied molecules are obtained by E_{HOMO} and E_{LUMO} with the following equations are obtained:³²

$$\chi = -\mu = \left(\frac{-E_{\text{HOMO}} - E_{\text{LUMO}}}{2} \right) = \left(\frac{I+A}{2} \right) \quad (3)$$

$$\eta = \left(\frac{E_{\text{LUMO}} - E_{\text{HOMO}}}{2} \right) = \left(\frac{I-A}{2} \right) \quad (4)$$

σ is a chemical illustrator that surveys molecular stability and reactivity. σ is defined as the reverse of η .³³

$$\sigma = \frac{1}{\eta} \quad (5)$$

The ω is a survey of the energy drop because of the maximum electron run between donor and acceptor. It can be represented as a function of χ and η as shown in Eq. (6).³⁴

$$\omega = \frac{\mu^2}{2\eta} = \frac{\chi^2}{2\eta} \quad (6)$$

The ω surveys the ability of molecules to receive electrons. As the ω value of a molecule increases, its electrophilic character increases, and as it decreases, its nucleophilic character increases.

The electronegativity value of molecules is a parameter that helps to compare the reactivity of molecules. The value of this parameter is given to estimate the electron transfer between metal and inhibitor. The molecule with a high electronegativity value hardly gives any valence electrons to this molecule. Because these electrons are attracted to the nucleus more than other molecules. According to Sanderson's electronegativity equation,^{35,36} we calculate the value of the electrons transferred from the anti-corrosion molecule with the following equation.

$$\Delta N = \frac{\chi_M - \chi_{inh}}{2(\eta_M + \eta_{inh})} \quad (7)$$

Here χ_M and χ_{inh} are the electronegativity value of the metal and the inhibitor molecule, respectively. η_M and η_{inh} are the chemical hardness of the metal and the inhibitor molecule, respectively.

According to the simple charge transfer model, the electron donation and recovery process can be expressed as an electronic donation back process between the inhibitor molecule and the metal surface.³⁷

$$\Delta E_{back\ donation} = -\frac{\eta}{4} \quad (8)$$

The $\Delta E_{back\ donation}$ implies that When $\eta > 0$ and $\Delta E_{back\ donation} < 0$ the charge transfer to a molecule, followed by a back donation from the molecule, is energetically favored.

Fully geometric optimizations of all molecules, HOMO-LUMO diagrams, molecular electrostatic potential maps (MEPs) and corrosion inhibition parameters were calculated with DFT and B3LYP (d, p) base set in Gaussian09 program (Figure 2 and Table 1).

It has been determined in some studies that this calculation method, which is carried out theoretically, is used to examine the relationship between corrosion inhibition efficiency and electronic properties of molecules.³⁸

MEPs that provide information about the molecular distribution of electrons are represented by different colors. In Figure 1, the negative (red) areas are associated with electrophilic reactivity and positive (blue) areas with nucleophilic reactivity. Electrostatic potential increases during red > orange > yellow > green > blue. The highest potential is on oxygen atoms.³⁹

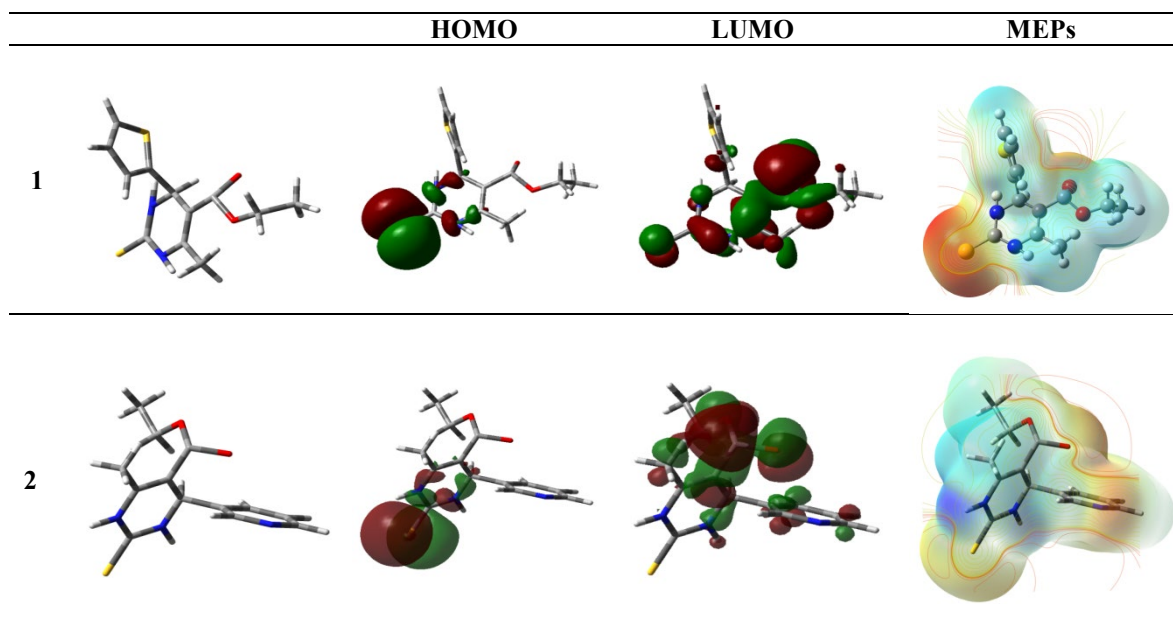


Figure 2. Structures, HOMO-LUMO diagrams and MEPs of optimized pyrimidine molecules

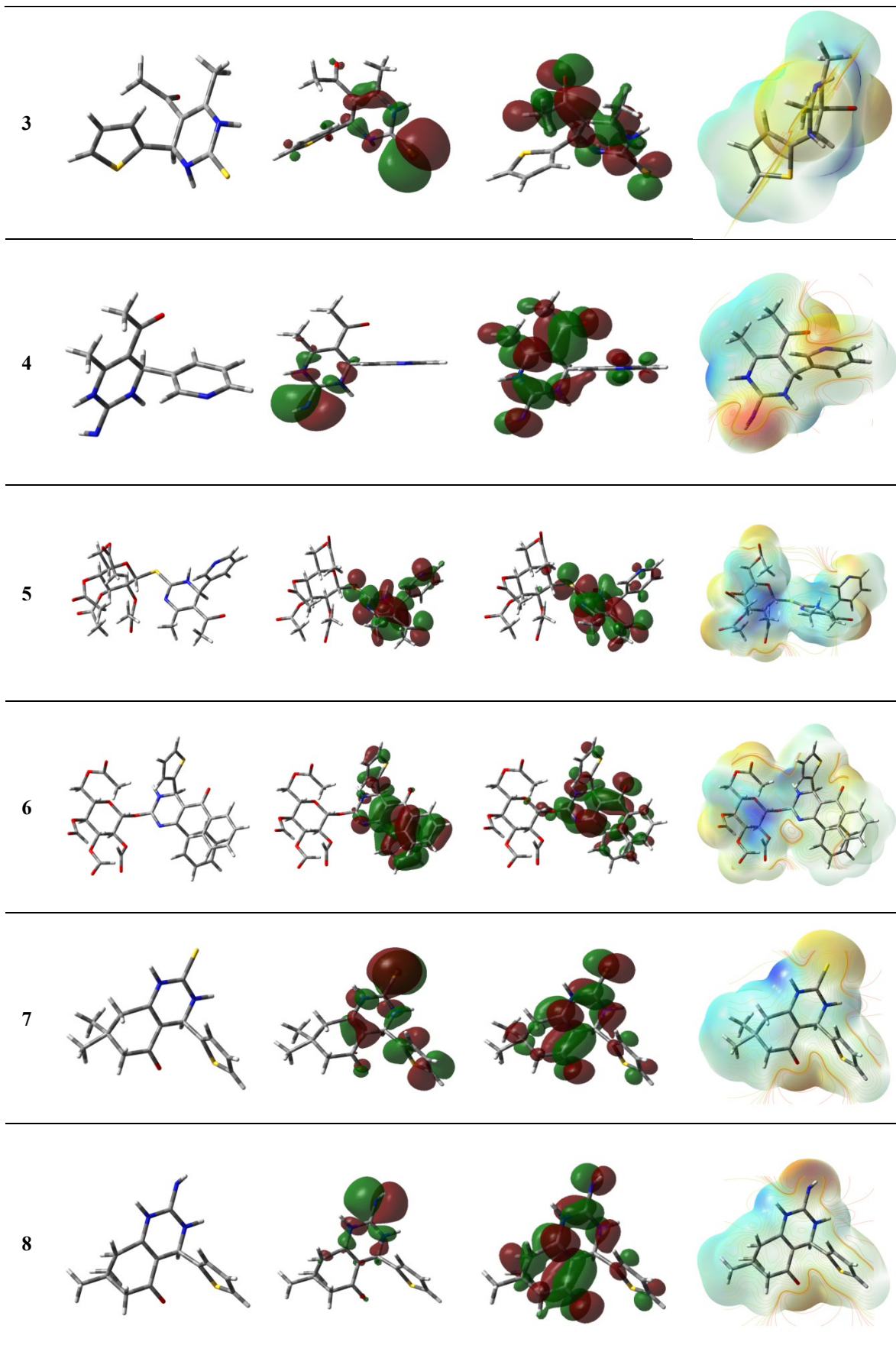


Figure 2. Continued

Table 1. Calculated quantum chemical parameters of the studied molecules in gas phase (eV)

Compound	E _{HOMO}	E _{LUMO}	ΔE	I	A	η
1	-5.2995	-3.2518	2.0477	5.2995	3.2518	2.0477
2	-5.8046	-3.4603	2.3443	5.8046	3.4603	2.3443
3	-5.8174	-2.2074	3.6099	5.8174	2.2074	3.6100
4	-4.5629	-1.7851	2.7478	4.5629	1.7851	2.7778
5	-6.1366	-2.8254	3.3112	6.1366	2.8254	3.3112
6	-5.7711	-2.9677	2.8034	5.7711	2.9677	2.8034
7	-5.6549	-1.8795	3.7754	5.6549	1.8795	3.7754
8	-4.3874	-1.6131	2.7743	4.3874	1.6131	2.7743

Compound	S	χ	μ	ω	ΔN	ΔE _{back-donation}
1	0.4884	6.9254	7.7544	14.6825	0.0182	-0.5119
2	0.4266	7.5347	4.4066	4.1416	-0.1140	-0.5860
3	0.2770	6.9211	3.6135	1.8085	0.0109	-0.9025
4	0.3599	6.4555	4.6522	3.8957	0.0980	-0.6944
5	0.3020	7.5493	3.1698	1.5172	-0.0829	-0.8278
6	0.3567	7.2549	4.9994	4.4578	-0.0454	-0.7008
7	0.2648	6.5946	5.3217	3.7506	0.0536	-0.94385
8	0.3605	5.1939	5.0076	4.5193	0.3255	-0.6935

The chemical reactivity properties of the inhibitor molecule depend on the interaction between HOMO and LUMO orbitals. The energy level of HOMO is defined as the skill of a molecule to donate electrons. Therefore, the molecule with a higher E_{HOMO} value shows a better tendency to electron donation and increases the adsorption on the metal. Therefore, it provides better inhibition efficiency. The LUMO energy level of molecules is the molecule's ability to accept electrons. When the LUMO energy level of the inhibitor molecule is lower, it is capable of accepting more electrons. The skill of the inhibitor to bind to the metal surface increases with increasing HOMO energy values and decreasing LUMO energy values.

The energy gap (ΔE_{gap}) between the E_{HOMO} and E_{LUMO} energy levels of molecules is one of the most important parameters used to determine the reactivity of the inhibitor molecule. The energy gap value (ΔE_{gap}) of the inhibitor molecule indicates its ability to bind to the metal surface. The term chemical hardness (η) is used against electron cloud polarization and chemical degradation. Chemical hardness (η) is an important parameter investigating the reactivity of molecules in experimental and theoretical chemistry. Global softness (σ), ΔE_{gap} and chemical hardness are interrelated. The chemical hardness, global softness values of the Koopman theory⁴⁰ replaced the HOMO and LUMO energy values. If hard molecules have a high ΔE_{gap} value, this molecule is not a good corrosion inhibitor. Therefore, this molecule cannot easily donate HOMO's electron to metal. The global electrophilic index (ω) surveys the ability of molecules to receive electrons. As the ω value of a molecule increases, its electrophilic character increases, and as it decreases, its nucleophilic character increases. If the transferred electron (ΔN) is < 3.6, it helps to increase the inhibitory efficiency by increasing the skill of these inhibitors to donate electrons to the metal surface. The highest electron fraction is connected with the best inhibitor. In

the light of this information it can be said that the compounds **1** and **2** may have high inhibition potential.

CONCLUSIONS

In this study, quantum chemical calculations of previously synthesized pyrimidine compounds³⁰ were studied. The electronic properties of the molecules, corrosion prevention parameters and electrostatic potential maps (MEP) properties were theoretically calculated on the DFT-B3LYP / 6-31 G (d, p) base set. As a result, it was determined that compound **1,2** is theoretically the most active structure in terms of corrosion prevention potential.

ACKNOWLEDGEMENTS

This work was supported by the Van Yuzuncu Yil University of Turkey FYL-2019-8386

Conflict of interests

Authors declare that there is no a conflict of interest with any person, institute, company, etc.

REFERENCES

- Lagrene, M.; Mernari, B.; Bouanis, M.; Traisnel, M. and Bentiss, F. *Corrosion Sci.* **2002**, 44, 573-79.
- Yurt, A.; Ulutas, S.; Dal, H. *App. Surface Sci.* **2006**, 253, 919-22.
- Şafak, S.; Duran, B.; Yurt, A.; Türkoğlu, G. *Corrosion Sci.* **2012**, 54, 25-29.
- Shahabi, S.; Norouzi, P.; Ganjali, M. R. *Int. J. Electrochem Sci.* **2015**, 10, 2646-50.

5. Abd El-Maksoud, S.A. *Appl. Surf. Sci.*, **2003**, 206, 129-133.
6. Lopez-Sesenes, R.; Gonzalez-Rodriguez, J.G.; Casales, M.; Martinez, L.; Sanchez-Ghenno, J.C. *Int. J. Electrochem. Sci.*, **2011**, 6, 1772-1784.
7. Aljourani, J.; Golozar, M.A.; Raieisi, K. *Mater. Chem. Phys.* **2010**, 121 (1,2), 320-325.
8. Abboud, Y.; Abourriche, A.; Saffaj, T.; Berrada, M.; Charrouf, M.; Bennamara, A.; Al Himidi, N.; Abd El-Maksoud, S.A.; Fouda, A.S. *Mater. Chem. Phys.*, **2005**, 93, 84.
9. Awad, H.S.; Gawad, S.A. *AntiCorros. Method Mater.*, **2005**, 52, 328.
10. Chetouani, A.; Aouniti, A.; Hammouti, B.; Benchat, N.; Benhadda, T.; Kertit, S. *Corros. Sci.*, **2003**, 45, 1675- 1684.
11. Loto, R. T.; Loto, C. A.; Popoola, A. P. I.; Ranyaoa, M. *International Journal of the Physical Sciences*, **2012**, 7(19), 2697- 2705.
12. Rasheeda, K.; Alva, V. D. P.; Krishnaprasad, P. A.; Samshuddin, S. *Int. J. Corros. Scale Inhib.* **2018**, 7, 48.
13. Dansena, H.; Dhongade, H. J.; Chandrakar, K. *Asian J. Pharm. Clin. Res.* **2015**, 8, 171.
14. Selvam. T. P.; James, C. R.; Dniandev, P. V.; Valzita, S. K. *Research in Pharm.* **2012**, 2, 01.
15. Abdallah, M.; Helal, E.A.; Fouda, A.S. *Corr. Sci.*, **2006**, 48 (7), 1639-1654.
16. Zhang, D.Q.; Cai, Q. R.; He, X. M.; Gao, L. X.; Zhou, G. D. *Materials Chemistry and Physics.* **2008**, 112(2), 353-8.
17. Amin, M.A.; Ibrahim, M.M. *Corrosion Science.* **2011**, 53(3), 873-85.
18. Wazzan, N.A.; Obot, I.; Kaya, S. *Journal of Molecular Liquids.* **2016**, 221, 579-602.
19. Usman, B.; Jimoh, I.; Umar, B. A. *Applied Journal of Environmental Engineering Science.* **2019**, 5(1), 66-74.
20. Atalay, Y.; Yakuphanoglu, F.; Sekerci, M.; Avci, D.; Başoğlu, A. *Spectrochimica Acta Part A: Molecular and Biomolecular Spectroscopy.* **2006**, 64(1), 68-72.
21. Ebenso, E.E.; Arslan, T.; Kandemirli, F.; Caner, N.; Love, I. *International Journal of Quantum Chemistry.* **2010**, 110(5), 1003-18.
22. Heakal, F. E. T.; Rizk, S. A. and Elkholy, A. E. *Journal of Molecular Structure*, **2018**, 1152, 328.
23. Akbas, E.; Yildiz, E.; Erdogan, A. *Journal of the Serbian Chemical Society*, **2020**, 85, 481.
24. Shojaie F., Mirzai-Baghini, N. *International Journal of Industrial Chemistry*, **2015**, 6, 297-310.
25. Frisch, M. J.; Trucks, G. W.; Schlegel, H. B.; Scuseria, G. E.; Robb, M. A.; Cheeseman, J. R.; Scalmani, G.; Barone, V.; Mennucci, B.; Petersson, G. A.; Nakatsuji, H.; Caricato, M.; Li, X.; Hratchian, H. P.; Izmaylov, A. F.; Bloino, J.; Zheng, G.; Sonnenberg, J. L.; Hada, M.; Ehara, M.; Toyota, K.; Fukuda, R.; Hasegawa, J.; Ishida, M.; Nakajima, T.; Honda, Y.; Kitao, O.; Nakai, H.; Vreven, T.; Montgomery, J. A.; Peralta, Jr. J. E.; Ogliaro, F.; Bearpark, M.; Heyd, J. J.; Brothers, E.; Kudin, K. N.; Staroverov, V. N.; Kobayashi, R.; Normand, J.; Raghavachari, K.; Rendell, A.; Burant, J. C.; Iyengar, S. S.; Tomasi, J.; Cossi, M.; Rega, N.; Millam, J. M.; Klene, M.; Knox, J. E.; Cross, J. B.; Bakken, V.; Adamo, C.; Jaramillo, J.; Gomperts, R.; Stratmann, R. E.; Yazyev, O.; Austin, A. J.; Cammi, R.; Pomelli, C.; Ochterski, J. W.; Martin, R. L.; Morokuma, K.; Zakrzewski, V. G.; Voth, G. A.; Salvador, P.; Dannenberg, J. J.; Dapprich, S.; Daniels, A.D.; Farkas, Ö.; Foresman, J. B.; Ortiz, J. V.; Cioslowski, J. and Fox, D. J. Gaussian, Inc., Wallingford CT, **2009**.
26. Lee, C.; Yang, W.; Parr, R. G. *Phys. Rev. B* **1988**, 37, 785.
27. Becke, A. D. *J. Chem. Phys.* **1993**, 98, 1372.
28. Parr, R. G.; Szentpaly, L. *J. Am. Chem. Soc.* **1999**, 121, 1922.
29. Becke, A. D. *J. Chem. Phys.* **1992**, 96, 2155.
30. Salem, M. A.; Behalo, M. S.; Elrazaz, E. *Medicinal Chemistry Research*, **2019**, 28, 1223–1234.
31. Ergan, E.; Akbas, E. *Fresenius Environmental Bulletin*, **2018**, 27(12B), 9549-9556.
32. Brus, L.E. *J Chem Phys.*, **1983**, 79, 5566–5571.
33. Chattaraj, P.K.; Sarkar, U.; Roy, D.R. *Electrophilicity Index. Chemical Reviews.* **2006**, 106, 2065.
34. Parr, R.G.; Yang, W. Oxford University Press, Oxford, 1989.

35. Sanderson, R.T. Chemical bond and bond energy, Academic Press, New York, 1976.
36. Sanderson, R.T. *J. Chem. Educ.*, **1954**, 31, 2-7.
37. Ramírez-Ramírez, J.Z.; Rubicelia Vargas, R.; Garza, J.; Gázquez, J.L. *The Journal of Physical Chemistry A*. **2010**, 114(30), 7945.
38. Young, D.C. A practical guide for applying techniques to real world problems in Computational Chemistry. New York: John Wiley and Sons Inc. 2001, pp 630-38.
39. Zhang, Z.; Li, W.; Zhang, W.; Huang, X.; Ruan, L.; Wu, L. *Journal of Molecular Liquids*, **2018**, 272, 528-538.
40. Koopmans, T. *Physica*, **1993**, 1, 104-113.



Comparison of the chemical composition and bioactive properties of extracts prepared from the mature Turkish and Brazilian banana peels

Tefvik ÖZEN^{1,*}, İbrahim DEMİRTAŞ²

¹Department of Chemistry, Faculty of Arts and Sciences, Ondokuz Mayıs University, 55139, Samsun, Turkey

² Department of Chemistry, Faculty of Arts and Sciences, Iğdir University, 76000, Iğdir, Turkey

Received: 13 May 2021; Revised: 13 June 2021; Accepted: 13 June 2021

*Corresponding author e-mail: tevfikoz@omu.edu.tr

Citation: Özen, T.; Demirtaş, İ. *Int. J. Chem. Technol.* 2021, 5 (1), 67-76.

ABSTRACT

The banana (*Musa sp.*) plant grows in tropical and subtropical regions. The fruit of the banana is eaten and the peel of the banana is discarded. In this study, chemical analyzes (HPLC-TOF/MS ve GC-MS) and biochemical activities (antioxidant and antimicrobial) of ethyl acetate (Ea) and methanol/chloroform (Me/Ch) extracts prepared from banana peel (Bbp) grown in Brazil and banana peel (Tbp) grown in Turkey were investigated. Cetene, 4-hydroxybenzoic, palmitic, linoleic, stearic, gentisic and syringic acid are the most abundant compounds in the extracts. The total antioxidant activity of Tbp-Ea ($A_{0.5}$: 36.84 $\mu\text{g/mL}$), inhibition of lipid peroxidation of Bbp-Ea (IC_{50} : 3.22 $\mu\text{g/mL}$), reducing power of Tbp-Me/Ch ($A_{0.5}$: 4.96 $\mu\text{g/mL}$), DPPH^{*} scavenging activity of Bbp-Ea (IC_{50} : 8.54 $\mu\text{g/mL}$), metal chelating activity of Tbp-Ea (IC_{50} : 16.54 $\mu\text{g/mL}$) and H_2O_2 scavenging activity of Tbp-Me/Ch (IC_{50} : 0.36 $\mu\text{g/mL}$) were found the most effective. It was exhibited that extracts were effective against gram-negative and gram-positive bacteria. In conclusion, the phytochemical and biochemical results of the Tbp and Bbp extracts will contribute further pharmacological, biochemical and pharmacological investigations.

Key Words: Banana (*Musa sp.*) peel extract, polyphenolics, fatty acids, volatile compounds, bioactivity.

1. INTRODUCTION

Polyphenolics are the most common secondary metabolites in plants and contain at least one aromatic ring. Phenolics form different chemical structures with the hydroxyl group of carbohydrates, lipids, organic acids, amines and cell wall components. Due to their natural antimicrobial and antioxidant bioavailability,

Olgun Türk ve Brezilya muz kabuklarından hazırlanan ekstraktların kimyasal bileşimi ve biyoaktivite özelliklerinin karşılaştırılması

ÖZ

Muz (*Musa sp.*) bitkisi tropikal ve subtropikal bölgelerde yetişir. Muzun meyvesi yenir ve kabuğu atılır. Bu çalışmada Brezilya' da yetişen muz kabuğu (Bbp) ve Türkiye' de yetişen muz kabuğundan (Tbp) hazırlanan etil asetat (Ea) ve metanol/kloroform (Me/Ch) ekstraktlarının kimyasal analizleri (HPLC-TOF/MS ve GC-MS) ve biyokimyasal aktiviteleri (antioksidan ve antimikrobiyal) araştırıldı. Seten, 4-hidroksibenzoik, palmitik, linoleik, stearik, gentisik ve siringik asit ekstraktlarda en bol bulunan bileşiklerdir. Tbp-Ea'nın toplam antioksidan aktivitesi ($A_{0.5}$:36.84 $\mu\text{g/mL}$), Bbp-Ea'nın lipid peroksidasyonunun inhibisyonu (IC_{50} : 3.22 $\mu\text{g/mL}$), Tbp-Me/Ch'nin gücünü azaltma ($A_{0.5}$:4.96 $\mu\text{g/mL}$), Bbp-Ea'nın DPPH^{*} temizleme aktivitesi (IC_{50} : 8.54 $\mu\text{g/mL}$), Tbp-Ea'nın metal şelatlama aktivitesi (IC_{50} : 16.54 $\mu\text{g/mL}$) ve Tbp-Me/Ch'nin H_2O_2 temizleme aktivitesi (IC_{50} : 0.36 $\mu\text{g/mL}$) en etkili bulundu. Ekstraktların gram negatif ve gram pozitif bakterilere karşı etkililiğini gösterdi. Sonuç olarak, Tbp ve Bbp ekstraktlarının fitokimyasal ve biyokimyasal sonuçları daha ileri farmakolojik, biyokimyasal ve farmakolojik araştırmalara katkı sağlayacaktır.

Anahtar Kelimeler: Muz (*Musa sp.*) kabuğu ekstresi, polifenolikler, yağ asitleri, uçucu bileşikler, biyoaktivite.

phenolic compounds in polymeric formulations present a wide range of applications in the fields of food, health and biotechnology. Consumption of products with high polyphenolics sources can slow, prevent or completely reverse the development of neurological cancer and cardiovascular diseases. Research of high polyphenolic content plants with the reuse of industrial fruit and vegetable wastes has increased the interest of researchers

in the processing of vegetables and fruits.¹ Research on the reuse of industrial fruit and vegetable debris containing high polyphenols has increased the interest of researchers in the recovery of by-products obtained during the processing stages of fruits and vegetables.² Banana (*Musa sp.*) is one of the most consumed fresh and processed tropical fruits in the world due to its high vitamin, mineral, nutritional value and also low cost.³ Bananas are freshly consumed or processed to dry fruit ice-cream, jam and nectar to prepare functional foods, while peels constituting approximately 38% of fruit-weight are considered waste.^{4,5} It was recorded that the peels are a waste product containing high dietary fibre and polyphenolic, and also have a strong antioxidant feature.⁶⁻⁸ Recently, scientists have been in a lot of work to improve the nutritional value of food products and to reveal the value of food waste products.^{9,10} Banana peels are large quantities annually, evidenced by household, market, restaurant and food processing waste. The disposal of banana peel is a major concern, but in recent research, it has been suggested that banana peel is a source of important bioactive compounds.¹¹ 1 ton dry banana peel is presented as a material balance for based on the valorization biorefinery and the results exhibit that protein (432 kg), citric acid (170 kg), ethanol (325 m³) and methane (220 m³) can be produced.¹² Banana peel has been used in different industrial field trials of organic fertilizer and refining agent. Gusmavartati et al. (2015) compared the banana peel and other organic natural product wastes in terms of carbon and nitrogen contents and reached very high results (C, 37.99% and %N, 1.37%). In addition, in this study, they obtained a very high yield of organic fertilizer by mixing with banana shells, house market and restaurant wastes at certain ratios.¹³ Bp was determined to be a good absorbent for Cr(VI) ions in industrial wastewater.¹⁴

The climatic and geographical conditions of Turkey are suitable for growing bananas in the microclimate areas of the Mediterranean and Aegean regions as an agricultural product, and greenhouse cultivation is carried out. Imported bananas are preferred due to the size, colour difference and short shelf life of the banana grown in Turkey. However, Turkish people are highly preferred and consumed in the domestic market. In the literature, there are researches on the use of banana peel in different application areas. Although there are limited studies in the literature about Turkish banana, there is no research on the peel of Turkish banana. Thus, by comparing the phytochemical and bioactivities of the domestic and imported banana peel extracts, the content and activity of the domestic banana peels were revealed. In this work chemical contents of the ethyl acetate (Ea) and MeOH/CHCl₃ (Me/Ch) extracts of mature Turkish banana peel (Tbp) and mature Brazilian banana peel (Bbp) were analyzed with HPLC-TOF/MS and GC-MS, and their bioactivities were performed with antioxidant and antimicrobial tests.

2. MATERIALS AND METHODS

2.1. Chemicals

The ethyl acetate, methanol, chloroform, hexane are HPLC grade solvents and were purchased from Merck. Ammonium molybdate, sodium phosphate, K₃Fe(CN)₆, trichloroacetic acid, K₂HPO₄, KH₂PO₄, NADH (nicotinamide adenine dinucleotide), NBT (nitroblue tetrazolium), PMS (ferrozine meta sulphate), FeCl₃ and DPPH· (2,2-diphenyl-1-picrylhydrazyl) were provided from Sigma. The other chemicals were purchased from local commercial sellers.

2.2. Sample

The mature Turkish (Tb) and Brazilian bananas (Bb) were purchased from the market. They were peeled and then their peels were dried in a dry and dark place at room temperature.

2.3. Extraction and phytochemical analysis

The dried Tb and Bb peels were extracted at room temperature and macerated with 10 g of banana peel MeOH/CHCl₃ (1:1) solvent mixture in a closed container and the dark.¹⁵ At the end of the extraction period, the remains were filtered. Solvents of the extracts were removed in a vacuum on a rotary evaporator. Quantitative analysis and phytochemical content experiments were carried out with these extracted extracts. For GC-MS analyzes, the derivatization of the alcohols in the form of methoxy was carried out. The dried banana peel was added with a sufficient amount of purified water and subjected to boiling. After boiling, the extract was filtered with ordinary filter paper. The solvent mixture MeOH/CHCl₃ (Me/Ch) was added to the remaining waste from the filtrate and stored. Ethyl acetate (Ea) was added to the water portion obtained from the filtrate. The solvent of the Ea phase was completely evaporated.

The phenolic components of extracts were quantitatively determined with Agilent brand 1260 Infinity HPLC model and using Zorbax SB-C18 (4.6 x 100 mm-3.5 µm) column 6210 and Time of Flight LC/MS detector.¹⁶ The acetonitrile and ultrapure water with formic acid (1%) were used as a mobile phase mixture.

The application program was applied with per flow rate (0.6 mL per minute), total injection volume (10 µL) and column temperature (35 °C). The program was carried out so that the pure solvent mixtures were passed through the column in the range of 0-1 minute, 10% B, 1-20 min, 50% B, 20-23 min, and 23-30 min [A: Water; B: acetonitrile] according to the solvent application programs.

2.4. Antioxidant activity

The activities of extracts were performed *in vitro* by six different methods¹⁷ and compared with BHT. $A_{0.5}$ ($\mu\text{g/mL}$) values were found as an effective concentration at which the absorbance (A) was 0.5 value for total antioxidant activity and reducing power of extracts. And also IC_{50} values ($\mu\text{g/mL}$) were performed with effective concentration scavenging 50% of radicals for lipid peroxidation, metal chelating, H_2O_2 and free radical scavenging activities of extracts.

2.4.1. Total antioxidant activity by phosphomolybdate assay

The activity of extracts has performed the test described in literature¹⁸ and based on the reduction of $\text{Mo}^{+4} \rightarrow \text{Mo}^{+5}$ by the antioxidants. The formation of green $\text{PO}_4^{3-}/\text{Mo}^{+5}$ compounds monitored at acidic pH. A 0.3 mL sample was added to ammonium molybdate, sulfuric acid and sodium phosphate, respectively. Subsequently, the mixture of reaction activity was incubated at 95 °C, and read absorbance at 695 nm.

2.4.2. Assay of reducing power

The reducing power of extracts was evaluated by Oyaizu Method with slight modification.¹⁹ The extract was mixed with 0.20 M phosphate buffer (pH 6.6) and 10 g/L $\text{K}_3\text{Fe}(\text{CN})_6$, respectively. After the incubation period at 50 °C, 10% TCA (2.5 mL) was added to the reaction mixture and centrifuged at 3000 x g to obtain a clear solution. 2.5 mL of the reaction mixture was combined with 0.1% FeCl_3 and water and read at 700 nm between 3 and 5 min after initiation of the reaction. It is indicated that the increased absorbance of the reaction depending on concentration has an effective reducing in the reaction condition that the reducing capacity had increased.

2.4.3. Assay of free radical scavenging activity

The activities of the samples were performed according to the reference.²⁰ The 1 mM of DPPH· solution was combined with a sample in the test tubes and incubated at room temperature for 30 min. The absorbance of the reaction mixture was monitored at 517 nm.

2.4.4. Assay of H_2O_2 scavenging activity

The activity of the sample was evaluated according to ref.²¹ A 1 mL extract solution was added in a flask to 0.1 mM H_2O_2 in phosphate buffer (pH 7.4), ammonium molybdate, H_2SO_4 and KI. The reaction mixture was titrated with 5 mM $\text{Na}_2\text{S}_2\text{O}_3$ until the yellow color was lighter and the volume was recorded.

2.4.5. Assay of metal chelating activity

The chelating activity was performed by inhibiting the

formation of ferrozine- Fe^{2+} complex after adding of extract with Fe^{2+} .²² In the presence of sample, this complex is disrupted with sample-chelated complex. The rate of red colour reduction allows to measure level of the chelating activity. The chelating complex level of extract with Fe^{2+} was recorded at 562. Briefly, the sample was combined with 0.05 mL FeCl_2 . After adding 0.2 mL ferrozine, the reaction medium was incubated at room temperature and then the absorbance of the mixture was measured at 562 nm.

2.4.6. Inhibition assay of lipid peroxidation

The assay was carried out using TBA method based on inhibition level of linoleic acid peroxidation according to the modification literature method.²³ Briefly, the extract was combined with linoleic acid, 100 μM phosphate buffer (pH 7.4) and 20 μM ascorbic acid. The reaction of peroxidation was initiated by adding of 10 μM FeSO_4 (0.1 mL) and incubated for 60 min. The mixture was added to 10% TCA solution and kept in water bath (95 °C). After cooling at room temperature, butanol was mixed with the reaction medium and centrifuged at 4000xg. After removing the supernatant, the formation of TBA reactive substance was monitored at 532 nm.

2.5. Antimicrobial activity

The activity of extracts was performed three gram negative bacteria (*Pseudomonas aeruginosa* ATCC15442, *Escherichia coli* ATCC25922, *Klebsiella pneumoniae* ATCC 10031) and three-gram positive (*Enterococcus faecalis* ATCC29212, *Bacillus cereus* CCM99, *Staphylococcus aureus* ATCC25213) bacteria. The microorganisms were cultured in Biochemistry Research Laboratory (Ondokuz Mayıs University, Department of Chemistry, Biochemistry Laboratory).^{24,25}

The antibacterial activities of extracts were tested by disc diffusion.²⁶ The different concentrations of extracts were prepared a range of 1024-0.5 $\mu\text{g/mL}$. For disc diffusion method, amoxicillin and tetracycline were used as a positive and solvent as negative control.²⁷ 6 mm sterile discs were impregnated with 20 μL of extract materials and then incubated on MHA (Mueller Hinton Agar) medium for 16-18 hours at 37 °C on where 100 μL of suspension containing 0.5 McFarland of bacteria spread on agar. The activity was evaluated by measuring the apparent transparent inhibition zones around the discs in millimeters.

3. Statistical Analysis

The data were presented as the mean \pm standard deviation (S.D.). The results were analyzed by one-way ANOVA of variance followed by Duncan's test and considered to be significant with $p < 0.05$ confidence level, statistically.

4. RESULTS AND DISCUSSION

The amount of banana production in Turkey is increasing every year. In 2015, the banana production is 270500 tons. Bananas consumption has increased with the understanding of human health. This increase is not met by the climatic factors that limit banana breeding. Turkey has imported 235188 tonnes of bananas in 2013 to ensure that this deficiency.²⁸

Dried banana peels were extracted with boiling water prior to extraction with organic solvents, which are an important part of the characterization of the phenolic contents, due to the solvent-free residue of the banana shell for different purposes.

The use of banana peel in different areas has been investigated in Turkey.^{29,30} The water-soluble part of aqueous Turkish banana peel (Tbp) and Brazilian banana peel (Bbp) extracts can be an important source of raw materials such as phenolic and flavonoids for different applications and can be evaluated in different areas.

4.1. Chemical analysis

The analysis of the volatile compound and fatty acid components in the Tbp-Ea, Tbp-Me/Ch, Bbp-Ea and Bbp-Me/Ch extracts were made by GS-MS (Figure 1-4) and results were listed in Table 1. The 13,27-cycloursan-3-one (74.23%), 12-oleanen-3-yl acetate (16.47%) and 9,19-cyclolanost-23-ene-3,25-diol (6.29%) were found high volatile compound in Tbp-Ea extract. Cetene (3.39%), 15-heptadecenal (9.49%), 9-hexadecenol (9.74%), 1-nonadecene (6.12%) and 9,19-cyclolanost-23-ene-3,25-diol (3.66%) were the abundant volatile components in Bbp extract. Palmitic acid methyl, linoleic acid methyl and stearic acid methyl esters were the most common fatty acids in the extracts of Me/Ch and Ea in both banana samples, and their values ranged from 38.25 to 0.04%. HPLC-TOF/MS chromatograms of Tbp and Bbp extracts were obtained for quantitative and qualitative analysis as seen in Figure 5.

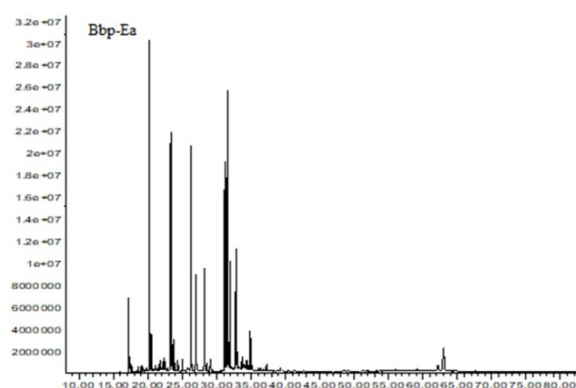


Figure 1. The GC analysis spectrum of Bbp-Ea extract

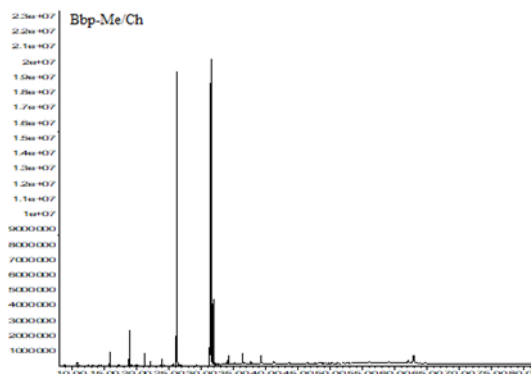


Figure 2. The GC analysis spectrum of Bbp-Me/Ch extract

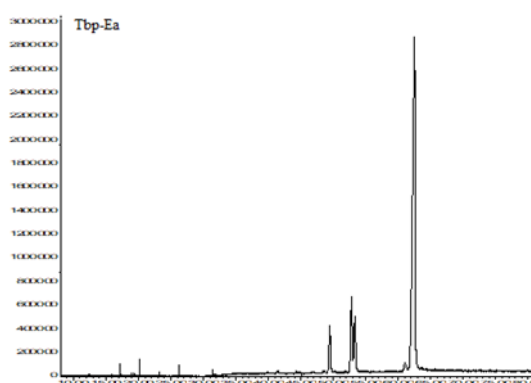


Figure 3. The GC analysis spectrum of Tbp-Ea extract

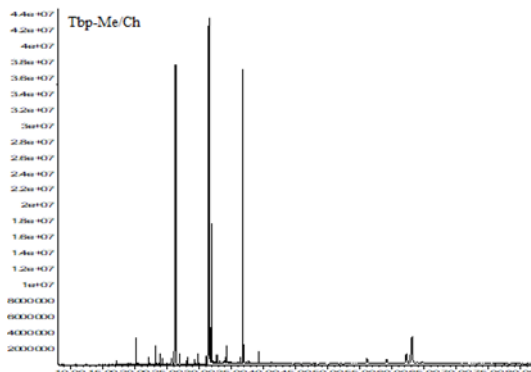


Figure 4. The GC analysis spectrum of Tbp-Me/Ch extract

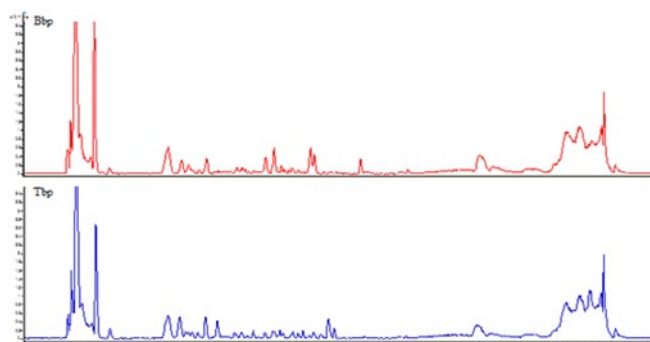


Figure 5. HPLC-TOF/MS chromatograms of extracts obtained from Bbp and Tbp

Table 1. The volatile compounds and fatty acid components (%) in the Tbp-Ea, Tbp-Me/Ch, Bbp-Ea and Bbp-Me/Ch extracts

No	Volatile Compounds, %	RT (min)	Bbp-Ea	Bbp-Me/Ch	Tbp-Ea	Tbp-Me/Ch
1	1-Tetradecene	17.180	3.33	-	0.35	-
2	3-Tetradecene	17.398	0.47	-	-	-
3	7-Tetradecene	17.591	0.42	-	-	-
4	2,6-Di-tert-butylbenzoquinone	18.598	0.22	-	-	-
5	Farnesane	18.925	0.28	-	-	-
6	2,4-di-tert-butyl-	19.185	0.24	-	-	-
7	2-Hexadecanol	19.814	0.14	-	-	-
8	Cetene	20.242	9.39	-	0.27	0.86
9	1-Decanol 2-hexyl-	20.318	0.35	-	-	-
10	7-Hexadecene	20.385	1.01	-	-	-
11	Benzophenone	21.031	0.40	-	-	-
12	Methyl tridecyl phthalate	21.492	0.14	-	-	-
13	1,3-di-iso-propylnaphthalene	21.643	0.20	-	-	-
14	1,7-di-iso-propylnaphthalene	21.727	0.36	-	-	-
15	Tetradecane	21.819	0.20	-	-	-
16	1-Hexadecanol	21.995	0.11	-	-	-
17	3-Eicosene	23.262	-	-	-	0.78
18	15-Heptadecenal	23.312	9.49	-	0.09	-
19	3-Octadecene	23.489	0.90	-	-	-
20	7-Octadecene	23.757	1.00	-	-	-
21	Hexahydrofarnesyl acetone	24.361	0.44	-	-	0.27
22	18-Norabietane	27.054	0.28	-	-	-
23	1-Nonadecene	28.228	6.12	-	-	0.59
24	2-Methyl-7-nonadecene	28.547	0.57	-	-	-
25	5-Eicosene	29.059	0.86	-	-	-
26	Methyl 2-ethylhexyl phthalate	29.839	-	-	-	0.82
27	1-Eicosanol	31.147	-	-	-	0.61
28	9-Hexadecanol	31.173	9.74	-	-	-
29	Behenic alcohol	32.775	2.93	-	-	0.39
30	Larixol	32.934	0.20	-	-	-
31	10-Heneicosene	33.060	0.36	-	-	-
32	Methyl dehydroabietate	34.587	0.16	-	-	-
33	12-Oleanen-3-yl acetate	52.798	-	-	16.47	-
34	Lupeol acetate	53.335	-	-	8.01	-
35	Stigmasterol	56.070	-	-	-	0.85
36	γ -Sitosterol	59.157	-	-	-	0.69
37	13,27-Cycloursan-3-one	62.169	0.97	0.73	74.23	1.98
38	9,19-Cyclolanost-23-ene-3,25-diol	63.007	3.66	3.18	-	6.29
No	Fatty acids					
1	Undecanoic acid 10-methylmethyl ester	19.303	0.22	-	-	-
2	Myristic acid methyl ester	22.138	0.36	0.38	-	0.32
3	Pentadecanoic acid methyl ester	23.916	0.28	0.73	-	0.50
4	Palmitoleic acid methyl ester	25.670	0.27	-	-	0.52
5	Palmitic acid methyl ester	26.282	11.77	38.25	0.36	30.63
6	Benzenepropanoic acid 3.5-bis (1.1-dimethylethyl)-4-hydroxymethyl ester	26.953	4.77	-	-	0.65
7	Margaric acid methyl ester	29.327	-	-	-	0.41
8	Linoleic acid methyl ester	31.407	6.87	18.81	0.19	23.13
9	Linolenic acid methyl ester	31.550	11.83	30.77	-	22.27
10	Stearic acid methyl ester	31.902	3.37	4.78	0.04	5.56
11	Arachidic acid methyl ester	34.209	0.16	0.51	-	0.56
12	Behenic acid methyl ester	36.424	0.12	0.87	-	0.31
13	Tricosanoic acid methyl ester	37.732	-	-	-	0.16
14	Lignoceric acid methyl ester	39.293	0.18	0.99	-	0.71
15	Pentacosanoic acid methyl ester	41.163	-	-	-	0.14

Bbp-Ea: Brazilian banana peel ethyl acetate extract**Bbp-Me/Ch:** Brazilian banana peel methanol/chloroform extract**Tbp-Ea:** Turkish banana peel aqueous extract**Tbp-Me/Ch:** Turkish banana peel methanol/chloroform extract

According to screening library and revealing retention time (RT) of calibration standards, 131 components in the Bbp (Bbp-EA, Bbp-Me/Ch) and 171 components in the Tbp (Tbp-AE, Tbp-Me/Ch) were found. As a standard, organic acids and phenolic components were used in the quantitative determination and 36 components were identified. From these components, 4-hydroxybenzoic acid (Tbp-Ea: 68.41 mg, Tbp-Me/Ch: 50.26 mg), genestistic acid (Tbp-Ea: 0.47 mg, Tbp-

Me/Ch: 0.48 mg) and syringic acid (Tbp-Ea: 1.21 mg, Tbp-Me/Ch: 1.22 mg) were the most abundant in Tbp extracts (Table 2). The unknown compounds in Tbp and Bbp extracts were determined as seen in Figure 6. Bismuth subgallate (Bbp), trimethobenzamide (Tbp), jasmonic acid (Bbp), 5 β -cholestanol (Tbp) and rhein glucuronide (Bbp) were the main unknown compound in extrats.

Table 2. Content analysis of organic acids and phenolic compounds in Tbp-Ea, Tbp-Me/Ch, Bbp-Ea and Bbp-Me/Ch extracts

No	Phenolics, (mg phenolic/kg)	Bbp- Ea	Bbp-Me/Ch	Tbp-Ea	Tbp-Me/Ch
1	Gallic acid	tr	tr	nd	nd
2	4-hydroxybenzoic acid	0.57	1.37	68.41	50.26
3	Gentisic acid	0.17	0.04	0.47	0.48
4	Protocatechuic acid	0.06	0.09	tr	nd
5	Caffeic acid	0.02	tr	nd	tr
6	Vanillic acid	0.27	0.03	0.43	nd
7	Syringic acid	0.07	0.10	1.21	1.22
8	Rutin	tr	0.01	0.50	0.38
9	4-hydroxybenzaldehyde	tr	tr	tr	tr
10	Polydatine	tr	tr	tr	nd
11	Ellagic acid	tr	nd	nd	nd
12	Scutellarin	0.04	tr	tr	nd
13	Quercetin-3- β -D-glucoside	0.01	tr	tr	tr
14	Naringin	0.01	0.04	0.02	tr
15	Diosmin	0.18	0.20	nd	2.21
16	Taxifolin	0.07	tr	tr	nd
17	Hesperidin	0.03	tr	tr	tr
18	Apigetrin	tr	tr	nd	tr
19	Neohesperidin	0.20	tr	nd	nd
20	Myricetine	tr	tr	nd	tr
21	Baicalin	tr	tr	nd	nd
22	<i>p</i> -coumaric acid	tr	tr	tr	tr
23	Fisetin	tr	tr	nd	nd
24	Protocatechuic acid	tr	tr	tr	tr
25	Morin	0.03	0.06	nd	nd
26	Salicylic acid	tr	tr	tr	tr
27	Quercetin	tr	tr	nd	nd
28	Silibinin	tr	nd	tr	nd
29	Cinnamic acid	0.02	nd	nd	nd
30	Apigenin	0.07	tr	tr	tr
31	Naringenin	0.19	tr	nd	nd
32	Kaempferol	tr	nd	nd	nd
33	Eupatorin	tr	nd	nd	nd
34	Wogonin	0.03	nd	tr	tr
35	Galangin	tr	nd	nd	nd
36	Biochanin A	tr	nd	tr	tr

tr: trace; nd: not detected

Bbp-Ea: Brazilian banana peel ethyl acetate extract

Bbp-Me/Ch: Brazilian banana peel methanol/chloroform extract

Tbp-Ea: Turkish banana peel aqueous extract

Tbp-Me/Ch: Turkish banana peel methanol/chloroform extract

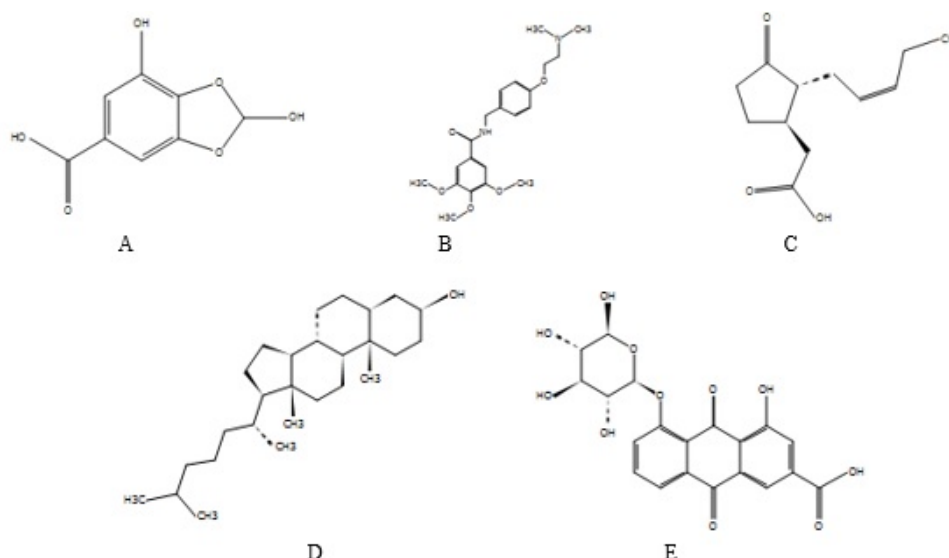


Figure 6. Unknown compounds from Bbp and Tbp extracts

4.2. Antioxidant activity

The antioxidant activities of Bbp-EA, Bbp-Me/Ch, Tbp-EA and Tbp-Me/Ch extracts were tested by total antioxidant activity, reducing power, inhibition of lipid peroxidation, metal chelating, free radical and H_2O_2 scavenging activity and compared with BHT and EDTA as positive controls (Table 3).

4.2.1. Total antioxidant activity

The activity was evaluated spectrophotometrically by

phosphomolybdenum assay. In this assay, the extract reduced Mo(VI) to Mo(V) and the green-PO4-3/Mo+5 complex was formed.¹⁶ The activities of Bbp-Ea, Bbp-Me/Ch, Tbp-EA and Tbp-Me/Ch extracts and BHA showed a significant increase depending on concentration ($p < 0.05$). (Table 3). BHT, Tbp-Ea, Bbp-Me/Ch, Bbp-Ea and Tbp-Me/Ch showed the more effective $A_{0.5}$ values, namely: 30.49, 36.84, 39.17, 49.93 and 71.45 $\mu\text{g/mL}$. Tbp-Ea and Bbp-Me/Ch were good antioxidant sources and found to have high total antioxidant activity values which were correlated with their higher concentration of phenolics.

Table 3. Total antioxidant activity, reducing power, inhibition of lipid peroxidation, free radical scavenging and H_2O_2 scavenging activities of the Tbp-Ea, Tbp-Me/Ch, Bbp-Ea and Bbp-Me/Ch extracts

Sample	Total antioxidant activity	Reducing power	DPPH [•] scavenging activity	Metal chelating activity	H_2O_2 scavenging activity	Inhibition of lipid peroxidation
	$A_{0.5}$, $\mu\text{g mL}^{-1}$		IC_{50} , $\mu\text{g mL}^{-1}$			
Bbp-Ea	49.93±3.07	9.43±0.78	10.50±2.73	17.35±1.97	0.71±0.15	3.22±0.85
Tbp-Ea	36.84±2.57	7.24±1.55	21.63±1.53	16.54±0.68	0.81±0.09	3.35±2.36
Bbp-Me/Ch	39.17±1.78	4.96±0.95	27.50±2.92	19.70±1.62	0.45±0.18	12.38±3.43
Tbp-Me/Ch	71.45±4.19	5.27±0.77	25.31±1.75	29.44±1.28	0.36±0.11	9.05±0.55
BHT	30.49±2.92	4.02±0.28	8.54±2.82	4.77±0.97	21.69±3.00	2.14±0.73

The values were represented means \pm SD ($n = 3$), $p < 0.05$

Bbp-Ea: Brazilian banana peel ethyl acetate extract

Bbp-Me/Ch: Brazilian banana peel methanol/chloroform extract

Tbp-Ea: Turkish banana peel ethyl acetate extract

Tbp-Me/Ch: Turkish banana peel methanol/chloroform extract

BHT: Butylated hydroxytoluene

4.2.2. Reducing power

This assay is used to determine the electron donating capacity of an antioxidant. In the presence of a reductive polyphenol, Fe^{3+} -ferricyanide leads to reduction of Fe^{2+} -ferricyanide. Then, the color conversion is monitored spectrophotometrically.³¹ Bbp-Ea, Bbp-Me/Ch, Tbp-EA and Tbp-Me/Ch extracts exhibited effective reducing

power at 700 nm (Table 3). It has been determined that the different concentrations of the extract are gradually increased with increasing concentration, but exhibit lower reduction power than BHA. The Tbp-Me/Ch extract showed reducing capacity higher than that of Bbp-Ea, Bbp-Me/Ch and Tbp-EA significantly. The reducing potential ($A_{0.5}$, $\mu\text{g/mL}$) of the extracts and standard increased in the following order: BHT, 4.02 >

Bbp-Me/Ch, 4.96 > Tbp-Me/Ch, 5.27 > Tbp-Ea, 7.24 > Bbp-Ea, 9.43.

4.2.3. Free radical (DPPH) scavenging

This assay was carried out with synthetic DPPH[•], which is widely used in antioxidant activity tests in evaluating the radical scavenging activity of natural and synthetic antioxidants. When an antioxidant and DPPH[•] are mixed, the antioxidant gives an hydrogen to DPPH[•] and the purple color turns into a yellow color.¹⁶ It was followed that the scavenging activities of Bbp-Ea, Bbp-Me/Ch, Tbp-EA and Tbp-Me/Ch extracts and BHT were changed as the concentrations increased. Table 3 shows the DPPH[•] scavenging capacities of the extracts. Extracts exhibited a lower free radical scavenging activity than BHT. Bbp-Ea and Tbp-Ea exhibited the effective IC₅₀ values, namely: 10.50 and 21.63 µg/mL.

4.2.4. Metal chelating activity

The O₂^{•-} and [•]OH radicals, which are the most active activators of oxidative stress, are of transition metal origin. These radicals transfer electrons, cause lipid peroxidation, damage proteins and accelerate lipid peroxidation.³² The antioxidant inhibits oxidation, reduce redox potential and stabilize the formation of metal oxide. Bbp-Ea, Bbp-Me/Ch, Tbp-EA and Tbp-Me/Ch extracts exhibited effective in stabilizing binding to the active transition metal as natural chelator products (Table 3). It was found that the extracts had lower effect on the formation of Fe²⁺-extract complex according to the formation of Fe²⁺-EDTA. The chelating activity of Tbp-

Ea (IC₅₀: 16.54 µg/mL) was found close to Bbp-Ea (IC₅₀: 17.35 µg/mL).

4.2.5. Inhibition of lipid peroxidation

Oxidation products resulting from oxidation can permanently affect or modify the defence mechanism through different chemical and physical processes. Among the target substances of oxidation are DNA, oxygen, polyunsaturated fatty acids and phospholipids cholesterol.³³ Lipid peroxidation is a radical chain process in which the primary products of lipid oxidation produced in the initial stage of the amount of peroxide and oxidation are measured.³⁴ The Bbp-Ea, Bbp-Me/Ch, Tbp-EA and Tbp-Me/Ch affected by inhibition of linoleic peroxidation, *p* < 0.05 and the results were exhibited in Table 3. The inhibition assays range from 10-100 µg mL⁻¹. The outcomes were expressed exclusively by Bbp-Ea (3.22 µg/mL) and Tbp-EA (3.35 µg/mL) exhibited a closer inhibition of linoleic peroxidation than that of BHT. Bbp-Ea and Tbp-Ea exhibited more effective inhibition of linoleic acid peroxidation (IC₅₀) than Bbp-Me/Ch and Tbp-Me/Ch.

4.3. Antimicrobial activity

The activity results were exhibited in Table 4, where it can be seen that the Turkish banana peel extracts exhibited the best antibacterial activity against the *E. coli*, *E. faecalis* and *K. pneumoniae* tested in comparison with Brazilian banana peel extracts according to inhibition zone value.

Table 4. The antimicrobial activities of the Tbp-Ea, Tbp-Me/Ch, Bbp-Ea and Bbp-Me/Ch extracts

Samples/ Antibiotics	Test	Gram-negative bacteria		
		<i>E. coli</i>	<i>P. aeruginosa</i>	<i>K. pneumoniae</i>
Tbp-Me/Ch	Inhibition zone, mm	10.8±1.13	8.75±0.49	12.15±4.03
Tbp-Ea		9.7±0.99	9.95±0.78	8.50±2.12
Bbp-Me/Ch		7.95±0.64	NA	8.85±1.06
Bbp-Ea		7.25±0.35	11.0±0.0	10.70±1.84
Tetracycline		25.25±0.35	15.65±2.05	20.30±0.28
Amoxicillin		25.35±1.91	NA	NA
Control		6.0±0.0	6.0±0.0	6.0±0.0
Samples/ Antibiotics	Test	Gram-positive bacteria		
		<i>E. faecalis</i>	<i>B. cereus</i>	<i>S. aureus</i>
Tbp-Me/Ch	Inhibition zone, mm	9.75±0.07	NA	7.0±0.00
Tbp-Ea		16.6±0.00	NA	8.20±0.85
Bbp-Me/Ch		8.70±0.42	NA	11.25±2.33
Bbp-Ea		8.00±0.57	NA	8.4±0.14
Tetracycline		17.90±0.90	47.00±4.24	20.40±0.57
Amoxicillin		25.7±0.99	34.75±3.89	26.95±0.78
Control		6.0±0.0	6.0±0.0	6.0±0.0

NA: no activity. The values were represented means ± SD (*n* = 3), *p* < 0.05

Bbp-Ea: Brazilian banana peel ethyl acetate extract

Bbp-Me/Ch: Brazilian banana peel methanol/chloroform extract

Tbp-Ea: Turkish banana peel ethyl acetate extract

Tbp-Me/Ch: Turkish banana peel methanol/chloroform extract

The Tbp-Ea was most active against *E. faecalis* in comparison to all the microorganisms tested and exhibited a broad spectrum of antibacterial activity. Specifically, the ethyl acetate and methanol/chloroform extracts showed different levels of antibacterial activity against gram positive and negative bacteria. This is supported by a previous study on water³⁵, isopropyl alcohol³⁶ and ethyl acetate³⁷ extracts that exhibit close or greater activity against ethyl acetate and methanol/chloroform extracts against bacteria without cellular toxicity.

5. CONCLUSIONS

The agro-residues can be considered a valuable resource after recycling and reprocessing. The banana peel has a lot of antioxidant activity and can be a very cheap source of extracts rich in bioactive compounds. This study showed that it had important effects on the phenolic contents extracted by extraction with Ea and Me/Ch. Total antioxidant activities of Tbp-Ea and Bbp-Me/Ch were found to be close to BHT. Tbp-Ea, Bbp-Ea, Bbp-Me/Ch and Tbp-Me/Ch are promising natural additives that exhibit antibacterial, H₂O₂ scavenging activity and the capacity to inhibit lipid peroxidation. However, the metal chelate capacity of the extracts was low. This research has compared the phytochemical and bioactivity potentials of Brazilian banana peel extract and Turkish banana peel extracts by chromatographic and spectroscopic analysis, and also revealed promising results.

ACKNOWLEDGEMENTS

This work was supported by Project Management Office (BAP), Ondokuz Mayıs University, Samsun for supporting this research with PYO.FEN.1904.19.006 and PYO.FEN.1904.20.002 project numbers. We are also thankful to Sarmed Marah for helping in the antibacterial activity, and also Fatih Gül for the HPLC-TOF/MS and GC-MS analyzes of the extracts

Conflict of interests

The authors declare that there is no a conflict of interest with any person, institute, company, etc.

REFERENCES

- Pandey, K. B.; Rizvi, S. I. *Oxid. Med. Cell. Longev.* **2009** 2: 270-278.
- Ravindran, R.; Jaiswal, A. K. *Trends Biotechnol.* **2016** 34: 58-69.
- Mohapatra, D.; Mishra, S.; Sutar N. *Indian J. Biochem. Bio.* **2010**, 69, 323-329.
- Aurore, G.; Parfait, B.; Fährasmane, L. *Trends Food Sci. Tech.* **2009**, 20: 78-91.
- González-Montelongo, R.; Lobo, M.G.; González, M. *Food Chem.* **2010** 119: 1030-1039.
- Pereira, A.; Maraschin, M. *J. Ethnopharmacol.* **2015**, 160: 149-163.
- Darsini, D.; Maheshu, V.; Vishnupriya, M.; Sasikumar, J. *Indian J. Biochem. Bio.* **2012**, 49, 124-129.
- Can-Cauch, C. A.; Sauri-Duch, E.; Betancur-Ancona, D.; Chel-Guerrero, L.; González-Aguilar, G. A.; Cuevas-Glory L.F.; Pérez-Pacheco E.; Moo-Huchin V.M. *J. Funct. Food* **2017**, 37: 501-506.
- Singh, R.; Singh, G.; Chauhan G. *Trends Food Sci. Tech.* 1996, 33: 355-357.
- Elleuch, M.; Bedigian, D.; Roiseux, O.; Besbes, S.; Blecker, C.; Attia H., *Food Chem.* **2011**, 124: 411-421.
- Agama-Acevedo, E.; Sañudo-Barajas, J.; Vélez De La Rocha, R.; González-Aguilar, G.; Bello-Perez, L.A. *Cyta-J. Food*, **2016**, 14: 117-123.
- Pathak, P. D.; Mandavgane, S. A.; Kulkarni, B. D. *Rev. Chem. Eng.* **2016**, 32: 651-666.
- Yusuf, M. *Journal of Tropical Soils* **2016**, 20: 59-65.
- Memon, J.R.; Memon, S.Q.; Bhangar, M.I.; El-Turki, A.; Hallam, K.R.; Allen, G.C. *Colloid Surface B.* **2009**, 70: 232-237.
- Koldaş, S.; Demirtas, I.; Ozen, T.; Demirci, M. A.; Behçet, L. *J. Sci. Food Agr.* **2015**, 95: 786-798.
- Ozen, T.; Yenigun, S.; Altun, M.; Demirtas, I., *Comb. Chem. High T. Scr.* **2017**, 20: 559-578.
- Gulcin, İ. *Arch. Toxicol.* **2020**, 94: 651-715.
- Prieto, P.; Pineda, M.; Aguilar, M. *Anal. Biochem.* **1999**, 269: 337-341.
- Oyaizu, M. *Japanese Journal of Nutrition* **1986**, 44: 307-315.
- Blois, M. S., *Nature* **1958**, 181, 1199-1200.
- Zhao, G. R.; Xiang, Z. J.; Ye, T. X.; Yuan, Y. J.; Guo, Z.X. *Food Chem.* **2006**, 99: 767-774.
- Dinis, T. C.; Madeira, V. M.; Almeida, L.M. *Arch. Biochem. Biophys.* **1994**, 315: 161-169.

23. Choi C. W.; Kim S. C.; *Plant Sci.* **2002**, 163: 1161-1168.
24. Hudzcki, J. *Kirby-Bauer Disk Diffusion Susceptibility Test Protocol.* **2009**, 1-23.
25. Ozen, T.; Kizil, D.; Yenigun, S.; Cesur, H.; Turkekul, I. *Int. J. Med. Mushrooms* **2019**, 21.
26. Reller, L. B.; Weinstein M.; Jorgensen J. H.; Ferraro M. J., *Clin. Infect. Dis.* **2009**, 49: 1749-1755.
27. Ozen, T.; Bora, N.; Yenigun, S.; Korkmaz, H. *Flavour. Frag. J.* **2020**, 35: 270-283.
28. Sarıdaş, M. A.; Kargi, S. P.; Bayirođlu B. M.; Şeyma, Y. *Yüzüncü Yıl Üniversitesi Tarım Bilimleri Dergisi.* **2017**, 27: 370-377.
29. Topbaşı, B.; Sevinçli, Y. *Electronic Journal of Vocational Colleges* **2017**, 7(1), 47-53.
30. Ince, M.; Ince, O.; Asam, E.; Önal, A. *Atom Spectrosc.* **2017**, 38: 142-148.
31. Bursal, E.; Köksal, E. *Food Res. Int.* **2011**, 44: 2217-2221.
32. Haber F.; Weiss, J. *Naturwissenschaften*, **1932**, 20: 948-950.
33. Antoovich, M.; Prenzler, P.D.; Patsalides, .E; Mcdonal, S.; Robards, K., *Analyst*, **2002**, 127: 183-198
34. Frankl, E. N, *Lipid Oxidation.* Elsevier, **2014**, 391.
35. Chabuk, Z; Al-Charrakh, A.H.; Hindi, N.K.K.; Hindi, S.K.K., *Res. Gate. Pharm. Sci.* **2013**, 1: 73-75.
36. Kapadia, S. P.; Pudakalkatti P.S.; Shivanaikar S. *Contemp.Clin. Dent.* **2015**, 6: 496-499.
37. Mokbl, M. S.; Hashinaga, F. *Am. J. Biochem. Biotechn.* **2005**, 1: 125-131.



Inhibition profiles and molecular docking studies of antiproliferative agents against aldose reductase enzyme

 Namık KILINÇ^{1,*}

¹Department of Medical Services and Techniques, Vocational School of Health Service, Iğdir University, 76000 Iğdir, Turkey

Received: 28 May 2021; Revised: 7 June 2021; Accepted: 7 June 2021

*Corresponding author e-mail: namik.kilinc@igdir.edu.tr

Citation: Kılınç, N. *Int. J. Chem. Technol.* 2021, 5 (1), 77-82.

ABSTRACT

Inhibition of Aldose Reductase (AR) is very important in terms of preventing many diabetic complications such as retinopathy, neuropathy, and cataract. In this study, inhibition effects of some antiproliferative agents, which have been shown to have many biological activities besides their anticancer properties, on the AR enzyme, which is a diabetes-related enzyme, were investigated. Biochanin A compound with an IC₅₀ value of 4.44 μM showed the best inhibition effect. IC₅₀ values of Rhein, Betulinic acid, Sanguinarine chloride, Budesonide, Plumbagin and 2-Methoxyestradiol compounds were calculated as 7.87 μM, 7.45 μM, 19.25 μM, 21.00 μM, 28.87 μM and 38.5 μM, respectively. Molecular docking studies have also been conducted to elucidate the inhibition mechanisms of the compounds whose *in vitro* inhibition effects have been investigated, and the free binding energies of enzyme-inhibitor complexes have been calculated with the Molecular Mechanics Generalized Born Surface Area (MM-GBSA). Both experimental data and computer-aided calculations have revealed that the compounds studied are very important drug candidates aimed at preventing diabetic complications.

Keywords: Aldose reductase, antiproliferative, molecular docking, inhibition.

Antiproliferatif ajanların aldoz redüktaz enzimine karşı inhibisyon profilleri ve moleküler docking çalışmaları

ÖZ

Aldoz Redüktaz (AR)'ın inhibisyonu, retinopati, nöropati, katarakt gibi birçok diyabetik komplikasyonun önlenmesi açısından oldukça önemlidir. Bu çalışmada, antikanser özelliklerinin yanı sıra birçok biyolojik aktiviteye sahip oldukları gösterilen bazı antiproliferatif ajanların diyabet ilişkili bir enzim olan AR enzimi üzerine inhibisyon etkileri araştırılmıştır. En iyi inhibisyon etkisini IC₅₀ değeri 4.44 μM olarak bulunan Biochanin A bileşiği göstermiştir. Rhein, Betulinic acid, Sanguinarine chloride, Budesonide, Plumbagin ve 2-Methoxyestradiol bileşiklerinin IC₅₀ değerleri, sırasıyla, 7.87 μM, 7.45 μM, 19.25 μM, 21.00 μM, 28.87 μM ve 38.5 μM olarak hesaplanmıştır. *In vitro* inhibisyon etkileri incelenen bileşiklerin inhibisyon mekanizmalarını aydınlatmak amacıyla moleküler docking çalışmaları da yapılmış ve enzim-inhibitör komplekslerinin, Molecular Mechanics Generalized Born Surface Area (MM-GBSA) ile serbest bağlanma enerjileri hesaplanmıştır. Hem deneysel veriler hem de yapılan bilgisayar destekli hesaplamalar çalışılan bileşiklerin diyabetik komplikasyonların önlenmesini hedefleyen çok önemli birer ilaç adayı olduklarını ortaya koymuştur.

Anahtar Kelimeler: Aldoz redüktaz, antiproliferatif, moleküler docking, inhibisyon.

1. INTRODUCTION

Long-term hyperglycemia in diabetes mellitus is regarded to be the primary cause of long-term diabetic disorders such as nephropathy, retinopathy, cataractogenesis, and neuropathy. Excessive oxidative stress, increased advanced glycation endproduct (AGE) synthesis, and an augmented aldose reductase-related polyol pathway have all been identified as possible paths

to explain the pathophysiology of diabetic problems.¹ Aldose Reductase (AR) is a monomeric reduced nicotinamide adenine dinucleotide phosphate (NADPH)-dependent enzyme that belongs to the aldo-keto reductase superfamily. Aldose reductase's primary function is to convert toxic aldehydes in the cell to inert alcohols, but when glucose levels in the cell become too high, it also transforms glucose to sorbitol, which is subsequently oxidized to fructose.²

AR is found in nearly all mammalian cells, as well as in elevated amounts in certain tissues including the retina, lens, and sciatic nerves, which are quickly compromised by diabetic complications linked to increased polyol pathway flux which can lead to cataract.³ Furthermore, because of their low penetration through membranes and inadequate metabolism, sorbitol and its metabolites concentrate in the eye, nerves, and kidneys, leading to the generation of diabetic complications such as nephropathy, retinopathy, and neuropathy.⁴ The AR enzyme has also been reported to be associated with many other diseases, including inflammation,⁵ cardiovascular diseases,^{6,7} ovarian abnormalities,^{8,9} depression,^{10,11} and cancer.¹² In addition, numerous studies have demonstrated that inhibition of AR prevents restenosis, endothelial cell apoptosis, and vascular smooth muscle growth.^{13,14}

As a result, AR inhibitors (ARIs) could be a possible therapeutic option for treating and preventing diabetic complications through suppressing the hyperglycemia-induced polyol pathway flux. So, in our presented study, we investigated inhibition effects of some anti-proliferative agents on diabetes mellitus-related aldose reductase enzyme. Molecular docking studies have also been conducted to elucidate the inhibition mechanisms, and Molecular Mechanics Generalized Born Surface Area (MM-GBSA) free binding energies of anti-proliferative agents-AR complexes have been calculated.

2. MATERIALS AND METHODS

2.1. Chemicals

β -nicotinamide adenin dinucleotide phosphate (β -NADPH), DL-glyceraldehyde, Na-phosphate, recombinant human aldose reductase enzyme, and antiproliferative agents were obtained from Sigma-Aldrich Co. (Taufkirchen, Germany).

2.2. The AR activity assay

The AR enzyme activity was measured using a modified version of Cerelli et al (1986)'s protocol.¹⁵ To begin the reaction, a 1 mL reaction medium was made by combining 0.45 mL deionized water, 0.1 mL NADPH, 0.25 mL Na-phosphate buffer, 0.1 mL enzyme solution, and 0.1 mL DL-glyceraldehyde. Spectrophotometric monitoring of the decline in NADPH concentration at 340 nm was used to assess enzyme activity.

2.3. In Vitro inhibition studies

The anti-proliferative agents Biochanin A, Rhein, Sanguinarine chloride, 2-Methoxyestradiol, Budesonide, Plumbagin, and Betulinic acid were tested for their ability to inhibit the AR enzyme. Each antiproliferative agent was prepared in five separate concentration, and

the inhibitory actions of these compounds on the AR enzyme were investigated. The enzyme activity in the inhibitor-free control cuvette was assumed to be 100%, and inhibitor concentrations that halved the enzyme activity were calculated (IC₅₀ values).

2.4. Molecular docking studies

To assess the potential interactions of the studied anti-proliferative agents with the target enzyme, AR, molecular docking simulations were run. To conduct molecular docking simulations, the Maestro 12.5 program, which is part of the Schrödinger Molecular Modeling Suite program, was used.¹⁶ To begin, the RCSB Protein Data Bank (PDB) was used to obtain the X-ray crystal structure of the AR enzyme (PDB ID: 2FZD). The Protein Preparation Wizard was used to preprocess and prepare the enzyme crystal structure under physiological conditions. The binding order and charges were allocated using the protein preparation wizard,¹⁷ all missing hydrogen atoms were inserted, and missing side chains of the protein were filled using the Prime module of the Maestro 12.5. With the assistance of Maestro's Ligprep software, 2D structure sketches of all ligands to be docked, their transformation into 3D structures, their protonation states at pH 7.4, and their optimizations were carried out. After preparing the protein structure and ligands to be docked, anti-proliferative agents were docked against the AR enzyme using Glide/XP (extra precision).¹⁸ The Glide software¹⁹ was used to measure the anti-proliferative agents' binding energies and docking scores to the AR target.

2.5. Calculations of binding free energy via molecular mechanics/generalized born surface area (MM/GBSA)

The Molecular Mechanics/Generalized Born Surface Area (MM/GBSA) approach combines molecular mechanics equations with continuum solvation models to measure binding free energies (ΔG_{bind}) for macromolecules.²⁰ Prime/MM-GBSA, which uses the OPLS3e force field and the VSGB dissolvable model, is used to calculate the binding free energies of AR-anti-proliferative agent complexes.²¹

3. RESULTS AND DISCUSSION

The polyol pathway, which becomes active when blood sugar levels rise, is regarded to be the leading cause of diabetic disorders. Aldose reductase, the initial stage of the polyol pathway, is related in particular to diabetes sequelae such as retinopathy, neuropathy, cataractogenesis, and nephropathy.²² Therefore, inhibitors of aldose reductase can be helpful therapeutic drugs for diabetic complication treatment and prevention.²³ New and efficient aldose reductase inhibitors need to be identified in order to better the

quality of life of diabetes patients by preventing diabetes complications. In this connection, our current work looked at the *in vitro* inhibition impact of certain antiproliferative agents on the activity of the human

recombinant aldose reductase enzyme. *In vitro* inhibition results of antiproliferative agents on aldose reductase enzyme are collectively given in Table 1.

Table 1. *In vitro* inhibition results of antiproliferative agents against aldose reductase enzyme

Compound	IC ₅₀ (μM)	R ²
Biochanin A	4.440	0.926
Rhein	7.870	0.947
Betulinic acid	7.450	0.980
Sanguinarine chloride	19.25	0.957
Budesonide	21.00	0.930
Plumbagin	28.87	0.978
2-Methoxyestradiol	38.50	0.930

In addition, binding modes and binding energies were also calculated by molecular docking simulations to evaluate the inhibition mechanism of antiproliferative agents whose inhibition effects on the recombinant human enzyme were investigated. However, molecular mechanical Generalized Born Surface Area (MM /

GBSA) method was used to calculate the free binding energies of AR-antiproliferative agent complexes. The results of molecular docking simulations and MM-GBSA free binding energies are given in Table 2. Sorbinil, which is a standard inhibitor for AR enzyme, was used as a positive control compound.

Table 2. Docking scores, binding energies and Prime MM-GBSA free binding energies (ΔG) of antiproliferative agents for AR enzyme

Name	Docking Score	XP GScore	Glide evdw	Glide emodel	MM-GBSA (ΔG _{bind})
Biochanin A	-10.04	-10.35	-32.73	-57.28	-62.17
Rhein	-9.72	-9.72	-28.44	-53.08	-42.67
Sanguinarine chloride	-9.09	-9.10	-30.43	-51.74	-56.96
2-Methoxyestradiol	-8.82	-8.82	-23.30	-33.57	-49.82
Budesonide	-8.29	-8.29	-24.24	-48.17	-50.92
Plumbagin	-7.35	-7.63	-20.17	-30.91	-38.29
Betulinic acid	-5.83	-5.84	-21.27	-34.80	-26.70
Sorbinil	-7.81	-7.86	-28.89	-43.59	-42.61

Biochanin A compound, which was previously determined to have antioxidant, anti-inflammatory, anticancer, anti-microbial, neuroprotective and hepatoprotective properties,²⁴ has a very strong inhibition effect (IC₅₀=4.44 μM) against the AR enzyme. Molecular docking studies of the Biochanin A compound against the AR enzyme revealed that the compound constructed hydrogen bonding with the amino acid residues TYR48 and HIS110 and a π-π interaction with TRP111 at the active site of the enzyme (Figure 1). The compound was determined to have better docking score and lower free binding energy (ΔG) than the positive control compound, sorbinil (Table 2).

It has been shown in the literature that Betulinic acid and Rhein compounds, which we found to have close and strong inhibitory effects as a result of our *in vitro* inhibition studies (IC₅₀=7.45 μM and 7.87 μM, respectively), have nephroprotective, hepatoprotective,

anti-inflammatory, anticancer, anti – HIV, antioxidant, antimalarial and antimicrobial activities.^{25,26} Molecular docking studies for Rhein and Betulinic acid compounds, which show strong experimental AR inhibitory effects, confirmed the inhibition effects of the compounds (docking scores, 9.72 and 5.83, respectively). Rhein compound established three hydrogen bonding with the residues TYR48, HIS110 and TRP111 and dual π-π stackings with the amino acid residue TRP20 in the active site of the AR enzyme (Figure 2). Similar to the Rhein compound, Betulinic acid hydrogen bonded to the Trp20 amino acid residue in the AR active center and also interacted hydrophobically with amino acids such as TYR48 and TRP111 (Figure 3).

IC₅₀ values of other antiproliferative agents, Sanguinarine chloride, Budesonide, Plumbagin and 2-Methoxyestradiol compounds, whose inhibition effects against AR enzyme were investigated, were found in the

range of 19.2-38.5 μ M. It can be said that these compounds (Sanguinarine chloride, Budesonide, Plumbagin and 2-Methoxyestradiol), which have a wide range of biological activities, have antidiabetic effects, considering their inhibition effects for the determined AR enzyme. Molecular docking studies for these compounds

reveal that all of the compounds scored much better than the positive control compound, sorbinil (Table 2). In addition, in the MM-GBSA study, the compounds (except Plumbagin) were also found to have better free binding energies than sorbinil.

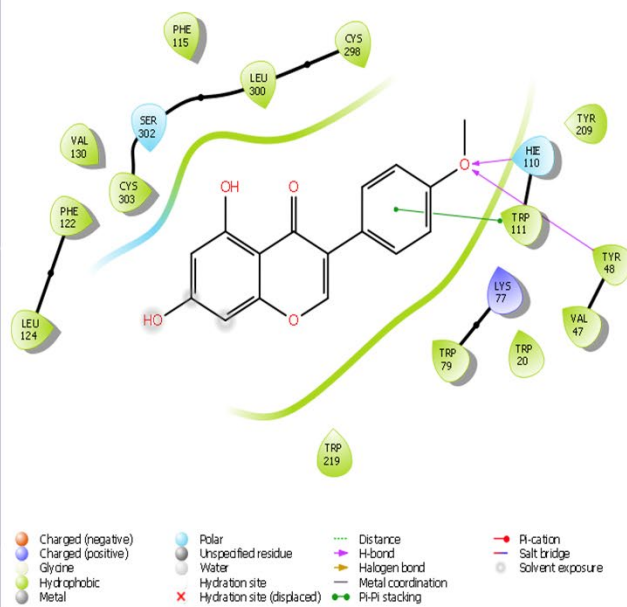
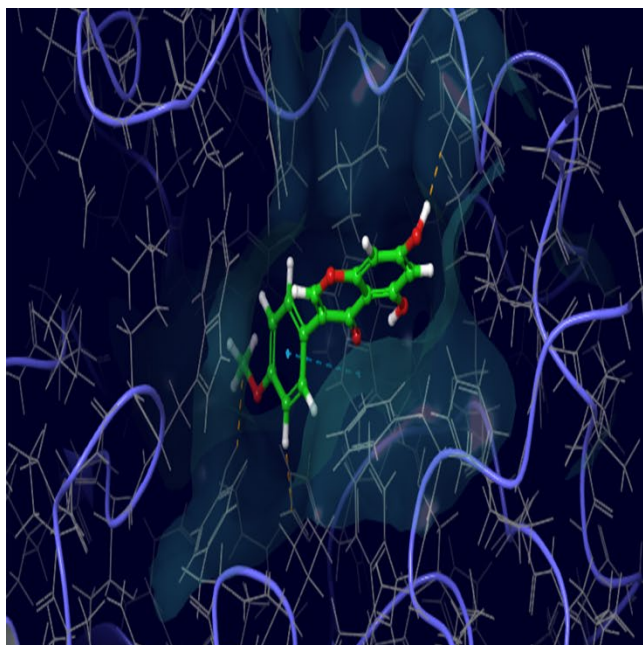


Figure 1. 3D binding mode (left) and 2D ligand interactions (right) of Biochanin A compound with AR enzyme. Ligand binding site represented as a solid surface.

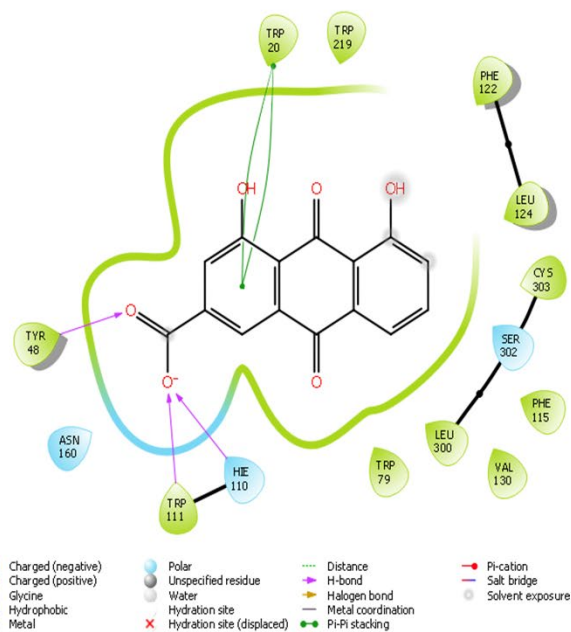
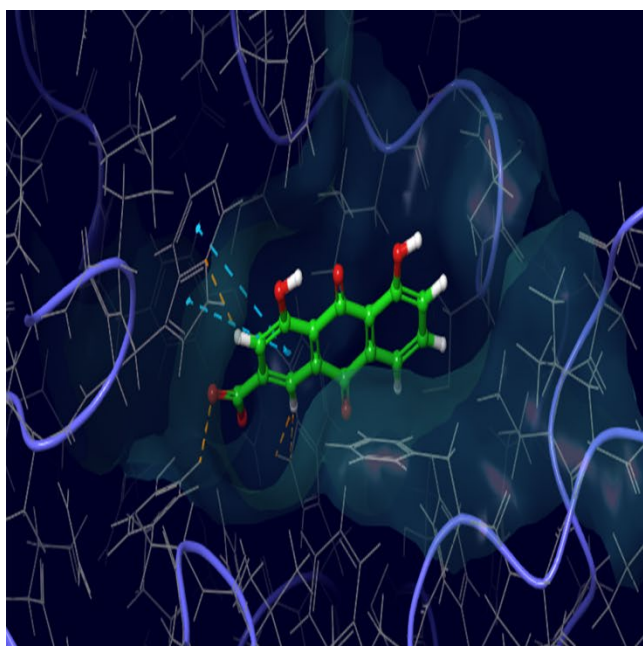


Figure 2. 3D binding mode (left) and 2D ligand interactions (right) of Rhein compound with AR enzyme. Ligand binding site represented as a solid surface.

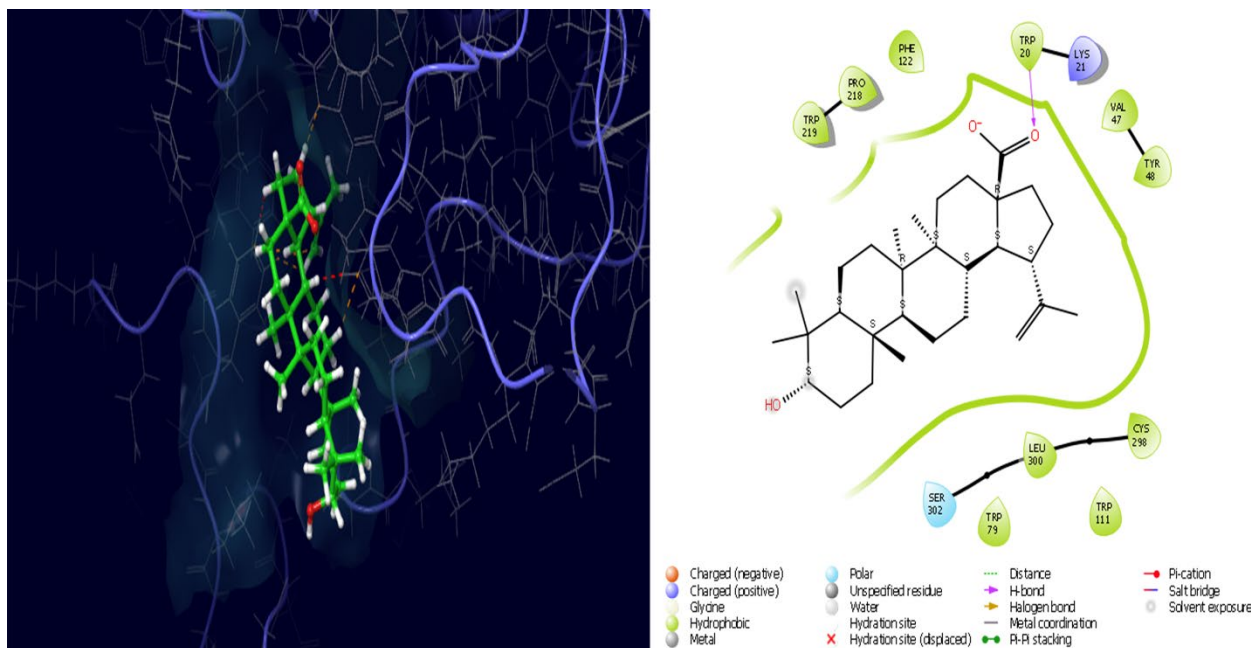


Figure 3. 3D binding mode (left) and 2D ligand interactions (right) of Betulinic acid compound with AR enzyme. Ligand binding site represented as a solid surface.

CONCLUSIONS

Inhibition of the AR enzyme, an enzyme of the polyol pathway that is activated in the case of high blood glucose levels, is vital in terms of preventing and delaying diabetic complications. Thus, the discovery of effective AR enzyme inhibitors is a hope for the treatment of diabetes mellitus-related diseases. Therefore, the *in vitro* inhibition effects of natural antiproliferative agents with known biological activities on the AR enzyme were examined and molecular docking studies were carried out to confirm the experimental inhibition results. Both the obtained experimental data and computer-aided modeling studies showed that all antiproliferative agents whose inhibition effects were examined are good drug candidates for the prevention of diabetic complications.

ACKNOWLEDGEMENTS

The author is thankful for its help in this research to Iğdir University Research Fund Accounting. (Project number: 2020-SBE-A03).

Conflict of interests

The author declares that there is no a conflict of interest with any person, institute, company, etc.

REFERENCES

1. El-Kabbani, O.; Ruiz, F.; Darmanin, C.; Chung, R. T. *Cell Mol Life Sci.* **2004**, 61(7), 750-762.
2. Brownlee, M. *Nature.* **2001**, 414(6865), 813-820.
3. Nishimura, C.; Yamaoka, T.; Mizutani, M.; Yamashita, K.; Akera, T.; Tanimoto, T. *Biochim. Biophys. Acta.* **1991**, 1078(2), 171-178.
4. Hotta, N.; Kawamori, R.; Fukuda, M.; Shigeta, Y. *Diabet. Med.* **2012**, 29(12), 1529-1533.
5. Ramana, K.V.; Srivastava, S.K. *Cytokine.* **2006**, 36, 115-122.
6. Ramasamy, R.; Liu, H.; Oates, P.J.; Schaefer, S. *Cardiovasc. Res.* **1999**, 42, 130-139.
7. Hwang, Y.C.; Sato, S.; Tsai, J.Y.; Yan, S.; Bakr, S.; Zhang, H.; Ramasamy, R. *FASEB J.* **2002**, 16, 243-245.
8. Berry, G.T. *Eur. J. Pediatr.* **1995**, 154, 53-64.
9. Lee, K.W.; Ko, B.C.; Jiang, Z.; Cao, D.; Chung, S.S. *Anti-cancer drugs.* **2001**, 12, 129-132.
10. Regenold, W.T.; Kling, M.A.; Hauser, P. *Psychoneuroendocrinology.* **2000**, 25, 593-606.
11. Regenold, W.T.; Phatak, P.; Kling, M.A.; Hauser, P. *Mol. Psychiatry.* **2004**, 9, 731.
12. Saraswat, M.; Mrudula, T.; Kumar, P.U.; Suneetha, A.; Rao, T.S.; Srinivasulu, M.; Reddy, G.B. *Med. Sci. Monit.* **2006**, 12, 525-529.
13. Ramana, K.V.; Bhatnagar, A.; Srivastava, S.K. *FASEB J* **2004**, 18, 1209-1218

14. Chandra, D.; Ramana, K.V.; Friedrich, B.; Srivastava, S.; Bhatnagar, A.; Srivastava, S.K. *Chem. Biol. Interact.* **2003**, 143–144, 605–612
15. Cerelli, K.J.; Curtis, D.L.; Dunn, J.P.; Nelson, P.H.; Peak, T.M.; Waterbury, L.D. *J. Med. Chem.* **1986**, 29, 2347-2351.
16. Schrödinger Release 2020-3: Schrödinger, **2020**, LLC, New York, NY.
17. Sastry, G.M.; Adzhigirey, M.; Day, T.; Annabhimoju, R.; Sherman, W. *J. Comput. Aided Mol. Des.* **2013**, 27, 221-234.
18. Friesner, R.A.; Banks, J.L.; Murphy, R.B.; Halgren, T.A.; Klicic, J.J.; Mainz, D.T.; Shenkin, P.S. *J. Med. Chem.* **2004**, 47, 1739-1749.
19. Halgren, T.A.; Murphy, R.B.; Friesner, R.A.; Beard, H.S.; Frye, L.L.; Pollard, W.T.; Banks, J.L. *J. Med. Chem.* **2004**, 47, 1750-1759.
20. Genheden, S.; Ryde, U. *Expert. Opin. Drug. Discov.* **2015**, 10(5), 449-461.
21. Prime, Schrödinger, **2020**, LLC, New York, NY.
22. Kato, A.; Yasuko, H.; Goto, H.; Hollinshead, J.; Nash, R. J.; Adachi, I. *Phytomedicine.* **2009**, 16(2-3), 258-261.
23. Ziegler, D. *Nephrol. Dial. Transplant.* **2004**, 19(9), 2170-2175.
24. Sarfraz, A.; Javeed, M.; Shah, M. A.; Hussain, G.; Shafiq, N.; Sarfraz, I.; Riaz, A.; Sadiqa, A.; Zara, R.; Zafar, S.; Kanwal, L.; Sarker, S.D.; Rasul, A. *Sci. Total Environ.* **2020**, 722, 137907.
25. Alakurtti, S.; Mäkelä, T.; Koskimies, S.; Yli-Kauhaluoma, J. *Eur. J. Pharm. Sci.* **2006**, 29(1), 1-13.
26. Zhou, Y. X.; Xia, W.; Yue, W.; Peng, C.; Rahman, K.; Zhang, H. *Evid. Based Complement. Alternat. Med.* **2015**, 2015, 1-10.0